# Impact of solar eclipses on $NO_2$ in the Earth's atmosphere as measured from space by TROPOMI

## Understanding the sensitivity of the Earth's atmospheric composition to short-term variations in sunlight

MSc Thesis, Geoscience & Remote Sensing

Jelle Schrijver

Delft University of Technology

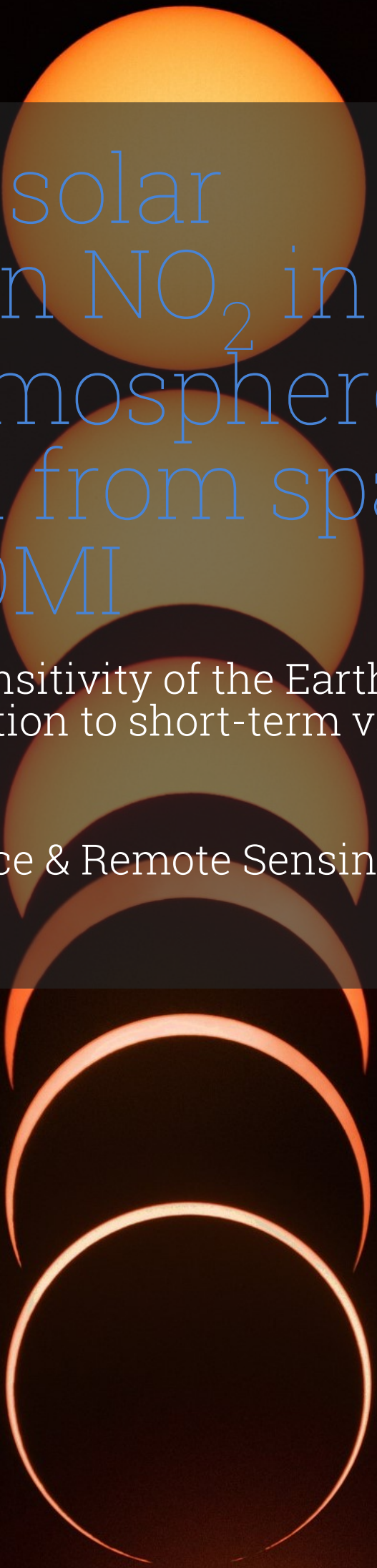

TU Delft

# Impact of solar eclipses on $NO_2$ in the Earth's atmosphere as measured from space by TROPOMI

## Understanding the sensitivity of the Earth's atmospheric composition to short-term variations in sunlight

by

Jelle Schrijver
Student number: 4581687

to obtain the degree of Master of Science
at the Delft University of Technology,
to be defended on Wednesday, February 14, 2024 at 14:00

| | |
|---|---|
| Graduation Supervisor: | Dr. J.P. Veefkind, TU Delft & KNMI |
| Daily Supervisor: | Ir. V. J. H. Trees, TU Delft & KNMI |
| Additional Supervisor: | Dr. S.R. de Roode, TU Delft |
| Additional Supervisor: | Ir. C.M.H. Unal, TU Delft |
| Additional Supervisor: | Dr. D.M. Stam |
| Institution: | Royal Netherlands Meteorological Institute |
| University: | University of Technology Delft |
| Faculty: | Faculty of Geosciences and Civil Engineering, Delft |
| Master Track: | Geosciences and Remote Sensing |
| Project Duration: | March 2023 - January 2024 |

An electronic version of this thesis is available at http://repository.tudelft.nl/

Cover: The annular solar eclipse of 2019 from the beginning to the ring of fire (Credit: Goh Keng Cheong / Getty Images)

TU Delft

Royal Netherlands Meteorological Institute
*Ministry of Infrastructure and the Environment*

# Preface

In front of you lies the MSc thesis titled ‘’Impact of solar eclipses on $NO_2$ in the Earth’s atmosphere as measured from the space by TROPOMI’’ which marks the end of my study time in Delft. As a first-year student, I started to explore and expand my interest in the Earth as a planet by starting the Applied Earth Sciences bachelor. This lay closest to my enthusiasm for the world outside of the big cities but was also in range of my desire to become an engineer. The bachelor led me to end up at the Geoscience & Remote Sensing master as my desire to ‘see’ more of the world grew. The master handed me the opportunities to explore and analyse large-scale global geoscientific problems, all being done from behind a desk in Delft. Consequently, this resulted in a great opportunity to conduct my final thesis research at the Royal Dutch Meteorological Institute, widely known as the KNMI.

The research on the response of atmospheric $NO_2$ to the influence of solar eclipses has enabled me to apply my knowledge gained over several years of studying in Delft. Simultaneously, the experience at KNMI has provided me with an excellent look into the scientific world. The interesting aspects and appliances of this research have pushed me to dive deep into the subject and motivated me significantly to figure out the origin of the problem. The motivation and drive for this research have not been possible without the outstanding guidance of Victor. The extensive discussions and countless new ideas to explore helped me achieve a high quality of work. You also always saw something to improve in graphs for which I thought they had reached their final state. Thank you for your input, Victor. Pepijn, thank you for your expert view on all aspects related to TROPOMI and the $NO_2$ retrieval. Your overall view on the problem at hand helped me guide my thesis in the right direction. Benjamin, I want to thank you specifically for all the coding questions I’ve had that you were willing and able to help me with. It certainly saved me quite some hours of headache. Stephan, Daphne and Christine thank you for your valuable feedback during the meetings we had throughout my thesis.

During my time in Delft, I’ve had the opportunity to meet some amazing people at Yeti and do some amazing climbs with them. Thank you for clearing my mind during the several climbing trips we have made during the thesis. To my roommates, thank you for keeping the spirit high and making me feel at home. Thank you to all the hardworking fellow thesis students in our room the ’afstudeerhok’. The many coffees and intermezzos we’ve shared made the time at the faculty enjoyable. To Femke, thank you for your endless support and encouragement. Your belief in me made me persevere until the very end. Thank you to my father, mother, sister and brother, who have been welcoming me whenever I felt the need to escape from Delft. Last but not least, thank you to you, my reader, for reading my thesis. Enjoy it!

*Jelle Schrijver*
*Delft, February 2024*

# Abstract

During a solar eclipse, sunlight incident on the Earth is reduced due to the (partial) shadow of the Moon. Atmospheric trace gas concentrations which are influenced by the amount of available sunlight, such as nitrogen dioxide ($NO_2$), may be affected due to the disrupted photolysis processes. Large-scale observations of the increased $NO_2$ concentrations caused by the solar eclipse would improve our understanding of the sensitivity of $NO_2$ in the atmosphere to short-term variations in sunlight. Spaceborne measurements can provide valuable information about the large-scale spatial distribution of $NO_2$, which is provided daily by the TROPOMI instrument aboard the Sentinel-5 Precursor satellite by measuring and retrieving locally reflected sunlight. However, the TROPOMI $NO_2$ retrieval is unable to derive reliable concentrations during a solar eclipse, as solar eclipses are not taken into account in its retrieval algorithm. In this research, we have adjusted the $NO_2$ retrieval of TROPOMI such that it can handle solar eclipses and study the large-scale response of $NO_2$ during two solar eclipses over Europe in 2021 and 2022. We found a large-scale increase of $NO_2$ in the adjusted measurements, which linearly correlated with the degree of obscuration. We compared the measured $NO_2$ increase with the values from the atmospheric chemistry model TM5 including an applied eclipse implementation and we found a close agreement in most areas that are not highly polluted. Our measurements and model predict a $NO_2$ increase of 60%$\pm$12% and 70%$\pm$7% for an obscuration fraction of 1, respectively. More advanced chemistry modelling work is needed to explain the measurements in highly populated areas. We conclude that our results demonstrate that the TROPOMI algorithm is capable of correctly measuring $NO_2$ after an adjustment of the $NO_2$ retrieval. We have shown that it is possible to adjust an atmospheric trace gas retrieval for the influence of a solar eclipse. Moreover, we are the first to provide evidence for an increase in $NO_2$ during a solar eclipse using space-based measurement techniques and to quantify this increase on a large scale with the same instrument. Our measurements can be used to test atmospheric chemistry models, possibly improving their sensitivity to solar eclipses but also artificial shadows on the Earth induced by sunlight-intercepting geoengineering approaches.

# Contents

# 1

# Introduction

Climate engineering is the artificial modification of the Earth's atmosphere-surface system and is nowadays considered a potential way to mitigate the effects of climate change. For example, management of the solar radiation is seen as a possible strategy to reduce the absorption of solar radiation at the Earth's surface and in the atmosphere. Stratospheric aerosol injection and placing sunshades in space are among the approaches suggested for solar radiation management (Lenton and Vaughan, 2009), where the focus is on reducing the net incoming shortwave radiation at the top of the Earth's atmosphere. However, such approaches could potentially impact atmospheric chemical processes which rely on and respond to the incoming sunlight. Twice a year on average, various degrees of solar obscuration can already be experienced at the Earth's surface. This occurs in the (partial) shadow of the Moon during a solar eclipse, leading to a reduced amount of received solar radiation. Studying the behaviour of atmospheric gasses during a solar eclipse could help to better understand the sensitivity of planetary atmospheres to variations in solar radiation and the potential short-term effects of sunlight-intercepting geoengineering approaches.

One of the possible short-term effects of solar eclipses on the atmosphere is an increase of $NO_2$ concentration. During the day, $NO_2$ and NO remain in equilibrium in the atmosphere as the conversions to and from $NO_2$ are balanced. However, in the absence of sunlight, $NO_2$ is dominantly present over NO, as $NO_2$ is destroyed under the influence of sunlight. Smooth transitions between daytime and nighttime can be observed due to the short time scale of several minutes at which these photochemical reactions take place. Indeed, because of those short time scales, the $NO_2$/NO ratio may also be affected by the faster reduction of sunlight during a solar eclipse. Adams et al. (2010) have already studied this effect during the solar eclipse on 1 August 2008 using ground-based measurements. Despite the convincing result of the influenced $NO_2$ concentration by the solar eclipse, this effect was only displayed for the single location of the ground-based measurements. Satellite-based measurements can greatly improve the understanding of the solar eclipse's impact on the atmosphere for a large area and can provide strong proof of $NO_2$'s sensitivity to sunlight based on an extensive set of data. Moreover, $NO_2$ concentration measurements influenced by a decreasing rate of incoming sunlight can contribute to the improvement of atmospheric- and climate models when it comes to the sensitivity of the atmospheric composition to variations in sunlight.

TROPOMI, on board the Sentinel-5 Precursor satellite launched in 2017, is a spectrometer measuring the air quality of the Earth globally every day (Veefkind et al., 2012). This instrumentation operates across an extensive range of wavelengths, from the ultraviolet (UV) to the short-wave infrared (SWIR), facilitating the measurement of various trace gasses, aerosols and clouds in the atmosphere. The combination of high spectral and spatial resolution, large signal-to-noise ratio and daily global coverage makes TROPOMI a unique observational tool for atmospheric composition studies. In terms of $NO_2$, TROPOMI contributes to quantifying the local air pollution as the spatial and temporal distributions of $NO_2$ can fluctuate strongly. During a solar eclipse, a large-scale increase in $NO_2$ concentration is observed in the measurements performed by TROPOMI. Figure 1.1 shows the $NO_2$ concentration during the solar eclipse of 10 June 2021 over Europe. In the orbit over Northern Europe where the solar

eclipse occurred, an increase in background $NO_2$ can be observed (between 20° and 40° longitude) in comparison to the adjacent orbit when there was not yet a solar eclipse. In the middle orbit, it shows an increase in $NO_2$ concentrations as it is influenced by the solar eclipse. Using the TROPOMI instrument to quantify the increase of $NO_2$ during a solar eclipse would be the first spaceborne evidence and analysis from space of a $NO_2$ increase during a solar eclipse.

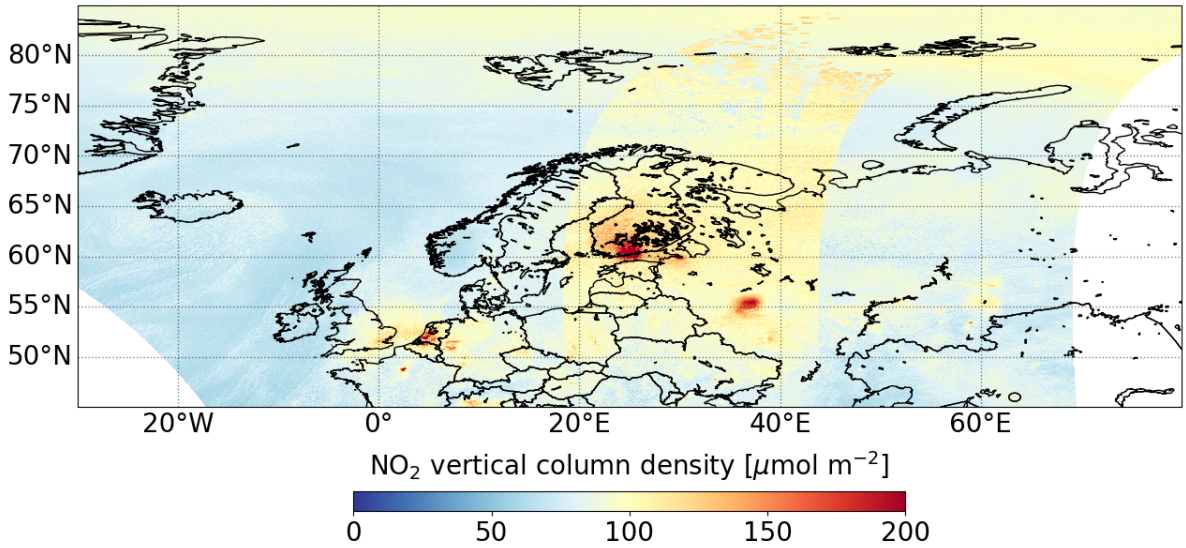


**Figure 1.1:** Map with $NO_2$ vertical column densities of 3 sequential orbits, including the orbit with solar eclipse.

However, the current $NO_2$ concentration measurements with TROPOMI during a solar eclipse cannot be trusted yet. The $NO_2$ concentration is retrieved from the Earth's top-of-atmosphere (TOA) reflectance spectrum, which is distorted during a solar eclipse, because of two reasons. First, the reduction of sunlight during a solar eclipse is not taken into account in the calculation of the TOA reflectance. This reduction depends on measurement time, location on the Earth's surface and wavelength (the latter due to solar limb darkening). Recently, it has been shown that an accurate calculation of this reduction allows for restoring the TOA reflectance at specific wavelengths (see Trees et al., 2021). Secondly, as the symmetry of the solar disk is broken during a solar eclipse, absorption features in the solar spectrum may be different than in a non-eclipse situation (see Fig. 2 of Adams et al., 2010). It remains to be shown how those phenomena affect the $NO_2$ concentration retrieval with TROPOMI, and to what extent the $NO_2$ increase observed in Figure 1.1 can be attributed to real changes in atmospheric chemistry.

The primary goal of this study revolves around two key objectives. Firstly, it aims to adjust the disrupted $NO_2$ measurements acquired by TROPOMI during eclipse occurrences. Specifically, the focus lies on refining the retrieval of $NO_2$ vertical column density, including both the troposphere and stratosphere. Secondly, this research aims to strengthen our comprehension of the photochemical processes governing $NO_2$ concentrations within the atmosphere through modelling the influences of a solar eclipse. A solar eclipse provides a unique setting to a controlled switch toggling sunlight on and off, providing an environment to analyse the photochemistry associated with these reactions. Consequently, the central research inquiry revolves around understanding the intricate relationship between solar eclipses and the resultant alterations in atmospheric photochemistry, measured on a large scale from space. The main research question therefore is:

***Can we find observational evidence from space of increased $NO_2$ concentration during solar eclipses?***

The formulated sub-questions following the main research question are:

**How do solar eclipses influence the current $NO_2$ retrieval?**
The reflectance spectrum changes significantly when parts of the incoming sunlight is blocked by the Moon. The influence on the spectrum and the observed $NO_2$ estimations will be shown.

**How can the $NO_2$ retrieval be improved such that it is not affected by solar eclipse related biases?**
The direct effect of the shadow of the Moon on the reflectance spectrum will be discussed, including how to adjust the retrieval for this. Consequently, the high-spectral-resolution features will be analyzed and corrected for so that they do not influence the $NO_2$ retrieval.

**What is the expected $NO_2$ concentration change during a solar eclipse?**
The expected $NO_2$ concentration will be modelled using pre-eclipse values for NO and $NO_2$, following the photochemical equilibrium equations. Additionally, the pre-eclipse values can be used in the comparison to the eclipse scenario to formulate the expected change in $NO_2$ concentration.

**How do the corrected $NO_2$ concentration measurements compare with the modelled $NO_2$ concentrations?**
The results from both the corrected concentration measurements and the modelled concentrations will be analysed and elaborated on whether they do or do not agree. Consequently, the degree of photochemistry and the observed change in $NO_2$ concentration can be analysed.

In Chapter 2 (Background), a comprehensive overview will be provided on atmospheric $NO_2$ and the capabilities of TROPOMI in measuring and monitoring $NO_2$ from a spaceborne perspective. This chapter will also delve into the Sun's influence and the impact of the sunlight on $NO_2$ measurements, particularly during solar eclipses. Subsequently, Chapter 3 (Problem Description) will focus on the solar eclipse cases, defining their specific characteristics and illustrating their corresponding impacts on $NO_2$ measurements. Chapter 4 (Methodology) will express the methodology employed in this study, encompassing the computation of obscuration fraction, adjustment applied to the $NO_2$ retrieval process and the modelling of $NO_2$ concentrations during solar eclipses. The intricacies of these processes will be demonstrated to provide a comprehensive understanding of the analytical framework. In Chapter 5 (Results and Discussion), the outcomes of the adjustments made and the model simulations conducted are presented, analysed and discussed. Through a detailed examination of the results, a nuanced understanding of the implications will be developed. Chapter 6 (Conclusion) will synthesize the key findings and present the overarching conclusions derived from this research. Finally, in Chapter 7 (Recommendations and Outlook), recommendations for further research endeavours will be discussed and an outlook on potential future concerns and topics within the domain will be provided.

# 2

# Background

In this Chapter, the behaviour and chemical background of the nitrogen dioxide concentrations in the atmosphere will be given (Section 2.1). Secondly, the monitoring and retrieval methods of these gasses as applied by TROPOMI will be further explained in detail (Section 2.2). Thirdly, the important features of the Sun and its resulting sunlight related to the measuring principles are described and explained (Section 2.3). Finally, the theory of solar eclipses is addressed, in addition to the influences it can induce (Section 2.4).

## 2.1. $NO_2$ in Earth's atmosphere

Nitrogen dioxide ($NO_2$) is a trace gas in our atmosphere and is, as part of the nitrogen dioxides ($NO_x$ = NO + $NO_2$), an important contributor to air pollution. The sources of $NO_x$ in Earth's atmosphere will be discussed in Subsection 2.1.1. The nitrogen oxides remain in balance through the photochemical equilibrium and this will be further elaborated in Subsection 2.1.2. Finally, the roles of $NO_2$ in the atmosphere are addressed in Subsection 2.1.3.

### 2.1.1. Sources of $NO_x$

$NO_x$ can be tracked down to several different sources. Overall, the main source of $NO_x$ in the troposphere is related to anthropogenic emission in the form of fossil fuel combustion. For fossil fuels, the combustion processes initiate the thermolysis of oxygen molecules, originating from clean air, which eventually leads to the formation of $NO_x$ in combination with N and $N_2$ (Jacob, 1999). During the combustion of coal, however, the formation of $NO_x$ does already occur without the contribution of clean air oxygen molecules. Most of these processes' emission initially occurs in the form of NO, whereafter it is transformed into $NO_2$ in the atmosphere. The thermolysis occurs when temperatures exceed 2000 K, which is also the reason why lightning arises as a natural source of $NO_2$. Biomass burning is another natural source of the emission of $NO_2$, but can also be induced again through anthropogenic activities. Soil is the last significant source of $NO_2$ as large fluctuations are seen after rain events over dry soils. The sources mentioned are mostly related to the tropospheric sources of NO and $NO_2$, whereas $NO_2$ in the stratosphere originates from a photochemical reaction where UV radiation fuels the oxidation of nitrous oxide ($N_2O$) to eventually form $NO_2$ (Crutzen, 1979). The origin of $N_2O$ is mainly from the soil, but as it is an inert gas it is able to travel up to the stratosphere without being involved in other chemical reactions throughout the atmosphere. Next to this naturally occurring source of $NO_2$, also a relatively small contribution is seen from high-flying aircraft which make up for the anthropogenic emission in the lower stratosphere.

### 2.1.2. Photodissociation of $NO_2$

In both the troposphere and stratosphere, the reaction from $NO_2$ to NO is mainly governed by the influence of sunlight, as follows (see, e.g., Adams et al., 2010):

$$NO_2 + h\nu \Rightarrow NO + O(^3P) \tag{2.1}$$

where $h\upsilon$ represents the available photons for photodissociation, within the photolysis region of 340-420 nm (where below 390 nm photolysis yields 100%). The photodissociation rate $J$ describes the rate of incoming photons and therefore indicates the possible rate of the photolysis reaction of Equation 2.1. Subsequently, the rate of incoming photons is related to the actinic flux, which is the irradiance integrated over all angles (Madronich, 1987). In Subsection 2.2.2 we will elaborate more on the definition of irradiance. The byproduct in Equation 2.1 is a single oxygen atom $O(^3P)$, which is also known as atomic oxygen (Crutzen, 1979). As this is a highly reactive atom, the new reaction with oxygen ($O_2$) to form ozone ($O_3$) quickly takes place according to:

$$O(^3P) + O_2 \Rightarrow O_3 \tag{2.2}$$

Finally, ozone reacts with NO again back to $O_2$:

$$NO + O_3 \Rightarrow NO_2 + O_2 \tag{2.3}$$

The availability of tropospheric ozone is limited, which is why Equation 2.2 is needed in the troposphere and consequently the $NO_x$ equilibrium alone will lead to a net production of ozone of zero. Meanwhile, due to the abundance of ozone in the stratosphere, the reaction of Equation 2.3 is not limited by Equation 2.2 and therefore Equation 2.3 will be able to constantly convert NO to $NO_2$ (Adams et al., 2010). The typical background profiles of the concentrations of $NO_2$ and $O_3$ through both the troposphere and stratosphere are shown in Figure 2.1.

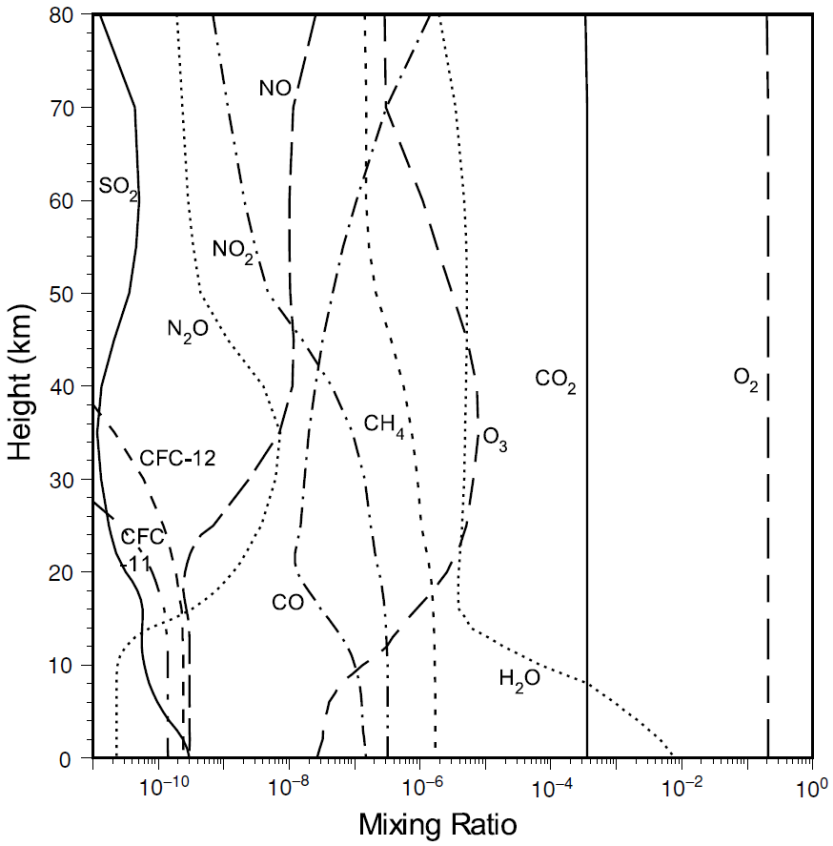


**Figure 2.1:** Representative vertical profiles of trace gasses, including $NO_2$ and $O_3$, during daytime (Liou, 2002).

In addition, Figure 2.1 shows insight into the $NO_2$/NO ratio over height concerning the natural state of photochemical equilibrium during daytime and the availability of NO to be converted to $NO_2$. Equation 2.1, Equation 2.2 and Equation 2.3 act on relatively short timescales of several minutes (Dessler, 2000). During daytime, it means that both $NO_2$ and NO are assumed to be in a photochemical equilibrium. As for the transition between day- and nighttime, the change in incoming sunlight results in a rapid increase of $NO_2$ concentration. Equation 2.1 will stop converting $NO_2$ to NO, while the NO to

$NO_2$ will still continue in Equation 2.3 (Dessler, 2000). As a result, almost all NO is converted into $NO_2$ at nighttime.

### 2.1.3. The roles of $NO_2$ in the troposphere and stratosphere

In the troposphere, nitrogen dioxide is a trace gas and is, as part of $NO_x$, an important contributor to air pollution. Within the mix of $NO_x$, $O_3$, particulate matter and $SO_2$ a close and complex coupling of all of its components exist which makes it hard to distinguish their individual contribution to air pollution. Nevertheless, evidence was presented that high $NO_2$ concentrations lead to an increase in respiratory diseases and can induce long-term damage to lungs (Sunyer et al., 1997; World Health Organization, 2003). In the troposphere, $NO_2$ acts as a catalyser for $O_3$ production (Sillman et al., 1990). Interaction with the $HO_x$ cycle results in a net increase of $O_3$, as this cycle 'steals' NO from the $NO_x$ cycle after Equation 2.1 to convert it to $NO_2$ without using any $O_3$ (Jacob, 1999). This way the $NO_x$ equilibrium is not disturbed, but no $O_3$ is used, consequently resulting in a net production of ozone. The presence of tropospheric ozone on the contrary, is not desirable as it contributes to air pollution similar to $NO_2$ and even is considered a mild greenhouse gas in the troposphere. The effect of $NO_2$ as a greenhouse gas is seen in a relatively low mean contribution to the radiative forcing of 0.05 W/m$^2$, but in heavily polluted areas can locally lead up to 2-4 W/m$^2$ (Shindell et al., 2009).

In the stratosphere, $NO_2$ is similarly in close relation to ozone. Ozone in the stratosphere is naturally an important component as it protects the surface of the Earth from harmful UV radiation. Stratospheric ozone is produced through the photolysis of oxygen in the UV wavelength region at wavelengths below 310 nm. This relation is the same as in Equation 2.2, however in the opposite direction and in addition UV radiation is added as a product (Crutzen, 1979). This results in the following equation:

$$O_3 + h\nu \Rightarrow O(^3P) + O_2 \tag{2.4}$$

Subsequently, as addressed in Subsection 2.1.1, the highly reactive $O(^3P)$ is also able to be used in the oxidation of $N_2O$ (see, e.g., Crutzen, 1979):

$$O(^3P) + N_2O \Rightarrow 2NO \tag{2.5}$$

At last, the formation of $NO_2$ is probable since the NO resulting from this oxidation is transformed to $NO_2$ with the use of $O_3$ in the described photodissociation equilibrium of $NO_x$ and Equation 2.3. In the stratosphere, this mainly means that $NO_2$ can introduce the net loss of stratospheric ozone (Dessler, 2000) since more $O_3$ is used up than created as the result of UV radiation and photodissociation. On a global scale, $NO_2$ can be observed and monitored with the use of satellites, creating the possibility to analyse these roles and influences $NO_2$ has on the atmosphere and its components.

## 2.2. Monitoring $NO_2$ concentrations from space

Measuring $NO_2$ on a global scale but still with a relatively high spatial resolution on a daily basis is key to being able to monitor the different influences of $NO_2$ on ozone, air pollution and climate change as discussed in Section 2.1. In the following sections details about TROPOMI (Subsection 2.2.1) will be addressed and the $NO_2$ retrieval procedure (Subsection 2.2.2 and Subsection 2.2.3) will be described.

### 2.2.1. TROPOMI

TROPOMI is short for the Tropospheric Monitoring Instrument and is onboard the Sentinel-5 Precursor (S5P) satellite. Its mission is to measure and provide relevant information on air quality and climate forcings (Veefkind et al., 2012). This includes trace gas concentrations, aerosol properties and information about the ozone layer. Before the launch of the satellite in October 2017, several satellite missions preceded the S-5 P mission with similar atmospheric composition research goals. SCIAMACHY (SCanning Imaging Absorption spectroMeter for Atmospheric CartograpHY) (Van Geffen et al., 2021) and OMI (Ozone Monitoring Instrument) (Van Geffen et al., 2021) have been providing daily measurements for over 20 years as precursors to the Sentinel-5 Precursor. The higher spatial resolution of TROPOMI of 5.5 km by 3.5 km and the improved signal-to-noise ratio, which can be up to three times higher, and the extended range in measurable wavelengths are major improvements compared to its predecessors (Veefkind et al., 2012).

To be able to deliver this continuous amount of data, S5P flies in a sun-synchronous orbit around the Earth with an inclination angle of $98.7°$. Having a swath of 2600 km wide and a sampling rate of 0.8 seconds, which translates to moving for 5.5 km in the along-track direction, the satellite can fly 14 orbits in one day (Veefkind et al., 2012). These 14 orbits per day make it possible to deliver global coverage for each day. The repeat cycle of 16 days realises a repetition of a specific orbit within that period. The satellite is flying an ascending node orbit where it crosses the local equator at 13.30 h mean local solar time in every orbit, making early afternoon measurements with an always illuminated surface of the Earth.

The sun-synchronous is important as the instrument used is an imaging spectrometer, which gives its results based on the reflected sunlight. The spectrometer can measure the ultraviolet (UV), visible (VIS), near-infrared (NIR) and shortwave-infrared (SWIR) ranges of the wavelength spectrum (Veefkind et al., 2012). These multiple regions are necessary to be able to measure different trace gasses and aerosols in the atmosphere, as each atmospheric constituent shows its response within different wavelength ranges. This is demonstrated in Figure 2.2, where the preceding satellites and their ranges are also shown. In comparison with the most recent satellite OMI, the additional ranges NIR (758-770 nm) and SWIR (2305-2385 nm) respectively add more information on clouds and the concentrations of CO and $CH_4$, for TROPOMI (Veefkind et al., 2012).

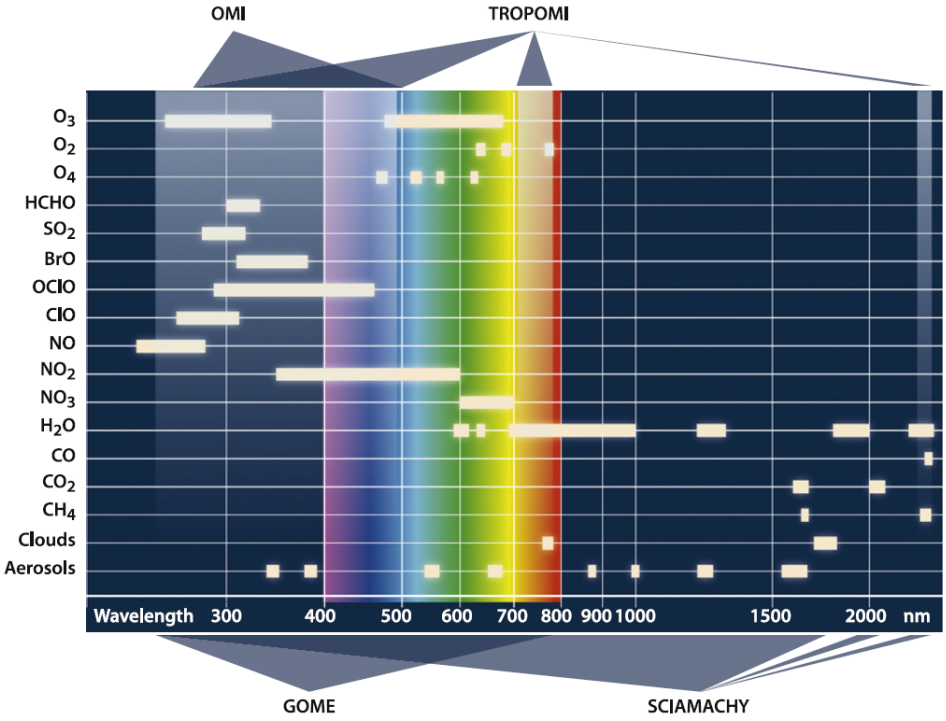


**Figure 2.2:** Wavelength ranges from TROPOMI and its predecessors (Veefkind et al., 2012).

A spectrometer is thus an instrument which can split light into different colours or wavelength regions, based on their specific wavelengths. As the S5P satellite is pointed towards the Earth's surface, it measures the sunlight being reflected by the Earth. The reflected light has passed through Earth's atmosphere as it travels from the surface up to the satellite, where the atmospheric constituents as trace gasses and aerosols have altered the way the light travels through scattering or absorption. As seen in Figure 2.2 the trace gasses all have their specific wavelength range in which they absorb the light. The spectrometer is thus able to very specifically choose the ranges where the gas of interest is active. For $NO_2$ this means that the default wavelength window is from 405 nm to 465 nm which is used in the $NO_2$ retrieval.

### 2.2.2. $NO_2$ retrieval

The $NO_2$ retrieval done by TROPOMI has been based on a similar type of approach as done by OMI, SCIAMACHY and GOME satellites (Van Geffen et al., 2021). This approach starts with measurements of the radiance and irradiance done by TROPOMI, from which the reflectance is computed. The reflectance is then processed into a $NO_2$ slant column density through the use of the DOAS method. In spaceborne DOAS, the reflectance is related to the extinction of light by scattering and absorbing species along the average photon path between the Sun and satellite instrument (Van Geffen et al., 2021). Consequently, the retrieved slant column density is converted to a vertical column density with the use of the air mass factor, which describes the dispersion of light through the atmosphere. A concise overview of the $NO_2$ retrieval is shown in Figure 2.3.

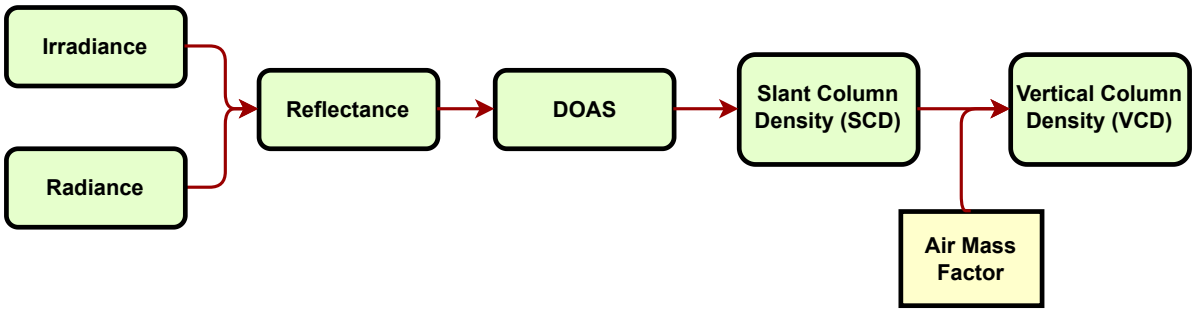


**Figure 2.3:** Schematic of the $NO_2$ retrieval workflow.

The fundamental principle of the retrieval is focused on the fraction of the sunlight reflected by the Earth (radiance, $I$) in comparison to the direct sunlight (irradiance, $E_0$), as measured by the satellite. The measured radiance originates from the top of the atmosphere and is described as the radiative energy flux in a particular direction. The radiance units are W $m^{-2}$ $nm^{-1}$ $sr^{-1}$. The irradiance is measured once per day when TROPMI measures the sunlight directly (Van Geffen et al., 2021) and is the integral of the weighted radiance with the resulting units W $m^{-2}$ $nm^{-1}$:

$$E = \int_0^{2\pi} \int_0^1 I(\mu, \phi) \mu d\mu d\phi \tag{2.6}$$

with the viewing zenith angle $\mu$ and azimuth angle $\phi$. $E_0$ is the solar irradiance perpendicular to the direction of incident sunlight at the top of the atmosphere. When comparing the radiance and irradiance with each other, the ratio of radiance per irradiance, which is known as the reflectance, is analyzed and modelled. By modelling different concentrations of multiple gasses, the measured reflectance can be obtained as close as possible, which finally results in a given concentration for the gasses of interest. Subsequently, the analysis describes the composition of the Earth's atmosphere as absorption and scattering within different wavelength ranges can be linked to specific gasses present in the atmosphere. This process is called the Differential Optical Absorption Spectroscopy (DOAS) method (Platt and Stutz, 2008).

Here, the actinic flux as mentioned in Subsection 2.1.2 is not considered, since the $NO_2$ retrieval is part of a broader collection of trace gasses that are retrieved via the DOAS method. Not all of these trace gasses are photochemically active, which is why the actinic flux would not be applicable for the DOAS method.

#### The DOAS method

The theory related to the DOAS method starts with the Lambert-Beer law, where the atmosphere's components can act as absorbers or scatterers as photons travel through the atmosphere (Platt and Stutz, 2008). Three fundamental building blocks for the Lambert-Beer law are the intensity of light before and after the extinction by absorption or scattering, $I_0$ and $I$, respectively, the path length and the concentration of the absorbers (Wypych, 2015). The influence of the atmosphere can be combined in one variable, which in this case is shown as $\tau(\lambda)$ and is known as the slant optical thickness spectrum (Platt and Stutz, 2008), in which $\lambda$ represents the wavelength of light in nm. As the Lambert-Beer law is applied to the spectra, the result is as shown in Equation 2.7:

$$I(\lambda) = I_0(\lambda) \cdot e^{-\tau(\lambda)} \tag{2.7}$$

The polynomial $P(\lambda)$ is now needed to separate the spectrally smooth influences, originating from the air- and cloud molecules and the aerosols, from the spectrally varying components of interest, originating from the trace gasses. The polynomial is represented by a low-order polynomial of, e.g., 3rd degree. After the subtraction of a polynomial $P(\lambda)$, the differential slant optical thickness spectrum $\tau^*(\lambda)$ is obtained, as shown in Equation 2.8:

$$\tau^*(\lambda) = ln\left(\frac{I_0(\lambda)}{I(\lambda)}\right) - P(\lambda) \tag{2.8}$$

The values of $\tau(\lambda)$ represent the attribution of trace gasses which are highly wavelength dependent and thus show variations in the spectrum with a high spectral resolution (Platt and Stutz, 2008). It consists of different trace gasses that absorb at wavelengths within the wavelength range of interest and contribute to $\tau^*(\lambda)$ by their differential absorption cross section $\sigma^*(\lambda)$ (in $cm^2$/molecule) and their slant column density $N_s$ (in molecules/$cm^2$) as shown in Equation 2.9:

$$\tau^*(\lambda) = \sum_j \sigma_j^*(\lambda) \cdot N_{s,j} \tag{2.9}$$

Here a total of $j$ absorbing gasses is considered. The differential absorption cross sections ($\sigma^*$) are known through measurements performed in laboratories and are only very little affected by small temperature changes (Van Geffen et al., 2021). Finally, both Equation 2.8 and Equation 2.7 are equalized in Equation 2.10:

$$ln\left(\frac{I_0(\lambda)}{I(\lambda)}\right) = P(\lambda) + \sum_j \sigma_j^*(\lambda) \cdot N_{s,j} \tag{2.10}$$

Then, Equation 2.10 is optimized through, for example, optimal estimation such that the difference within the equation becomes as small as possible. As the best optimization is reached, the best-fitting slant column density ($N_s$) is determined for each trace gas.

### TROPOMI implementation of DOAS

In the previous section, the DOAS method was described. Here, the implementation for TROPOMI is discussed, as a few technical aspects are added. First, the data product structure used in the TROPOMI processing chain should be addressed. The radiance and irradiance are both presented with their own Level-1 file. The Level-1 files contain the top of the atmosphere radiance or irradiance. The radiances and irradiance are geo-located and so can already be visualized on the coordinate grid of the orbit as a pixel. Using these 2 files, the DOAS calculations can be performed and the final column concentration products will be gathered in a Level-2 file, where all relevant parameters will also be geo-located.

The reflectance by TROPOMI at the top-of-atmosphere (TOA) is measured as follows:

$$R_{\text{meas}}(\lambda) = \frac{\pi I(\lambda)}{\mu_0 E_0(\lambda)} \tag{2.11}$$

where $I(\lambda)$ again is the radiance in W $m^{-2}$ $nm^{-1}$ $sr^{-1}$, $E_0(\lambda)$ is the extraterrestrial irradiance perpendicular to the beam in W $m^{-2}$ $nm^{-1}$ and $\mu_0 = cos(\theta_0)$, with $\theta_0$ the solar zenith angle, to match the correct angular orientation of the radiance (Van Geffen et al., 2021). Similar to the original DOAS theory, to solve for the slant column density of $NO_2$, a modelled reflectance will need to be computed to minimize the difference compared to the measured reflectance. The modelled reflectance $R_{\text{mod}}$ approach for TROPOMI is shown in Equation 2.12.

$$R_{\text{mod}}(\lambda) = P(\lambda) \cdot exp\left[-\sum_{k=1}^{n_k} \sigma_k(\lambda) \cdot N_{s,k}\right] \cdot \left(1 + C_{\text{ring}} \frac{I_{\text{ring}}(\lambda)}{E_0(\lambda)}\right) \tag{2.12}$$

$$P(\lambda) = \sum_{m=0}^{n_p} a_m \lambda^m \tag{2.13}$$

Similar to Equation 2.10, Equation 2.12 comprises a polynomial term. The polynomial term is shown in Equation 2.13, where the order of the polynomial, $n_p$, is usually equal to 5 for the TROPOMI processor (Van Geffen et al., 2021). The polynomial term here is used to filter out the spectrally smooth features and be able to only use the highly variable spectral features related to the absorption by the trace gasses. The parameters $\sigma(\lambda)$ and $N_s$ are related to the properties of the trace gasses. The absorption cross sections $\sigma(\lambda)$ can be visualized as the reference spectra related to the specific atmospheric component. Figure 2.4 shows the reference spectrum of $NO_2$, which was measured by Vandaele et al. (1998) in a laboratory.

Another addition in the approach for the modelled reflectance $R_{\text{mod}}$ can be seen in the last term, where the Ring effect is included. The Ring fitting coefficient $C_{\text{ring}}$ and Ring spectrum $I_{\text{ring}}$ are of importance for this matter. The Ring effect describes molecular scattering that consists of Rayleigh scattering and vibrational Raman scattering (Chance and Spurr, 1997). This affects the observed spectral radiance spectrum and therefore needs to be adjusted. The computation of the Ring spectrum is based on the spectral irradiance, which is why a reference spectrum of the Sun is needed. In Section 2.3 the reference spectrum of the Sun will be addressed in further detail.

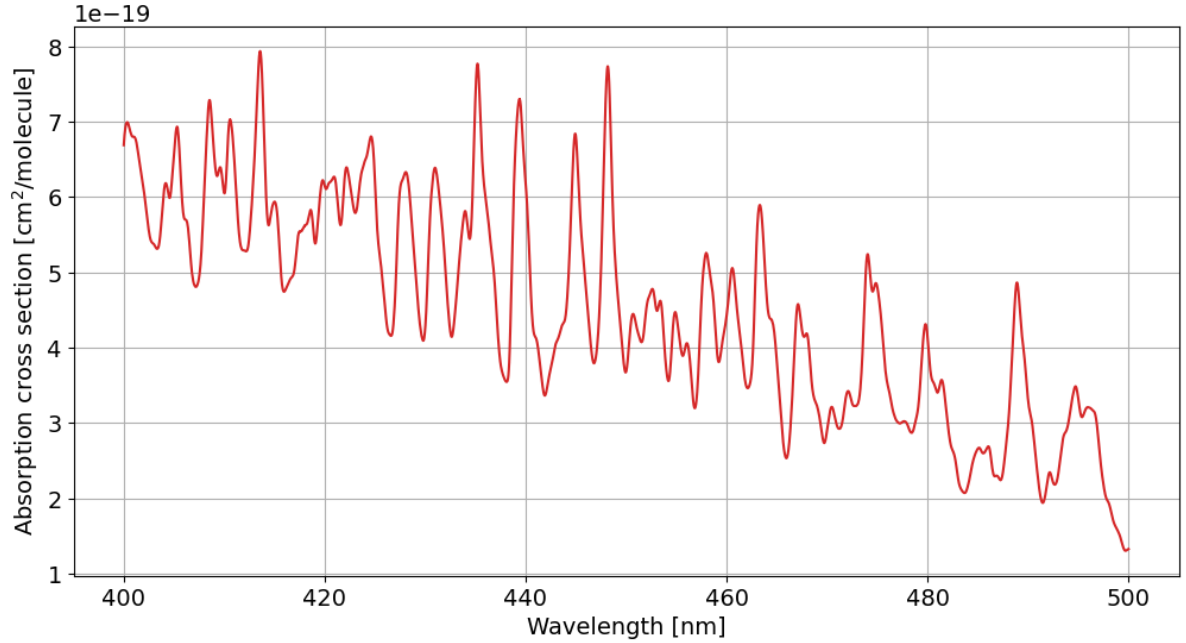


**Figure 2.4:** The $NO_2$ reference spectrum (Vandaele et al., 1998; Van Geffen et al., 2021).

The quality of the spectral fitting can be assessed by analyzing the residual of the fit, denoted as $R_{\text{res}}(\lambda)$. The value of $R_{\text{res}}(\lambda)$ is derived from the difference between the measured reflectance and the modelled reflectance, as follows (see Van Geffen et al., 2021):

$$R_{\text{res}}(\lambda_i) = R_{\text{meas}}(\lambda_i) - R_{\text{mod}}(\lambda_i) \tag{2.14}$$

$R_{\text{res}}(\lambda)$ essentially measures how well the spectral fitting process performed. Together with the signal-to-noise ratio (SNR), $R_{\text{res}}(\lambda)$ helps to determine the best fit for the modelled reflectance. The SNR represents the noise in the reflectance ($\Delta R_{\text{meas}}(\lambda_i)$), which depends on both the radiance noise ($\Delta I(\lambda_i)$) and the irradiance noise ($\Delta E_0(\lambda_i)$), as described in:

$$\Delta R_{\text{meas}}(\lambda_i) = \frac{1}{E_0(\lambda_i)} \sqrt{(\Delta I(\lambda_i))^2 + (\Delta E_0(\lambda_i))^2 \cdot (R_{\text{meas}}(\lambda_i))^2} \tag{2.15}$$

The best fit for the modelled reflectance is determined by minimizing the chi-squared function $\chi^2$ (Van Geffen et al., 2021):

$$\chi^2 = \sum_{i=1}^{n_\lambda} \left( \frac{R_{\text{res}}(\lambda_i)}{\Delta R_{\text{meas}}(\lambda_i} \right)^2 \tag{2.16}$$

The optimization process is performed through an optimal estimation as elaborated by Rodgers (2000). After the optimal $R_{\text{mod}}$ is determined for which the chi-squared function is as low as possible, the modelled reflectance returns a $NO_2$ slant column density. Furthermore, the precision of the slant column density, the chi-squared value and the other measure which describes the goodness of the fit, the root-mean-square error, are shared.

The processing chains also include some additional constraints regarding the quality of the processed pixels. First, processing quality flags are already present in the Level-1 files. Depending on whether this flag is a warning or an error, the pixel could already be left out of the DOAS processing as it is assumed to be too bad of quality. Typical errors that could lead to this outcome are *radiance missing*, *irradiance missing*, *solar zenith angle range error* and *signal to noise ratio error* (Eskes et al., 2022). Secondly, during the DOAS processing one other termination can occur. As the residual reflectance $R_{\text{res}}$ is being computed during each iteration of the modelled reflectance $R_{\text{mod}}$, the residual reflectance is being analyzed on the number of outliers on the spectral domain. This process of outlier removal is called spike removal and is focused on removing strong outliers outside of certain boundaries (Van Geffen et al., 2021). Spectral pixels are then removed from the residual and the DOAS process is repeated. In this second DOAS fitting run, the spike removal is not incorporated to avoid ending up in a cycle (see Appendix F of Van Geffen et al., 2021). Unfortunately, the entire pixel is not processed again if the number of outliers exceeds 10 once more, but the pixel is skipped as it is deemed to be too bad to give a reliable outcome.

### Air mass factor

The slant column does not only include the light which travels in a straight line from the Earth to the satellite but also contains scattered light. Photons are scattered in multiple directions and are for that reason also able to, for example, jump from one path to the other path when travelling halfway of the atmosphere (Lorente et al., 2017). The air mass factor is a variable that converts the slant column densities ($N_{\text{s}}$) into vertical column densities ($N_{\text{v}}$) as follows (see Eq. 12 of Van Geffen et al., 2021):

$$N_{\text{v}} = \frac{N_{\text{s}}}{M} \tag{2.17}$$

The different components of the air mass factor are: altitude-dependent air mass factor $m_l$ (unitless), the column density profile $v_l$ (in molecules/cm$^2$ per layer) and the temperature correction profile $c_l$ (unitless). This relation is shown in Equation 2.18 (see Van Geffen et al., 2021, Eq.13):

$$M = \frac{\sum_l m_l v_l c_l}{\sum_l v_l} \tag{2.18}$$

Next to the solar zenith angle and viewing zenith angle, other variables also have their influence on the way light behaves in the atmosphere. These variables for example include surface albedo, vertical temperature and $NO_2$ profiles (Chimot et al., 2016). The surface albedo is coupled together with the earlier mentioned solar- and viewing zenith angles. With a radiative transfer model, these variables are translated into their influence on the air mass factor (Van Geffen et al., 2021). The resulting altitude-dependent air mass factors are transformed into a look-up table, where output is generated as a function of the input variables. The altitude-dependent air mass factor, $m_l$ is the first component of the air mass factor as shown in Equation 2.18. The vertical profiles are of importance to be able to discriminate the significance of a specific layer concentration and temperature when converting the slant density contribution to the vertical density contribution of $NO_2$. The column density profile shows the relative contribution of $NO_2$ concentration in the different atmospheric layers. The temperature correction profile is relevant for the cross-section of $NO_2$, as this changes the absorption capabilities of $NO_2$ and is influenced by the temperature (Vandaele et al., 1998).

### 2.2.3. The TM5 atmospheric chemistry model

The TM5 model is a detailed three-dimensional global atmospheric chemistry transport model that creates the ability to closely simulate and analyse the chemical composition of the Earth's atmosphere (Krol et al., 2005; Huijnen et al., 2010). With the use of estimated weather forecasts, deposition and emissions, a comprehensive chemistry model can compute concentrations of various gasses in the atmosphere. The model produces these concentrations on a grid with a standard resolution of one by one degree (Van Geffen et al., 2021) and consists of 34 vertical layers, where the top of the highest layer is fixed for a pressure of 0.1 hPa (Huijnen et al., 2010). The meteorological inputs used in the TM5 model originate from the ECMWF operational forecast data, which are regridded to a one by one degree dataset (Krol et al., 2005) and stored to be used as three-hourly inputs. The full list of meteorological parameters can be found in the paper by Huijnen et al. (2010). Concerning the chemical model itself, all the reactions and the related rates of the trace gasses can be found in the chemical scheme presented in Huijnen et al. (2010). The photolysis reactions are also included in the chemical model. Additionally, the emissions of anthropogenic, biogenic and biomass origin are included as yearly totals. The emission inputs are implemented through a 0.5 by 0.5 degrees resolution grid with a temporal monthly resolution. As the emissions differ in origin, and so also differ in injection into the atmosphere, the emissions are applied separately to be able to differentiate between different emission heights (Huijnen et al., 2010). The considered anthropogenic $NO_2$ emissions for this research are for example injected in the surface layer, the first layer of the total 34 layers.

The TM5 model delivers the stratospheric $NO_2$ column for the TROPOMI processing, but this originates from the total column calculation which contains all 34 atmospheric layers. Next to these column concentrations, the calculation of air mass factors, as discussed Equation 2.2.2, uses several parameters like $NO_2$ profile, temperature profile and pressure profile (Van Geffen et al., 2021). Within the TM5 model, these parameters are known for each layer at every pixel and are used in the computation of the air mass factor needed for the conversion from slant column to vertical column. Additionally, since the model contains these 34 layers of the atmosphere, it creates the opportunity for this research to apply and compare eclipse correction(s) to the layered $NO_2$ values before analysing the total column.

## 2.3. The solar spectrum

The $NO_2$ retrieval as described in Subsection 2.2.2 is based on sunlight reflected by the Earth. Here, we discuss in detail the properties of the incoming sunlight, starting with the description of the structure of the Sun in Subsection 2.3.1. Secondly, the spectral lines in the solar reference spectrum will be addressed in Subsection 2.3.2. Lastly, the phenomenon of solar limb darkening will be described in Subsection 2.3.3.

### 2.3.1. Vertical structure of the Sun

To be able to correctly interpret the varying spectra related to the light we receive on Earth, it is important to understand the source of sunlight, which is the Sun. The structure and properties of the Sun present knowledge about the origin of the sunlight and why it behaves the way that it does.

The irradiance from the Sun in the visible part of the spectrum mostly originates from the photosphere of the Sun. The photosphere is considered to be the first layer of the Sun's atmosphere above the Sun's 'surface'. While the Sun is a gaseous body and therefore does not contain a solid surface, the surface of the Sun is defined by the difference in heat transfer mechanism of the interior and the atmosphere of the Sun (Liou, 2002). Directly below the surface, the heat transfer is organised through convection, while above the surface heat is transported through electromagnetic radiation, as illustrated in Figure 2.5. Subsequently, the atmosphere's first layer is the photosphere, where photons escape from the Sun's surface into the solar atmosphere and beyond (Chitta et al., 2020). The chromosphere is a turbulent part of the Sun's atmosphere, where the magnetic fields play an important role concerning the dynamics of the change from photosphere to chromosphere and eventually to the outer layer of the Sun, the corona (Phillips, 1995). The photosphere is a relatively thin layer of 500 km, while the next atmospheric layer, the chromosphere, extends to a thickness of 2000 km. This is illustrated in Figure 2.5.

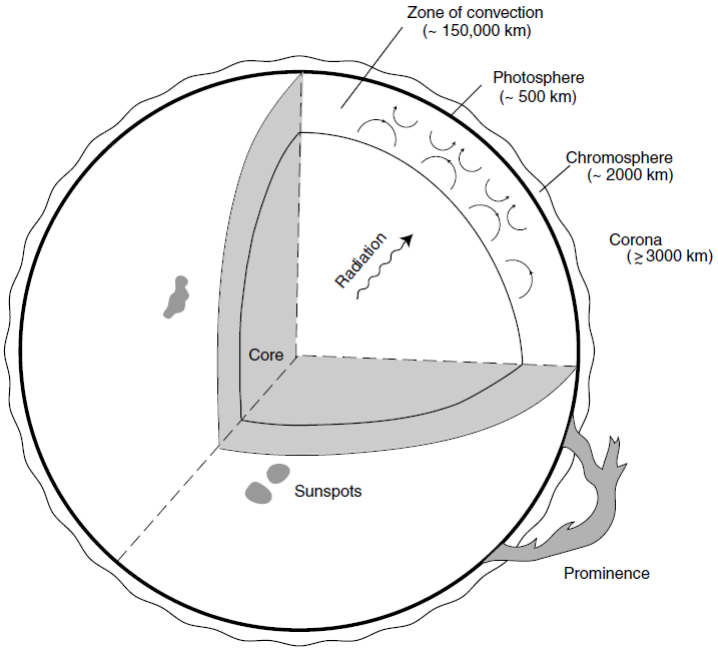


**Figure 2.5:** A schematic showing the cross-section of the Sun including the interior and the atmosphere. The photosphere is represented by the thick black line and the chromosphere is between this line and the outer wavy pattern (not to scale) (Liou, 2002).

Although the photosphere is relatively thin, it is the main source of the visible radiation we receive on Earth. This is caused by the high temperature in this layer and the positive relationship between temperature and emission flux. The maximum temperature reached in the chromosphere is still lower than the highest temperature in the photosphere, present at the lowest part of the photosphere (Liou, 2002), as can also be seen in Figure 2.6. Therefore, the chromosphere consists of relatively cool gasses in comparison to the hotter gasses in the photosphere. Consequently, the cooler gasses in the chromosphere are able to absorb radiation that is emitted in the photosphere. This causes the solar absorption spectrum to contain the absorption lines as they are known (Liou, 2002). The temperature profile through the photosphere and the chromosphere and the regions of specific absorption lines are shown in Figure 2.6. Pay close attention to the fact that here the regions of the absorption lines are shown, which are different than the emission lines that will be discussed in Subsection 2.3.2.

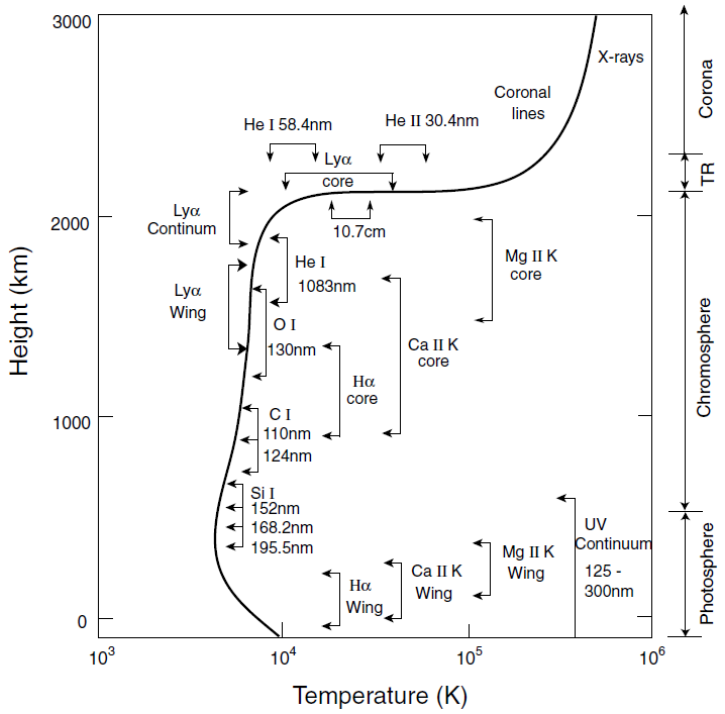


**Figure 2.6:** A schematic showing the cross-section of the Sun's atmosphere, with the height (in km) versus the temperature (in Kelvin). Note that the shown atoms and their respective wavelength regions are related to the absorption lines that are visible in the wavelength spectrum (Liou, 2002).

### 2.3.2. Spectral lines

Through the wavelength spectrum of light, we can distinguish atmospheric features that attenuate as the light passes through or by it. Before sunlight reaches the Earth's atmosphere, the light is attenuated by the influence of the Sun. Therefore, a portion of the spectral lines that are visible within the wavelength spectrum originate from the Sun. The understanding of the origin of these spectral lines is key for interpreting the results of altered sunlight.

The chromosphere is the part above the photosphere which during non-eclipse conditions cannot be seen from Earth as the energy released by the photosphere dominates the light we receive. The chromosphere absorbs part of the energy coming from the photosphere, which in turn is emitted again due to the abundant amount of hydrogen present in the chromosphere (Liou, 2002). Subsequently, the spectral origin of the emission is in the wavelength ranges where hydrogen atoms are active, which can be seen in Figure 2.6 where the H$\alpha$ core between 110 nm and 130 nm is shown as a region with absorption lines for the hydrogen atoms. Hydrogen atoms being active in this sense means electrons jumping down from one energy level towards another energy level within the hydrogen atom. With the jump down to another level, a certain energy change is considered and the energy change is compensated by an emission of a photon (Liou, 2002). This photon is what comes up as a Balmer line in the spectrum we analyze. Within the visible spectrum, 4 Balmer lines are present and several more show up in the ultraviolet spectrum below 400 nm (Wood, 1922). The overall trend is that the intensity of the Balmer lines tends to decrease with decreasing wavelength. The relevant Balmer lines and their corresponding wavelengths are shown in Table 2.1.

| Name | Wavelength [nm] |
|---|---|
| Balmer-$\alpha$ (H$\alpha$) | 656.3 |
| Balmer-$\beta$ (H$\beta$) | 486.1 |
| Balmer-$\gamma$ (H$\gamma$) | 434.0 |
| Balmer-$\delta$ (H$\delta$) | 410.2 |
| Balmer-$\varepsilon$ (H$\varepsilon$) | 397.0 |
| Balmer-$\zeta$ (H$\zeta$) | 388.9 |

**Table 2.1:** The specific Balmer lines and the wavelengths they occur at (Kramida, 2010).

The Balmer lines as they show up in the spectral irradiance spectrum of the Sun, however, do not represent themselves as emission lines but as absorption lines. This relates to the fact that radiation from the photosphere dominates the spectrum and therefore only the absorption is noticed in the spectrum instead of the emission by the chromosphere. Nonetheless, with possibly changing spectra during solar eclipses, this influence might change around the observation. This will be discussed in Subsection 2.4.2. As seen in Figure 2.7, the presented Balmer lines H$\delta$, H$\gamma$ and H$\beta$ show up as absorption lines in the spectrum.

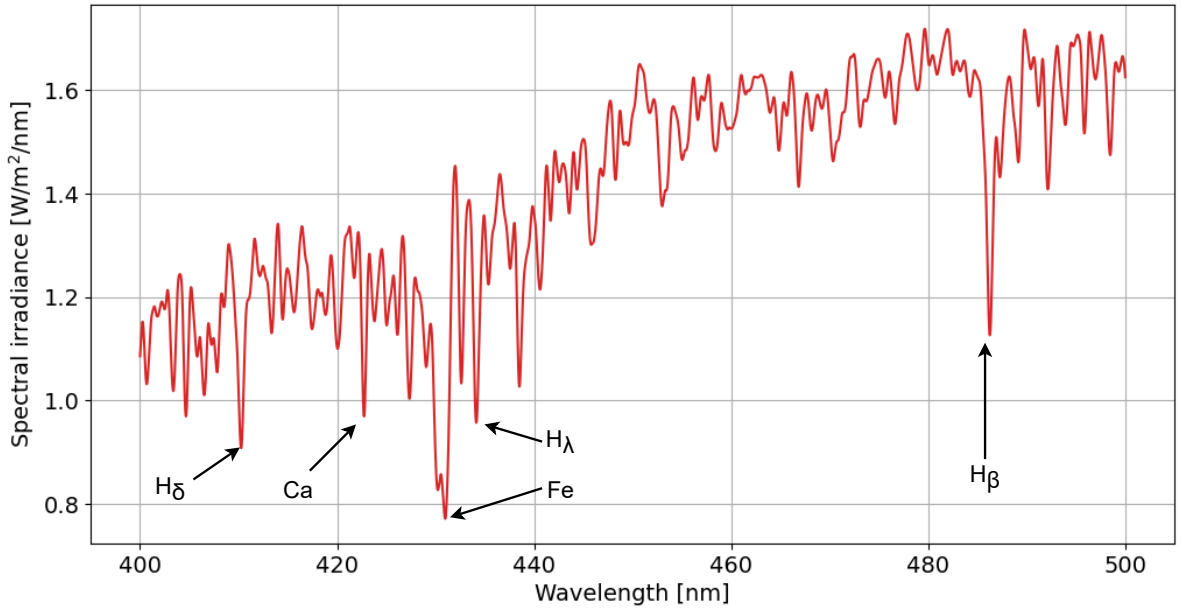


**Figure 2.7:** The spectral irradiance of the solar spectrum. Annotations show the associated influence of the resulting spectra lines (Chance and Kurucz, 2010; Van Geffen et al., 2021).

### 2.3.3. Solar limb darkening

When only considering a portion of the light originating from the solar disk instead of all the light, it is important to recognise the difference in intensity of light across the solar disk. This difference is described by solar limb darkening, where the edges of the Sun show less bright colours than the centre of the Sun. During solar eclipses, this change in intensity plays an important role.

In the TROPOMI algorithm, the solar radiation received at the Earth is considered and taken as an average for the entire solar disk for every wavelength. However, radiation originating from the photosphere differs in magnitude across the Sun's disk when looking at the Sun. When looking directly towards the middle, we see deepest into the photosphere of the Sun, which is relatively the hottest, as seen at 0 km height in Figure 2.6, and therefore emits a relatively bright signal (Liou, 2002). When looking more towards the outside edges of the solar disc, the light we see is from less deep into the photosphere, where the Sun's atmosphere is slightly colder and therefore less bright. This phenomenon is called solar limb darkening (Koepke et al., 2001). Due to the different emission temperatures, accord-

ing to Wien's displacement law, the solar limb darkening effect is also wavelength dependent (see, e.g. Trees et al., 2021), since radiation emitted at relatively higher temperatures will be visible at shorter wavelengths than radiation emitted at relatively lower temperatures. Figure 2.8 shows an image taken of the Sun where the intensity of the brightness across the solar disk shows the solar limb darkening.

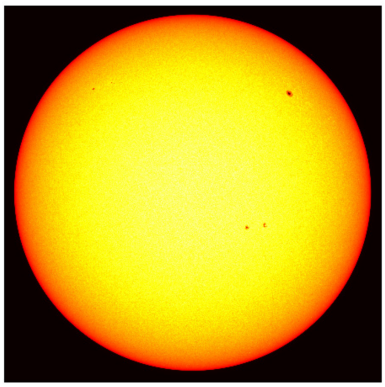

**Figure 2.8:** Solar image of the photosphere showing the solar limb darkening effect through the intensity of the brightness (Image taken on January 3, 2011, by SDO/HMI) (Moon et al., 2017).

## 2.4. Solar eclipses

The behaviour of the Sun and the corresponding incoming sunlight, without any influence of solar eclipse or other phenomena, was covered in Section 2.3. The following sections will describe the different Moon shadow types that can occur during a solar eclipse (Subsection 2.4.1). Secondly, the influence on the solar spectrum during a solar eclipse will be discussed (Subsection 2.4.2). Finally, the potential influence on the $NO_2$ concentrations in the atmosphere of a solar eclipse will be addressed (Subsection 2.4.3).

### 2.4.1. Moon shadow types

To get an understanding of the different light conditions during a solar eclipse, the various phases of the solar eclipse need to be considered. This can be described by the different types of Moon shadows that can occur during a solar eclipse.

A solar eclipse happens when the Moon aligns between the Sun and the Earth. A shadow of the Moon is cast onto the Earth's surface as a part of the light originating from the Sun is blocked. This creates different types of shadows: umbra, antumbra and penumbra (see, e.g., Trees et al., 2021). The shadows are visualized in Figure 2.9. The darkness of the shadows can be expressed in terms of their obscuration fraction $f_o(\lambda)$: the fraction of the sunlight that is blocked by the Moon (Seidelmann, 1992). The umbra is present when a total solar eclipse happens and the Moon fully occults the solar disk at $f_o(\lambda) = 1$. Depending on the distances between the Earth and the Sun, and between the Earth and the Moon, the umbra can occur on the surface of the Earth, or in space between the Earth and the Moon (Meeus, 1989). The antumbra appears on the Earth's surface during an annular eclipse when the Moon blocks the centre part of the solar disk but the solar limb is still visible (the so-called 'ring of fire'), such that $0 < f_o(\lambda) < 1$ holds as the outer edges of the Sun are visible. The shadow outside of the umbra and antumbra is called the penumbra and always occurs during partial, annular and total solar eclipses. Here the Moon does not fully occult the Sun and therefore also $0 < f_o(\lambda) < 1$ holds. The (ant)umbra, when present on the Earth's surface, is only a very small portion (commonly < 0.02%) of the lunar shadow (see Trees et al., 2021).

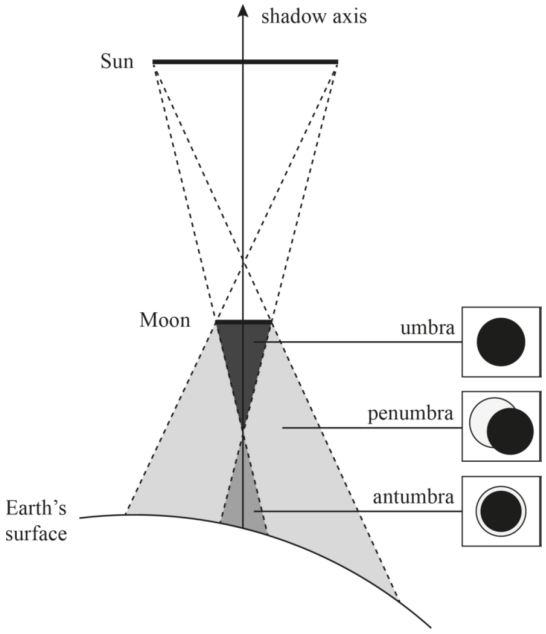


**Figure 2.9:** Shadow types during a solar eclipse (not to scale) (Trees et al., 2021).

### 2.4.2. Solar eclipse influence on the solar spectrum

When a solar eclipse takes place, the part of the solar disk responsible for the irradiance that is received on Earth changes as the Moon shifts in front of the Sun. As discussed in the previous paragraph, during non-eclipse scenarios, the sunlight we receive is dominated by the light originating from the photosphere and only a very tiny contribution originates from the chromosphere at the edges of the Sun, but this contribution is negligible. During a solar eclipse, however, the effective height of the Sun's atmosphere that is visible to us changes. The relative contribution from the photosphere versus the chromosphere therefore changes, and the wavelength spectrum shifts from mainly seeing absorption lines to seeing emission lines originating from the chromosphere. Depending on the specific geometry of each specific solar eclipse, this change in contribution can change the resulting irradiance received and its corresponding wavelength spectrum.

Ground-based observations during a solar eclipse indeed reported a changed irradiance spectrum compared to non-eclipse conditions. The research conducted by Adams et al. (2010) also confirms the different solar spectra resulting from varying contributions of the chromosphere. They stated that when only the outer region of the solar disk is covered by the Moon (less than 20%-30%) the contribution of the Balmer lines decreases. Past the 20%-30% mark, however, the Balmer lines show a strong increase in contribution. Also Gil et al. (2000) found that the transition zone between the decreasing and increasing contribution occurred around 20% occultation. For increasing occultation of the Moon in front of the Sun beyond the 30%, the irradiance spectrum is significantly influenced by the increasing contribution of radiation from the chromosphere. Figure 2.10 shows the differential optical depths measured by Adams et al. (2010) during a solar eclipse where the maximum occultation was 96%. The differential optical depth is a measure of the residual divided by the average reflectance within the fit window used in DOAS. The measurements made during the eclipse show large deviations from the non-eclipse measurements.

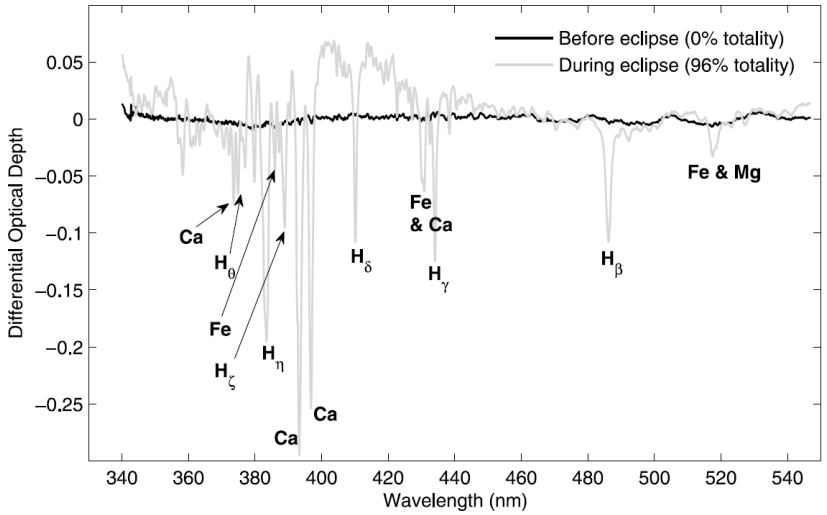


**Figure 2.10:** Measured differential optical depths before the solar eclipse (in black) and during the solar eclipse at 96% occultation (in grey) (Adams et al., 2010).

In order to explain the reason for the changing irradiance spectrum during a solar eclipse, we illustrate the contribution of the photosphere and chromosphere to the irradiance signal during a solar eclipse in Figure 2.11. Here the chromosphere is only presented as the circumference of the Sun because the assumption is made that the photosphere dominates the radiance received directly. Starting with the non-eclipse representation, we see that both the photosphere and the chromosphere contribute 100% to the outgoing light. Following the start of the eclipse, first, the chromosphere is blocked relatively more than the photosphere as only the outer edge of the solar disk is covered by the moon. As a consequence, the photosphere is for 95% visible and the chromosphere for 90%. Therefore the contribution of the Balmer lines in the spectrum decreases. As the solar eclipse evolves further, the turning point is met where both the photosphere and the chromosphere are visible for 80%. The relative contribution seen in the wavelength spectrum is thus similar to a non-eclipse configuration. Subsequently, the contribution of the photosphere will decrease faster than the contribution of the chromosphere. Consequently, the difference in contribution is expected to be visible in the wavelength spectrum due to the Balmer lines growing in size. Since $NO_2$ is retrieved from the high-spectral resolution structure of the measured spectra, those Balmer line signatures could potentially introduce biases in the $NO_2$ retrieval if not accounted for.

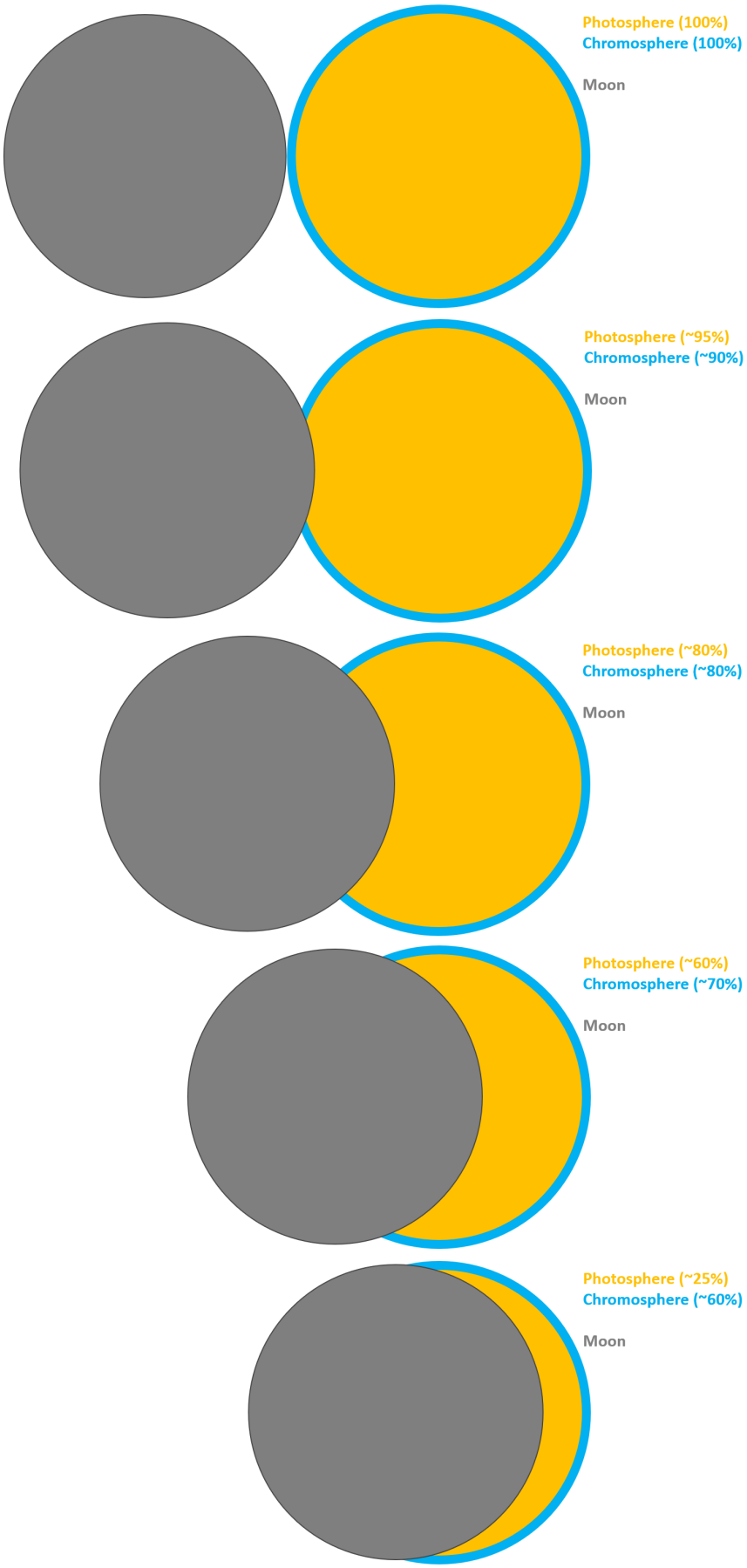


**Figure 2.11:** An example of a solar eclipse and the resulting contribution of the photosphere and the chromosphere to the irradiance received on Earth.

### 2.4.3. Solar eclipse influence on $NO_2$ concentrations

Solar eclipses could have an effect on the actual $NO_2$ concentration in the Earth's atmosphere. In the lunar shadow, the conversion rate from $NO_2$ to NO in Equation 2.1 is expected to be smaller due to the decrease of available sunlight. Moreover, the NO gas continues to be transformed to $NO_2$, as $O_3$ is still present. The expectation is that as soon as the eclipse starts, the corresponding changes in $NO_2$ concentration should be seen. According to Gil et al. (2000), the increase occurs linearly with the reduction of available sunlight. Using ground-based observations, Adams et al. (2010) indeed measured a maximum of 84% local increase of $NO_2$ slant column density during the solar eclipse of the 1st of August 2008. The relation between the measured ratio of $NO_2$ concentration with respect to the control day and the reduction in available sunlight caused by the solar eclipse, as found by Adams et al. (2010) is shown in Figure 2.12.

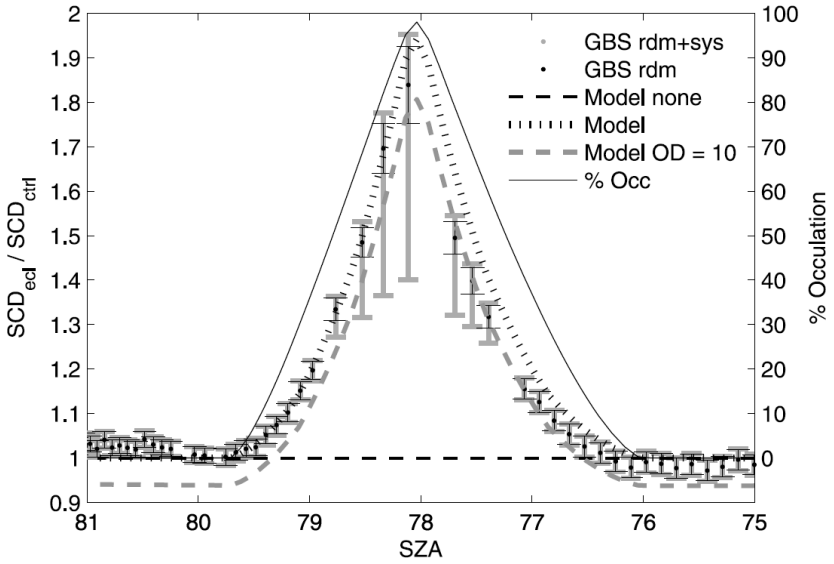


**Figure 2.12:** Measured and modelled values for the ratio between $NO_2$ slant column density concentrations during a solar eclipse and the control day are plotted against the solar zenith angle of the ground-based observations. Additionally, the percentage of occultation (in our research introduced as obscuration fraction) of the solar eclipse is included on the right y-axis (Adams et al., 2010).

The measurements of the $NO_2$ SCD normalized by the control day concentration increase and decrease similarly as the occultation increases and decreases. Additionally, the modelled $NO_2$ SCD ratios agree well with the measured values until the maximum occultation is reached. As the occultation decreases, the modelled values appear systematically higher than the measurements (Adams et al., 2010). Overall, good agreement is seen between the measured and modelled values with the degree of occultation during the solar eclipse.

As an eclipse happens, different parts of the world are experiencing different magnitudes of occultation. An eclipse happening exactly in the orbit where TROPOMI is taking its measurements creates an excellent opportunity to analyze the various effects it has on the $NO_2$ concentration on a global scale.

# 3

# Problem description

Here, the problem of measuring $NO_2$ concentrations during a solar eclipse from space using TROPOMI will be shown and elaborated. Two solar eclipses are considered here and will be used in further analysis as well. In Section 3.1 the original measurements regarding concentrations, uncertainty, errors and processing specifics of the solar eclipse of 10 June 2021 will be discussed. In Section 3.2 the similar elements but then for the solar eclipse on 25 October 2022 will be addressed.

## 3.1. Solar eclipse on 10 June 2021

### 3.1.1. Eclipse specifics

On 10 June 2021, a solar eclipse occurred above Greenland, Europe and Russia. The eclipse started in the west and followed along the orange area and blue lines to the east as depicted in Figure 3.1. The darkest shadow occurred at the point of the greatest eclipse in the north of Greenland at 80° N and 66° W. The maximum obscuration fraction achieved at this location is 0.89 (Espenak, 2016). The complete eclipse lasted 4 h and 59 min from P1 to P4 as seen in Figure 3.1, which represent the beginning and end of the partial eclipse, respectively.

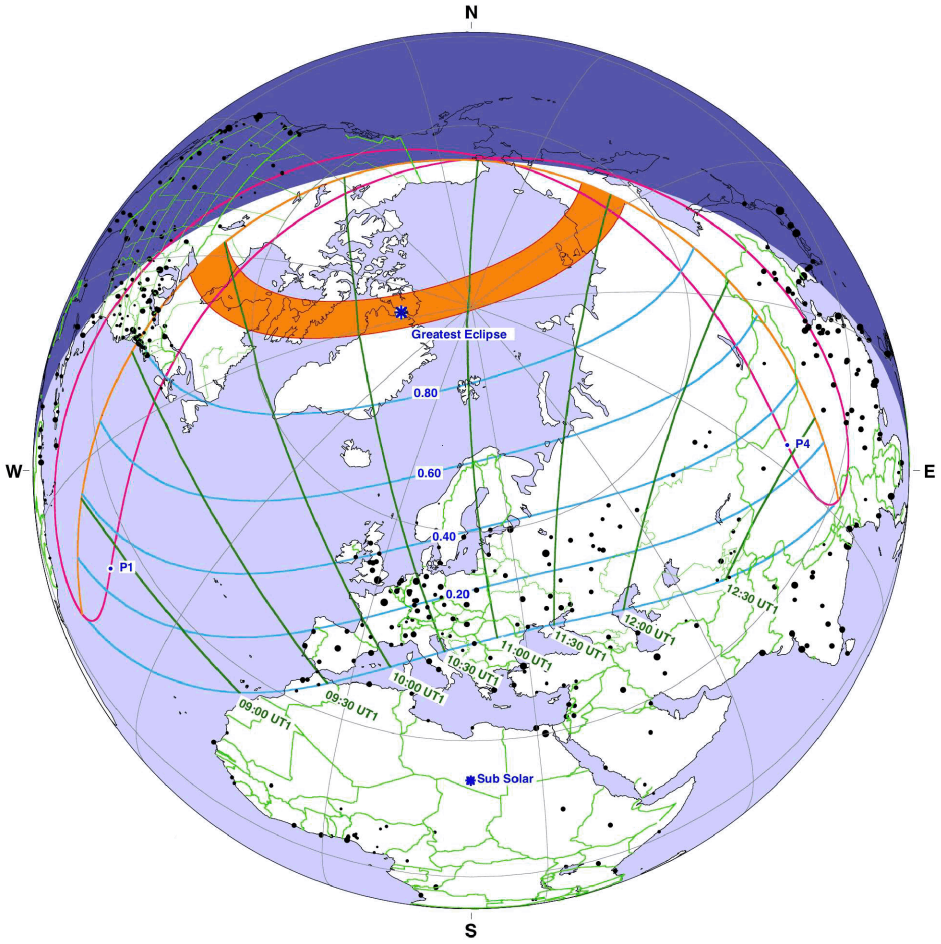


**Figure 3.1:** Eclipse visibility map of the eclipse on 10 June 2021. Green (vertical) lines indicate the progression in time during the solar eclipse. The blue (horizontal) lines indicate the intensity of the shadow through the obscuration fraction with respect to the time notation (Espenak, 2016).

### 3.1.2. $NO_2$ retrieval

The path of TROPOMI orbit 18955 coincided with the path of the solar eclipse and therefore measurements were taken during the solar eclipse. As TROPOMI takes its measurements during mid-day around 13.30 h local time, the green line in Figure 3.1 at 11:30 UT1 time indicates the approximate obscuration experienced during the measurements. The resulting $NO_2$ retrieved is shown in Figure 3.2.

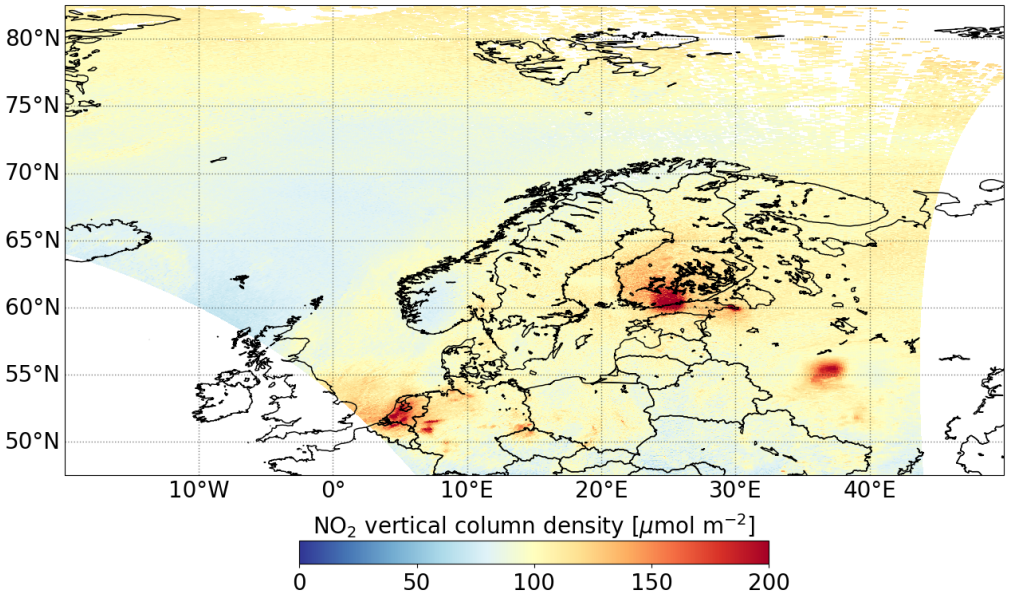


**Figure 3.2:** $NO_2$ vertical column density as originally measured and retrieved by TROPOMI on 10 June 2021 during TROPOMI orbit 18955.

Evident from the $NO_2$ concentrations are the elevated values which are seen to the north of 75° N latitude. Above the Norwegian Sea, a big area of blue pixels is seen where the concentrations are low, which is expected for regions with no influences of emissions. This would be similarly expected for the regions more north towards the North Pole. However, similar concentrations of $NO_2$ as the mean above land concentrations are found. The shape of these increased $NO_2$ concentrations subsequently coincides with the shape of the shadow cast on the Earth's surface due to the solar eclipse. The hypothesis of increased $NO_2$ concentrations during the duration of a solar eclipse could possibly be answered and proven through this observation. Nonetheless, this is not necessarily the case as proof of disturbed $NO_2$ is presented along the increased $NO_2$ values. Within the region of 70° N - 82.5° N and 20° E - 50° E, a significant amount of missing pixels is present, creating the suspicion of an unreliable and incorrect retrieval of the $NO_2$ vertical column density. The next section will therefore show the uncertainty related to the retrieved pixels, to examine whether the retrieval is indeed unreliable.

### 3.1.3. $NO_2$ uncertainty

The $NO_2$ slant column uncertainty is analysed to determine the reliability of the $NO_2$ vertical column densities as presented in Subsection 3.1.2.

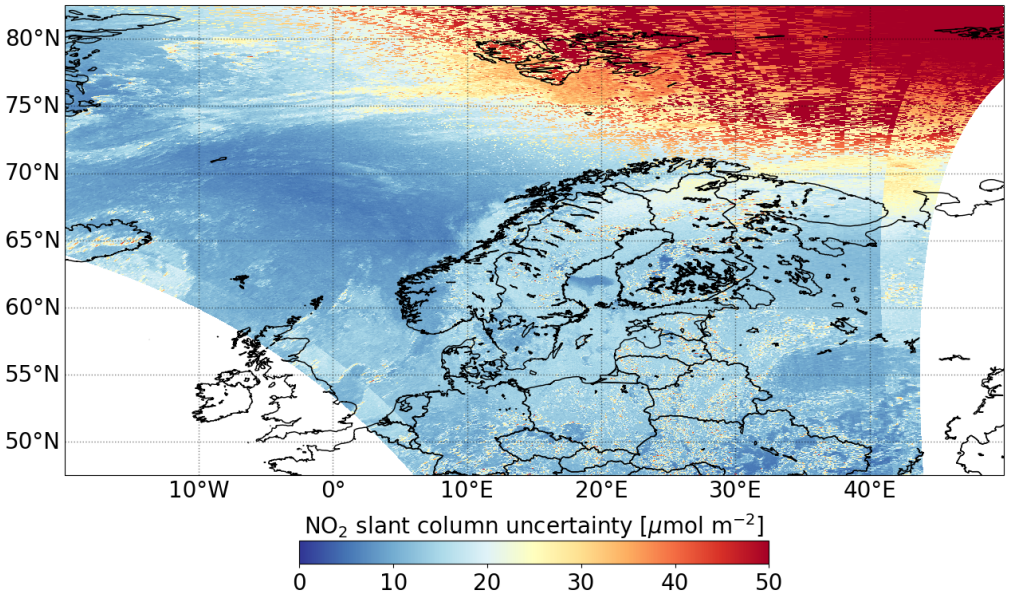


**Figure 3.3:** $NO_2$ slant column uncertainty as originally measured and retrieved by TROPOMI on 10 June 2021 during TROPOMI orbit 18955.

A significant increase in the $NO_2$ slant column uncertainty is seen in the north in Figure 3.3. This is in a similar region where higher values of $NO_2$ were seen in Figure 3.2, in addition to the completely missing pixels. The $NO_2$ slant column uncertainties increase towards a considerable 50 $\mu$mol m$^{-2}$ where the pixels take on a red colour. Again, the shape of the shadow caused by the solar eclipse is well visible. Interestingly, a relatively big region showing orange pixels around 77° N and 20° E stands out between dominant red-coloured pixels. Nonetheless, these orange pixels exceeded the quality threshold of 33 $\mu$mol m$^{-2}$ and are therefore assigned as bad quality. An in-depth analysis of the origin of these high uncertainties can be accomplished by determining the related warnings and errors for the pixels.

### 3.1.4. Processing quality flag

The processing quality flag attribute accompanied by the TROPOMI processing results shows the flags indicating conditions that affect the quality of the retrieval. The two major warnings and errors in the processing quality flag attribute for TROPOMI orbit 18955 are shown in Figure 3.4, which are specifically related to the $NO_2$ retrieval algorithm.

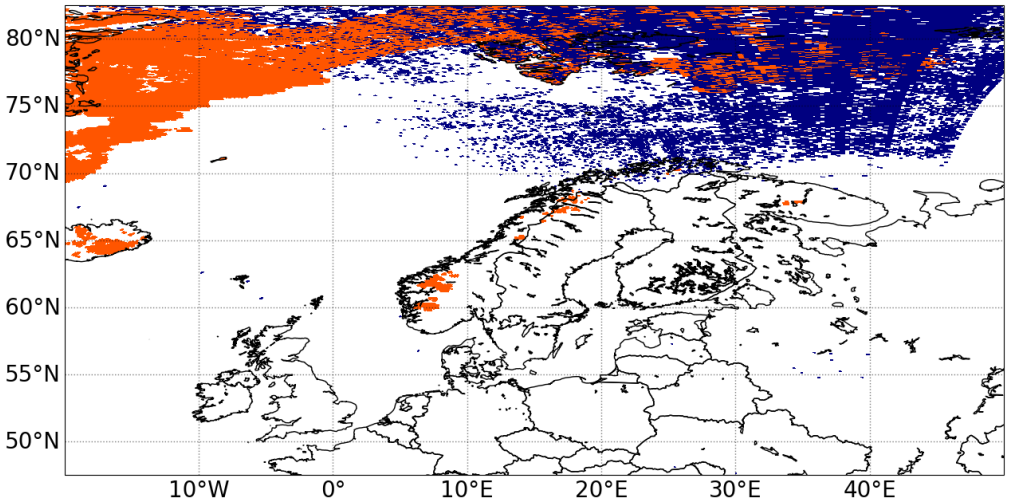


**Figure 3.4:** Pixels containing a warning or error in the processing quality flag attribute in the TROPOMI orbit 18955. The snow & ice warning (in orange) and the maximum number of outliers exceeded error (in blue) are shown.

The pixels shown in orange in Figure 3.4 are flagged with the snow & ice warning, which is produced by the cloud support product (Eskes et al., 2022). The pixels shown in blue in Figure 3.4 are flagged with the maximum number of outliers exceeded error, which is an outcome of the DOAS fitting process. Here, the number of outliers detected in the DOAS fit exceeds a maximum set for healthy spectra (Eskes et al., 2022). Overall, the difference between a warning and an error is seen in the fact that for a warning the pixel is not necessarily bad enough not to be processed. Still, the user is warned that the retrieval might have been negatively influenced. In contrast, an error indicates that the retrieval for the pixel was aborted due to for instance, bad quality of the input or missing input for the retrieval.

The comparison between Figure 3.3 and Figure 3.4 shows that the uncertainty in $NO_2$ concentrations is mainly caused by the error related to the number of outliers in the DOAS fit. This is the result of the spike removal, as introduced in Subsection 2.2.2, where the pixel can be ignored if the remaining spectrum still consists of 10 or more outliers during the second attempt of running the DOAS fit. Consequently, this error likewise caused the high amount of missing pixels as seen in Figure 3.2. Interestingly, the relatively big region showing orange pixels around 77° N and 20° E in Figure 3.3, show no warnings or errors in Figure 3.4 while being surrounded by a considerable amount of pixels containing errors related to the outliers within DOAS. This indicates that for pixels that did not experience processing difficulties, the uncertainty is still significantly higher than for pixels that did not experience solar eclipse effects. Following this error analysis, the origin of the responsible error will be highlighted to create an understanding of the physics related to the principle problem of the $NO_2$ retrieval influenced by a solar eclipse.

### 3.1.5. High-spectral-resolution features

The residual spectrum (see Subsection 2.2.2) retrieved after the measurements taken by TROPOMI can highlight specific influences on the measurements which were difficult to fit with the modelled reflectance ($R_{\text{mod}}$). A solar eclipse is one of these possible influences where the measurements can be disturbed in the spectral domain and the result is shown in Figure 3.5. For this analysis, the spike removal is turned off as a feature in the DOAS fitting process, to visualise the effect of the occurring physics in the form of high-spectral-resolution features.

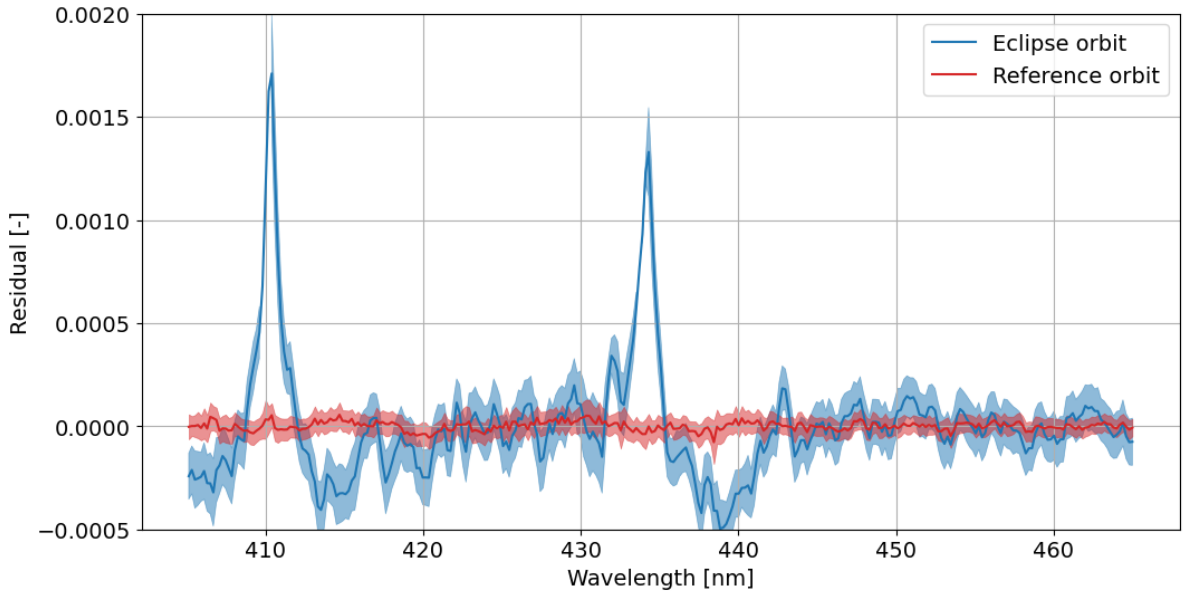


**Figure 3.5:** Residual spectrum of a pixel from an eclipse orbit experiencing a high obscuration fraction (in blue) and the residual spectrum of a pixel from a reference orbit without an eclipse (in red).

The high-spectral-resolution features are visible in Figure 3.5 at the wavelengths where the spectrum, originating from a pixel measured during the eclipse (in blue), shows significant increases in the residual. Compared to the reference spectrum (in red), which was retrieved from a pixel not experiencing a solar eclipse during a different orbit, the increase in residual seen in the spectrum taken during a solar eclipse

can be signified to indicate an even more striking result. High residuals like those shown here are an indication of an inaccurate retrieval. The modelled reflectance is found to be unable to produce a proper replica of the measured reflectance. The fitting parameters within the DOAS process are inadequate to create a representative modelled reflectance similar to the measured reflectance influenced by a solar eclipse.

## 3.2. Solar eclipse on 25 October 2022

The solar eclipse on 25 October 2022 occurred over Europe, the Middle East and Russia. The duration from where the solar eclipse starts to the end, from P1 to P4 in Figure 3.6, was 4 hours and 2 minutes. The moment of the Greatest Eclipse occurred above Russia, where the maximum obscuration fraction was 0.82 (Espenak, 2016).


**Figure 3.6:** Eclipse visibility map of the eclipse on 25 October 2022. Green (vertical) lines indicate the progression in time during the solar eclipse. The blue (horizontal) lines indicate the intensity of the shadow through the obscuration fraction with respect to the time notation (Espenak, 2016).

As the TROPOMI orbit 26077 flies over, the solar eclipse is caught and the atmospheric measurements during the solar eclipse are taken. The resulting $NO_2$ concentration measurements are shown in Figure 3.7.

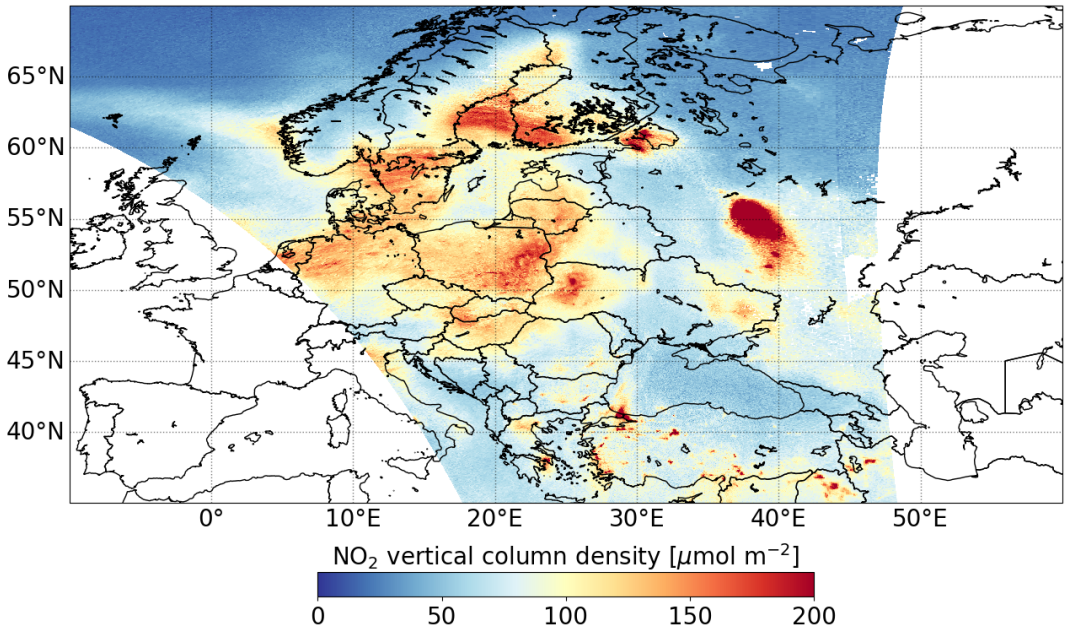


**Figure 3.7:** $NO_2$ vertical column density as originally measured and retrieved by TROPOMI on 25 October 2022 during TROPOMI orbit 26077.

At first hand, the response of the $NO_2$ retrieval to the solar eclipse is not clearly visible. However, the $NO_2$ concentrations in Figure 3.7 show slightly elevated values in a circular pattern east to 35° E between 42.5° N and 57.5° N. In addition, a region of very high concentrations is seen originating from Moscow. In the east of the orbit at the 50° N latitude, an area is presented where pixels are missing, which also represents the centre of the circular pattern described at the beginning of this paragraph. This coincides with the increasing obscuration fraction of the solar eclipse towards the east. Again, these factors point in the direction of an unreliable and incorrect retrieval of the $NO_2$ vertical column density. The next figure therefore shows the slant column uncertainty of the measurements taken during TROPOMI orbit 26077.

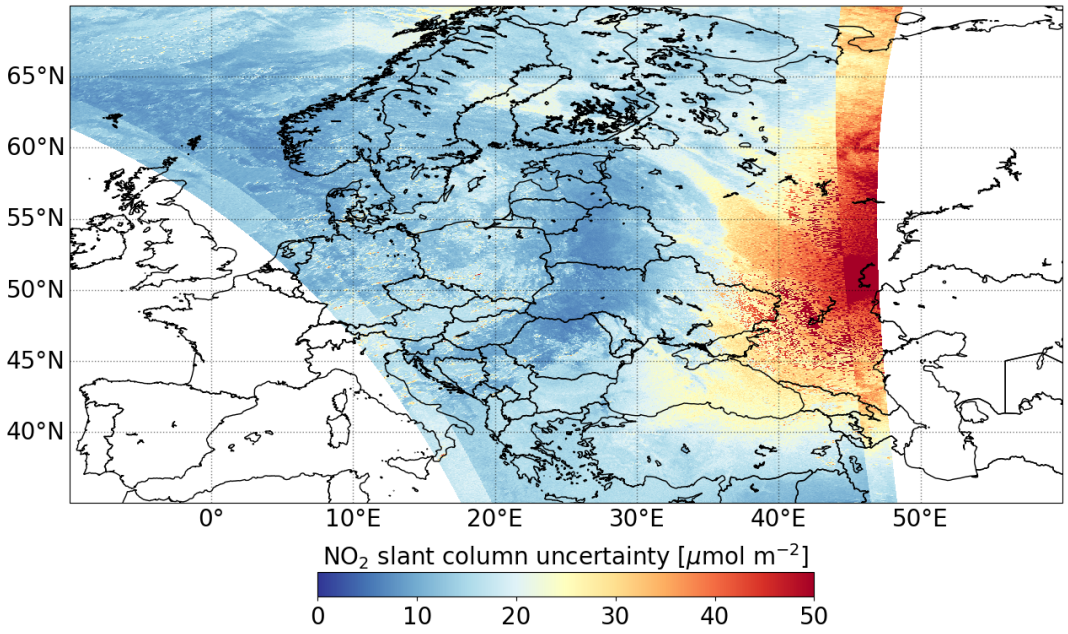


**Figure 3.8:** $NO_2$ slant column uncertainty as originally measured and retrieved by TROPOMI on 25 October 2022 during TROPOMI orbit 26077.

Evident from the $NO_2$ slant column uncertainty in Figure 3.8 is the high uncertainty over Russia in the east of the orbit. In this orbit, again significant uncertainties leading up to 50 $\mu$mol m$^{-2}$ are presented, where the majority also crossed the quality threshold of 33 $\mu$mol m$^{-2}$. The $\simeq$ 20 ground pixel rows in the east of the orbit show a sharp increase in uncertainty as this is related to the binning procedure of the measurements taken by TROPOMI. Here, the pixels are based on only one detector measurement of the instrument, while for the majority of the ground pixels, two detector measurements can be used. To get a better understanding of the cause for the overall high uncertainties, the warnings and errors relating to the processing are shown in Figure 3.9.

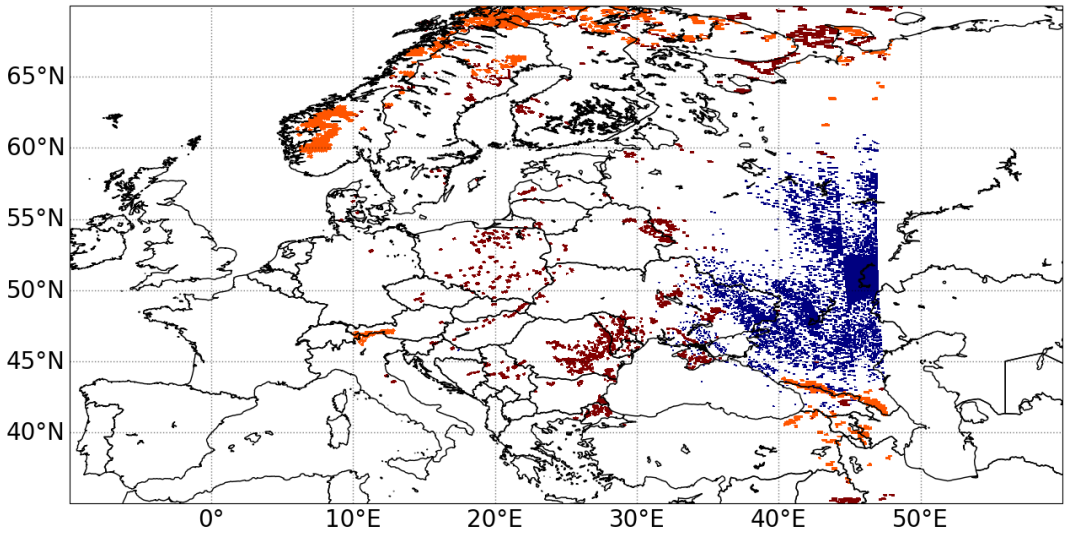


**Figure 3.9:** Pixels containing a warning or error in the processing quality flag attribute in the TROPOMI orbit 26077. The snow & ice warning (in orange), the maximum number of outliers exceeded error (in blue) and the pixel level of input data error (in brown) are shown.

The warnings and errors that show a considerably high contribution for TROPOMI orbit 26077 are shown in Figure 3.9. Similar to the orbit shown in Subsection 3.1.4, the orange pixels present the snow & ice warning and the blue pixels show the maximum number of outliers exceeded error. In addition, a significant amount of flags were seen in this orbit containing the pixel level of input data error, which is presented in brown in Figure 3.9. This error is related to missing part(s) for the auxiliary input data (Eskes et al., 2022). Overall, this can be related to for example cloud input data, but for this case containing a solar eclipse, there does not seem to be a relationship. The pixels containing this error do not show any feedback in the uncertainty values.

Similar to the errors seen for the solar eclipse on 10 June 2021, the influence of the solar eclipse on 25 October 2022 seems to be the cause of the high uncertainty as seen in Figure 3.8. A distinct correlation can be seen between the pixels containing the maximum number of outliers exceeded error in Figure 3.9 and the high uncertainty as shown in Figure 3.8. The high number of spectral outliers in the DOAS fitting algorithm causes these pixels to be deleted. In addition, the residual spectrum of orbit 26077 shows similar behaviour for the ground pixels affected by the solar eclipse as shown in Figure 3.5. Consequently, we can say that the retrieval of $NO_2$ is unreliable and disrupted by the influence of the solar eclipse.

# 4

# Methodology

In this chapter, the methodology of correcting the TROPOMI measurements for solar eclipse-related biases and modelling of the solar eclipse influences on $NO_2$ in the atmosphere will be discussed. First, the obscuration fraction computation will be explained including the solar limb darkening (Section 4.1). Secondly, the adjustment of the TROPOMI $NO_2$ retrieval will be highlighted (Section 4.2). A validation of the adjustment of the $NO_2$ retrieval will be shown additionally (Section 4.3). Finally, the modelling of the expected $NO_2$ concentrations during the solar eclipse will be discussed (Section 4.4).

## 4.1. Obscuration fraction

To be able to apply calculations concerning the solar eclipse, it will first be important to know the actual straightforward effect of the solar eclipse, which is the darkness of the shadow as described by the obscuration fraction $f_{\mathsf{o}}$. The obscuration fraction can be computed for every pixel as measured by TROPOMI, thus giving a measure of obscuration. Note that for every pixel the obscuration is calculated at the time the specific pixel was measured by TROPOMI. This way, the most accurate representation of the dynamic event of a solar eclipse is presented as a single moment in time and is in direct correspondence with the affected $NO_2$ concentration as measured in the atmosphere. In the computation, the sunlight's darkening effect towards the Sun's edge needs to be accounted for (see Subsection 2.3.3). These wavelength-dependent darkening effects are incorporated by the solar limb darkening function. The complete computation used in this research, as also used and described by Koepke et al. (2001), can be found in the paper by Trees et al. (2021).

The obscuration fraction $f_{\mathsf{o}}$ during a solar eclipse, as seen in Trees et al. (2021) (see Eq. 9), can be computed as follows:

$$f_{\mathsf{o}}(X, r_{\mathsf{m}}, \lambda) = \frac{\int_0^1 \frac{\alpha(r, X, r_{\mathsf{m}})}{\pi} \Gamma(\lambda, r) \cdot r \mathsf{d}r}{\int_0^1 \Gamma(\lambda, r) \cdot r \mathsf{d}r} \tag{4.1}$$

Here, the solar limb darkening function $\Gamma$ is based on the definition of Koepke et al. (2001):

$$\Gamma(\lambda, r) = \frac{I_0(\lambda, r)}{I_0(\lambda, r = 0)} \tag{4.2}$$

The solar limb darkening function describes the level of irradiance at a radius of $r$ away from the solar disk centre ($I_0(\lambda, r)$), normalized by the irradiance originating from the centre of the solar disk ($I_0(\lambda, r = 0)$) (Koepke et al., 2001). This function is wavelength-dependent as irradiance from different radii is emitted at different wavelengths (see Subsection 2.3.1). For the most accurate computation of the solar limb darkening, the approach of Ockenfuß et al. (2020) is implemented in the calculations as this showed good agreement with the measurements from Bernhard and Petkov (2019) made during a solar eclipse (Trees et al., 2021). Here, the wavelength-dependent limb darkening coefficients of Pierce and Slaughter (1977) can be used to compute the received light per wavelength concerning the sunlight during a solar eclipse and the final values for $\Gamma$ are included. The expression for the function

$\Gamma$ can be found in detail in the paper by Trees et al. (2021) (see Eq. 5). The solar limb darkening effect is visualised in Figure 4.1, where $\Gamma$ is plotted against $r$ the radius of the Sun.

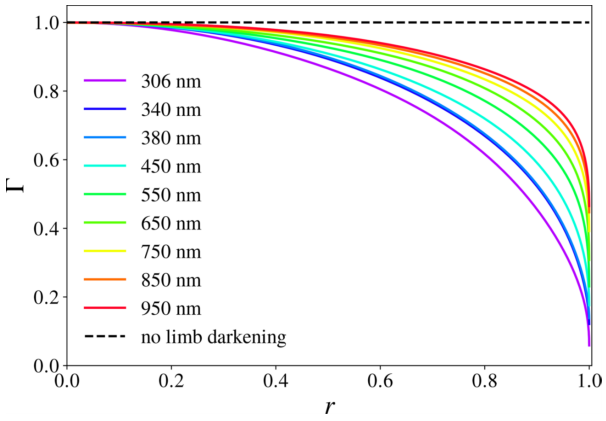


**Figure 4.1:** Limb darkening function $\Gamma$ for wavelengths ranging from 306 to 950 nm, where $r$ describes the radius distance away from the solar disk. The dashed line is the result without solar limb darkening taken into account ($\Gamma = 1$) (Trees et al., 2021).

Furthermore, the angle $\alpha$ in Equation 4.1 describes the degree of occultation of the lunar disk in front of the solar disc. This is based on the geometry as shown in Figure 4.2. The mathematical expression of $\alpha$ is based on $r$, $X$ and $r_\mathrm{m}$, which are the radius of a circular solar ring, the distance between the centres of the Moon and the Sun and the radius of the Moon, respectively. The expression of $\alpha$ can be found in the paper by Trees et al. (2021) (see Eq. 8). Subsequently, the calculation of $X$ and $r_\mathrm{m}$ can be found in Appendix A of Trees et al. (2021). The Besselian elements as used and described there, originate from and are published by NASA (Espenak and Meeus, 2006).

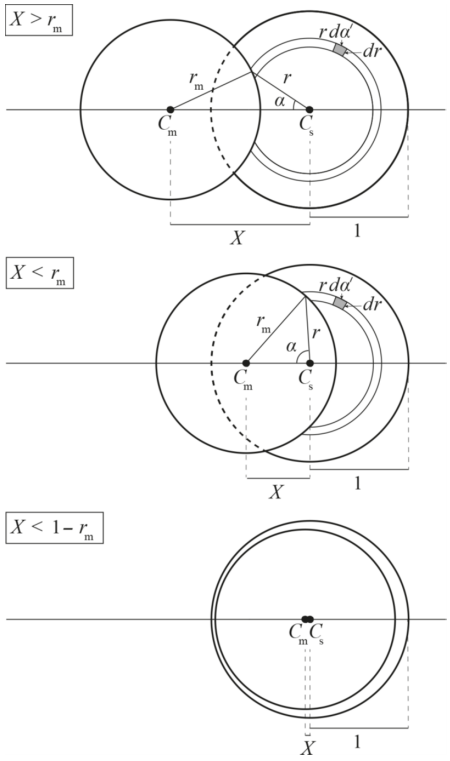


**Figure 4.2:** Sketches of the lunar disk (centred at $C_\mathrm{m}$) occulting the solar disk (centred at $C_\mathrm{s}$) during an annular solar eclipse. Here, $r_\mathrm{m} < 1$, where $r_\mathrm{m}$ is the radius of the lunar disk and the solar disk radius equals 1. $X$ is the distance between $C_\mathrm{m}$ and $C_\mathrm{s}$. For $X < r_\mathrm{m} + 1$, the lunar disk occults the solar disc. The eclipse obscuration fraction $f_\mathrm{o}$ increases with decreasing $X$. The annular phase occurs when $X < 1 - r_\mathrm{m}$ (bottom sketch). Angle $\alpha$ is half the sector angle of the solar disk occulted at distance $r$ by the lunar disc (Trees et al., 2021).

In this computation of the obscuration fraction, the assumption is made that the Moon is a circular disk as it moves in front of the Sun. This assumption is based on the solid composition and the nearly spherical shape of the Moon, with an atmosphere that optically is of irrelevant significance (Trees et al., 2021). The uncertainty related to this assumption will additionally also be considered to be zero, despite the fact the Moon does deviate from a circular disk due to the topography present on the Moon's surface. An analysis on the error propagation of this assumption was made by Trees et al. (2021), where was found that pixels within the shadow of the eclipse and measured by TROPOMI saw absolute differences of 0.00049 for the obscuration fraction. Since this is an insignificant difference, the error of the obscuration fraction $f_o$ can be assumed to be negligible.

## 4.2. Adjustment of the $NO_2$ retrieval

The following subsections will derive the process of adjusting the TROPOMI $NO_2$ retrieval to correct for the solar eclipse. Firstly, the radiance correction will be covered (Subsection 4.2.1), which is followed by the cloud correction and pixel recovery (Subsection 4.2.2). Next, the influence of solar eclipses on the TROPOMI DOAS fitting process is described with the corresponding high-spectral resolution features in the residual spectrum (Subsection 4.2.3). Subsequently, the required fitting window correction is explained (Subsection 4.2.4). The slant column uncertainty before and following the window correction is shown to validate the method (Subsection 4.2.5). Finally, the approach for the conversion from SCD to VCD measurements is addressed (Subsection 4.2.6). In the following schematic, an overview is given of the entire workflow of the adjustment of the $NO_2$ retrieval.

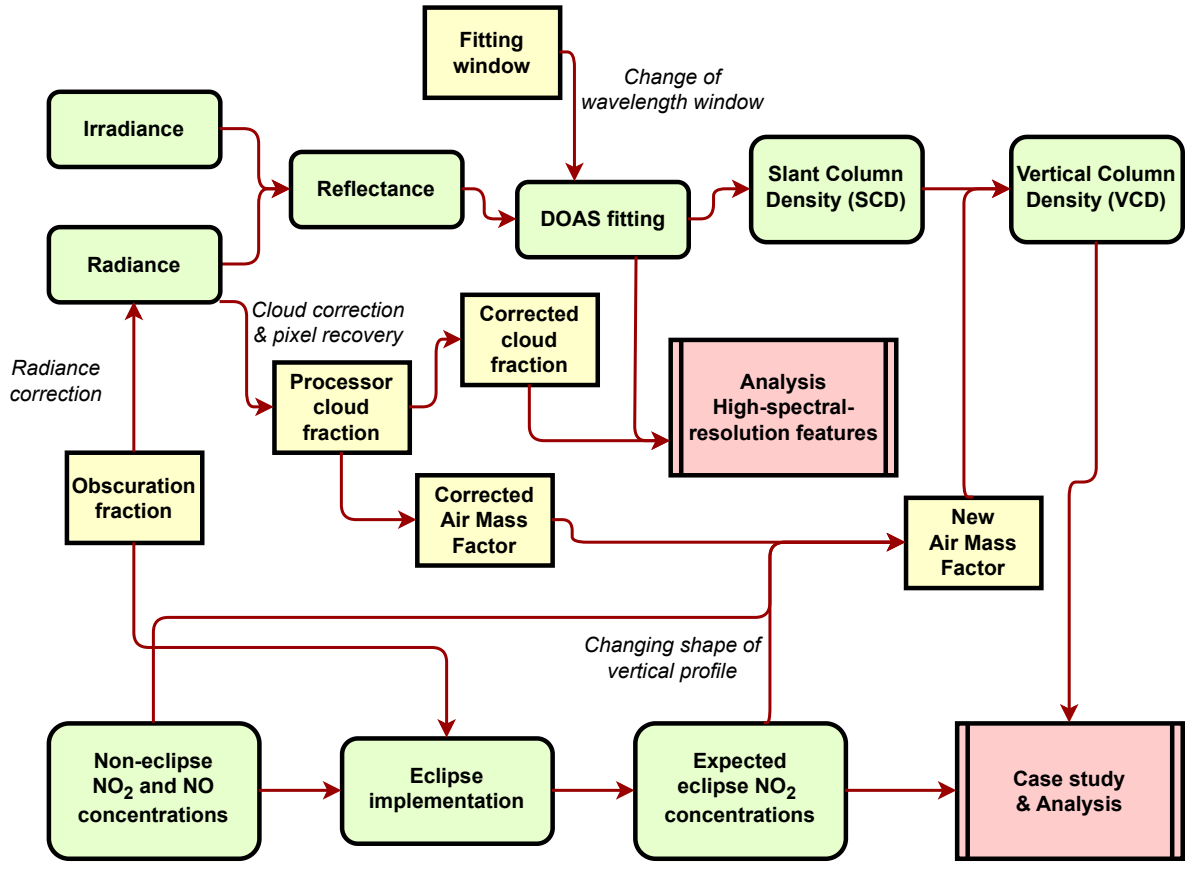


**Figure 4.3:** Schematic of the workflow described for the methodology. The green blocks show the general flow of either the TROPOMI processing (upper chain) or the TM5 processing (lower chain). The yellow blocks show where additional actions are needed for the adaptation to the solar eclipse scenario. The red blocks show the final analysis to be performed.

### 4.2.1. Radiance correction

The ratio between the measured irradiance and radiance is important for the retrieval of $NO_2$, as was discussed in Subsection 2.2.2. The measured irradiance does not change during a solar eclipse, since TROPOMI will always measure the radiation coming directly from the Sun, without any interference from the Earth or Moon. This doesn't hold for the radiance, as it is reflected via the Earth, which is experiencing the effects of the eclipse. This is visualized in Figure 4.4.

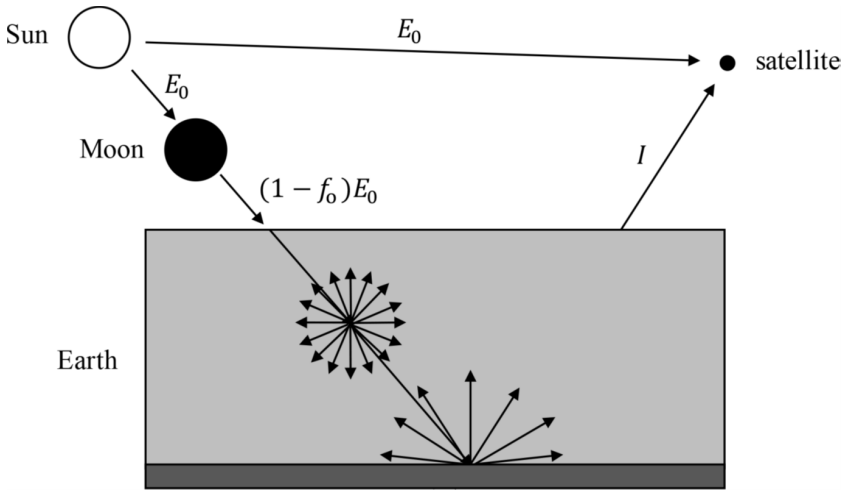


**Figure 4.4:** Schematic of the influence of a solar eclipse on the measured radiance (Trees et al., 2021).

What could already be concluded from Figure 4.4, is that the radiance needs to be corrected by a factor of the obscuration fraction $f_o$, which we compute according to Equation 4.1. For this application of the obscuration fraction, the obscuration fraction is computed for 440 nm as this is the median of the wavelengths in the default TROPOMI $NO_2$ spectral fitting window. Assuming that the light paths in the penumbra of the solar eclipse are unchanged (Trees et al., 2021; Emde and Mayer, 2007), the corrected reflectance for the obscuration in the penumbra can be computed as shown in Equation 4.3 (see also Eq. 2 of Trees et al., 2021).

$$R_{\text{corr}}(\lambda) = \frac{1}{1-f_o} \cdot \frac{\pi I(\lambda)}{\mu_0 E_0(\lambda)} = \frac{\pi I(\lambda)}{\mu_0 (1-f_o) E_0(\lambda)} \tag{4.3}$$

$R_{\text{corr}}$ is the intrinsic reflectance of the atmosphere-surface system and thus can be used to infer properties of the atmosphere inside the penumbra of a solar eclipse. In practice, we correct $I$ in the Level-1 radiance file, as follows:

$$I_{\text{corr}} = \frac{I}{1-f_o} \tag{4.4}$$

which also yields $R_{\text{corr}}$ via Equation 4.3. We use $I_{\text{corr}}$ as Level-1 input for the computation of the reflectance as described in Equation 2.11 (see *Radiance* and *Reflectance* in Figure 4.3).

During the DOAS fitting process, the chi-squared parameter is optimized by computing the best fitting $R_{\text{mod}}$, which was shown in Equation 2.12. As shown in Equation 2.16 and Equation 2.15 the noise of the radiance is of importance as well. Consequently, the radiance noise will also need to be corrected based on the influence of the obscuration factor. In the original Level-1 file, the radiance noise is saved in dB units. As the correction for the eclipse needs to be applied to the power quantity, conversions back and forth from dB are needed. The necessary conversions are shown in Equation 4.5 to Equation 4.7.

$$\Delta I(\lambda_i) = 10^{\Delta I_{\text{dB}}(\lambda_i)/10} \tag{4.5}$$

$$\Delta I_{\text{corrected}}(\lambda_i) = \frac{\Delta I(\lambda_i)}{1-f_o} \tag{4.6}$$

$$\Delta I_{\text{dB,corrected}}(\lambda_i) = 10 \cdot log_{10}(\Delta I_{\text{corrected}}(\lambda_i)) \tag{4.7}$$

### 4.2.2. Cloud correction & pixel recovery

The cloud fraction retrieved by TROPOMI also suffers from the reduced radiance during a solar eclipse. The effective cloud fraction is an input variable for the $NO_2$ retrieval processing chain (see *Processor cloud fraction* in Figure 4.3) and determines the air mass factors for the conversions to vertical column densities. Therefore, the effective cloud fraction should be corrected as well. We corrected the effective cloud fraction by running the FRESCO (Fast Retrieval Scheme for Clouds from the Oxygen A band) algorithm in the C++ processor at the KNMI workstation with the corrected Level-1 radiance (see Equation 4.4). This outputs the effective cloud fraction in the $NO_2$ fitting window together with the new air mass factors (see Appendix C of Van Geffen et al., 2021). The obscuration fraction for this correction was computed at 440 nm, and we turned off the option to delete pixels that have spikes in the residual spectrum (the so-called automatic spike removal). In this process, missing pixels related to missing air mass factors, bad quality and/or spikes in the spectrum were recovered, in addition to the corrected cloud fraction and the air mass factor. This means that a more complete analysis can be made as more pixels are able to be converted from slant column densities to vertical column densities following the DOAS fitting procedure.

### 4.2.3. Analysis of high-spectral-resolution features originating from the Sun

For the assessment of the high-spectral-resolution features in the DOAS residual spectrum originating from a changed solar spectrum during a solar eclipse, cloud-free pixels will be selected from which the residual wavelength spectrum is plotted, including the confidence intervals to be able to distinguish the expected anomalies. The expectation is that as the obscuration fraction increases, anomalies can grow significantly outside the confidence intervals of the reference spectra. As described in Subsection 2.2.2, the spike removal algorithm is designed to remove outliers within the wavelength spectrum. However, the signals that are measured due to the solar eclipse, will act as outliers in the resulting spectrum. Therefore, the spike removal within the DOAS processing is turned off to be able to fully analyse and understand the occurrence and the physics related to the measurements.

In the following figure, an overview is shown where the residual (see Equation 2.14) spectra during a solar eclipse are plotted as the obscuration fraction increases. The reference spectra are also plotted as these show representative spectra for non-eclipse orbits. For both spectra, the mean of the residuals of cloud-free pixels are computed, with their respective confidence intervals.

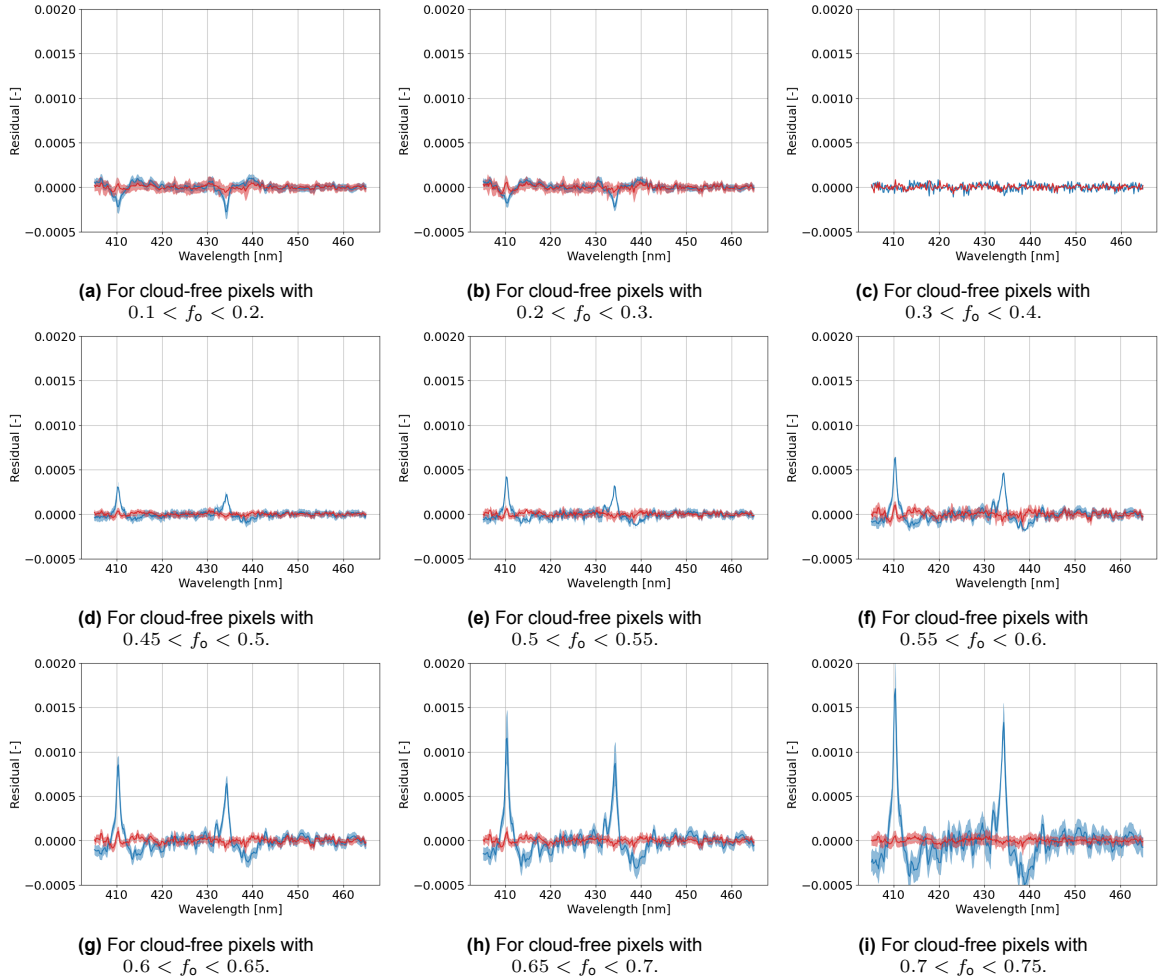


**(a)** For cloud-free pixels with $0.1 < f_o < 0.2$.

**(b)** For cloud-free pixels with $0.2 < f_o < 0.3$.

**(c)** For cloud-free pixels with $0.3 < f_o < 0.4$.

**(d)** For cloud-free pixels with $0.45 < f_o < 0.5$.

**(e)** For cloud-free pixels with $0.5 < f_o < 0.55$.

**(f)** For cloud-free pixels with $0.55 < f_o < 0.6$.

**(g)** For cloud-free pixels with $0.6 < f_o < 0.65$.

**(h)** For cloud-free pixels with $0.65 < f_o < 0.7$.

**(i)** For cloud-free pixels with $0.7 < f_o < 0.75$.

**Figure 4.5:** Residual wavelength spectra per range of obscuration fraction. Eclipse spectra are shown in blue and reference spectra are shown in red.

During the eclipse, the progression of the influence of the Balmer lines is visible. As the obscuration fraction increases, the residual wavelength spectrum also increases around the wavelengths of the Balmer lines within the original fitting window. Consequently, with rising residual values, it can be concluded that the optimal value of the modelled reflectance is not yet close to the measured reflectance. Therefore, the acquired fit results in a $NO_2$ retrieval with decreased quality. Concerning the reference wavelength spectrum shown, the eclipse wavelength spectrum shows large deviations. This amplifies the disagreement between the modelled and measured reflectance of the wavelength spectrum during the solar eclipse. The negative residuals that increase in magnitude as shown in Figure 4.5g, Figure 4.5h and Figure 4.5i are not related to any direct solar eclipse effects. They occur due to the way the DOAS algorithm is executed, this is shown in Appendix B.

Following the statements made by Van Geffen et al. (2021), we do not have to worry about other sources of possible outliers in the spectrum, like the high-energy particles from the South Atlantic Anomaly or bright, cloudy pixels experiencing saturation effects in combination with high SNR values. Firstly, considering the eclipse cases described in Chapter 3, the South Atlantic Anomaly will not be of influence because the eclipse cases used did not occur in the South Atlantic region. Secondly, pixels experiencing saturation effects due to bright clouds and a high SNR mainly occur when clouds are present. Since only cloud-free pixels are analysed, this does not pose a problem. The effect of turning off the spike removal algorithm during a solar eclipse is shown in Figure 4.6, where the increase in residuals is therefore related to the solar eclipse instead of the phenomena as mentioned earlier.

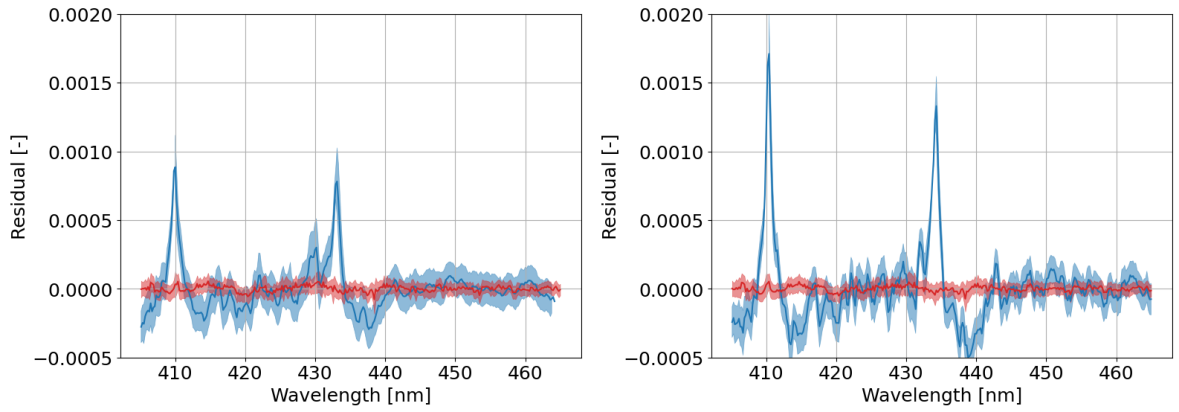


**(a)** Residual spectra with the spike removal algorithm turned on.

**(b)** Residual spectra with the spike removal algorithm turned off.

**Figure 4.6:** Eclipse wavelength spectrum (in blue) and reference wavelength spectrum (in red) for cloud-free pixels with $0.7 < f_o < 0.75$.

### 4.2.4. $NO_2$ fitting window adjustment

Within the standard wavelength range for $NO_2$ of 405 - 465 nm as used by TROPOMI, a few Balmer lines are present and cause the $NO_2$ retrieval to be unreliable. These Balmer lines present themselves at the wavelengths of 410.2 nm and 434.0 nm. Since the influence of these Balmer lines changes drastically during the event of a solar eclipse, as seen in Figure 4.5, another wavelength window could be chosen to be able to retrieve a better residual spectrum and therefore an improved $NO_2$ vertical column density. It was found by Vandaele et al. (1998) that $NO_2$ can naturally be measured in the range of 400 - 500 nm. For TROPOMI, the range of 405 - 465 nm was chosen as this range covers the strongest $NO_2$ absorption lines, this can also be seen in Figure 2.4. The spectrum at wavelengths larger than 465 nm can still be used and so this creates the opportunity to shift the wavelength range, to improve the $NO_2$ retrieval by excluding the wavelengths where the Balmer lines are present. Adams et al. (2010) has tested this on a single slant column measured from the ground surface, where a new range of 438 - 467 nm was chosen. The choice for this range was based on the optimisation of the root mean square residual. For this research, this wavelength range has been implemented and analysed to see whether it shows the same result for large-scale satellite measurements. The implementation of this window on cloud-free pixels for high values of obscuration fraction is already done.

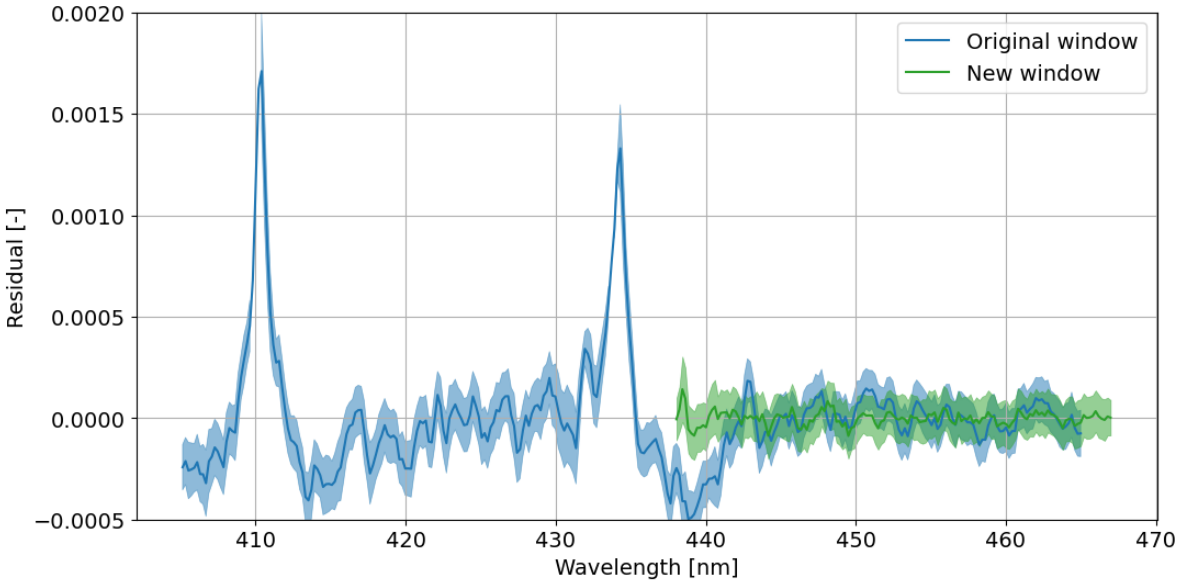


**Figure 4.7:** Spectrum of the original window (in blue) and the new window (in green) during the solar eclipse orbit at $0.7 < f_o < 0.75$.

The difference in magnitude of the residuals between the original window and the new window during a solar eclipse is clearly visible in Figure 4.7. Overall, the residual shows a good response to the solar eclipse and no disturbances due to the Balmer lines are present for the wavelength spectrum of the new window. This results in an overall low value for the residuals, stating a good agreement between the measured and modelled reflectance. Additionally, the residual spectrum of the new retrieval window is compared to a representative non-eclipse residual spectrum. The results shown in Figure 4.8 include the wavelength spectrum during an eclipse orbit using the new window, which is compared to the wavelength spectrum during a non-eclipse orbit using the original window.

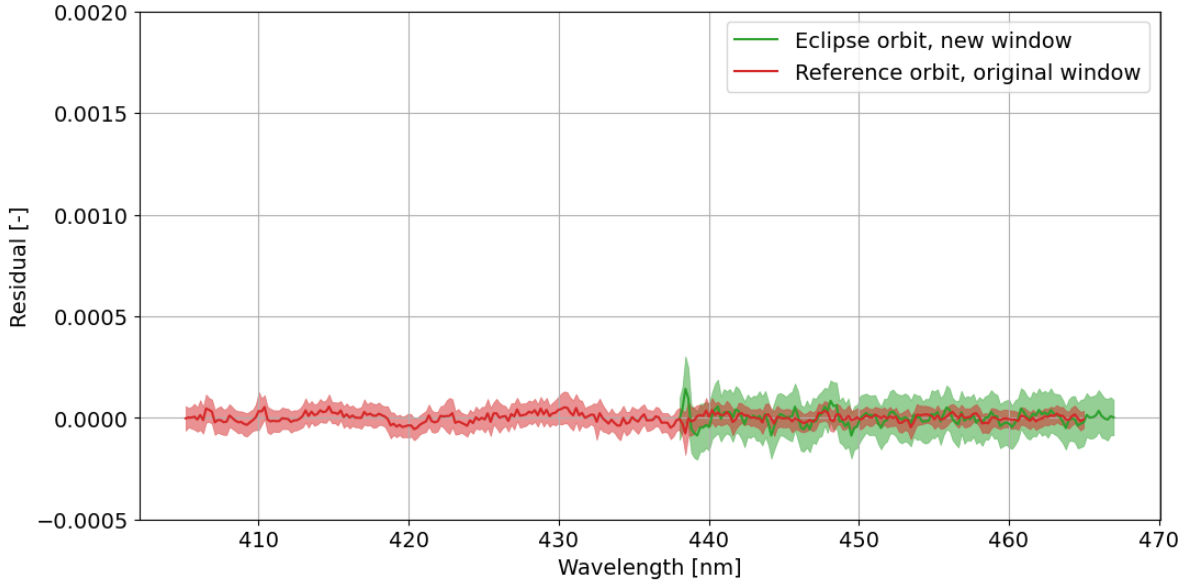


**Figure 4.8:** Spectrum of the original window of the reference orbit (in red) and the new window (in green) during the solar eclipse orbit at $0.7 < f_o < 0.75$.

It is worth noting that the effects of the solar eclipse are still visible in Figure 4.8. The standard deviation of the wavelength spectrum of the new window is still significantly higher when compared to the standard deviation of the reference wavelength spectrum. This is most certainly still a remaining effect of the solar eclipse, as the light experienced during a solar eclipse inherently differs from the non-eclipse situation. Nonetheless, the Balmer lines at wavelengths of 410 nm and 434 are not included in the retrieval and consequently, resulting in their effects on the wavelength spectrum staying undetected. The new range of 438 - 467 nm can therefore be applied to the DOAS fitting for all pixels in the orbit containing the solar eclipse. This will result in new slant column densities, slant column uncertainties and RMS values to be used in the further processing and analysis of the vertical column densities.

### 4.2.5. Slant column uncertainty

Overall, without the $NO_2$ fitting window adjustment described in Subsection 4.2.4 the vertical column density and uncertainty values will not show correct values during a solar eclipse. Considering the uncertainty values, the slant column uncertainties are evaluated here as they are closely related to the measurements and do not include systematic and random errors related to the air mass factor. Contrarily, systematic and random errors are incorporated when looking at the vertical column uncertainties (Van Geffen et al., 2021). Errors related to the slant column are induced by random errors as noise but also include the errors of the physical model and reference spectra chosen for the computation, as explained by Van Geffen et al. (2021). The latter will increase its contribution to the measurements made during a solar eclipse. In addition, quality criteria are applied to the slant column uncertainty, where a value higher than 33 $\mu$mol m$^{-2}$ receives the bad quality flag. Thus, the slant column uncertainty is a good measure to evaluate the improvements of the fit after the window correction.

With the applied window adjustment, improved slant column uncertainties are already seen when compared to the outcomes of the original retrieval. Figure 4.9 and Figure 4.10 show the slant column

uncertainties of the original- and new retrieval of the TROPOMI orbit 26077, respectively.

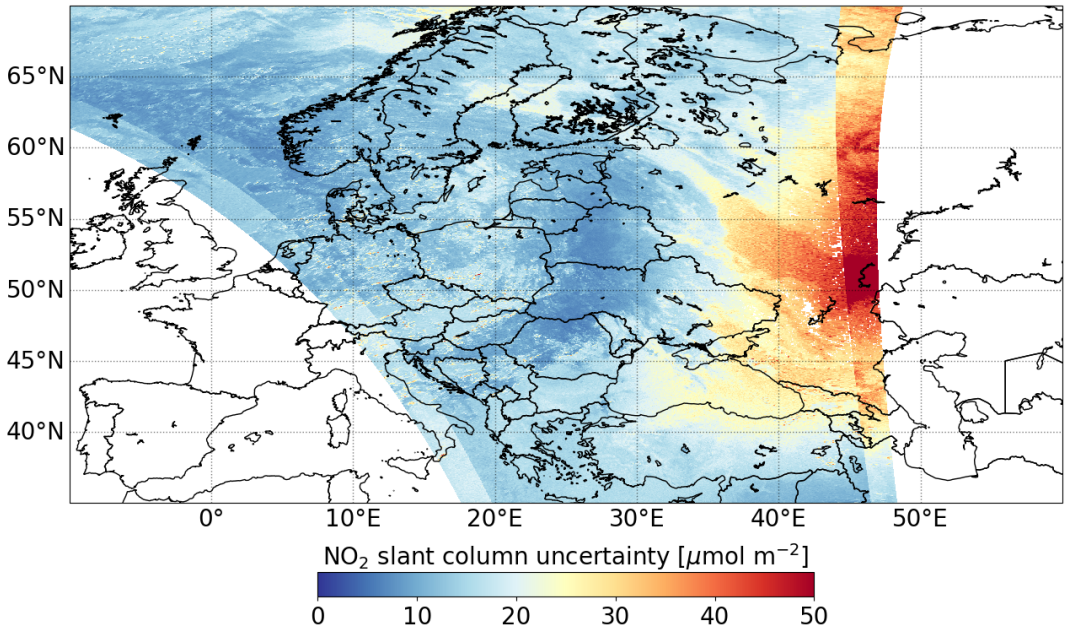


**Figure 4.9:** Slant column uncertainty from the original $NO_2$ retrieval of TROPOMI orbit 26077.

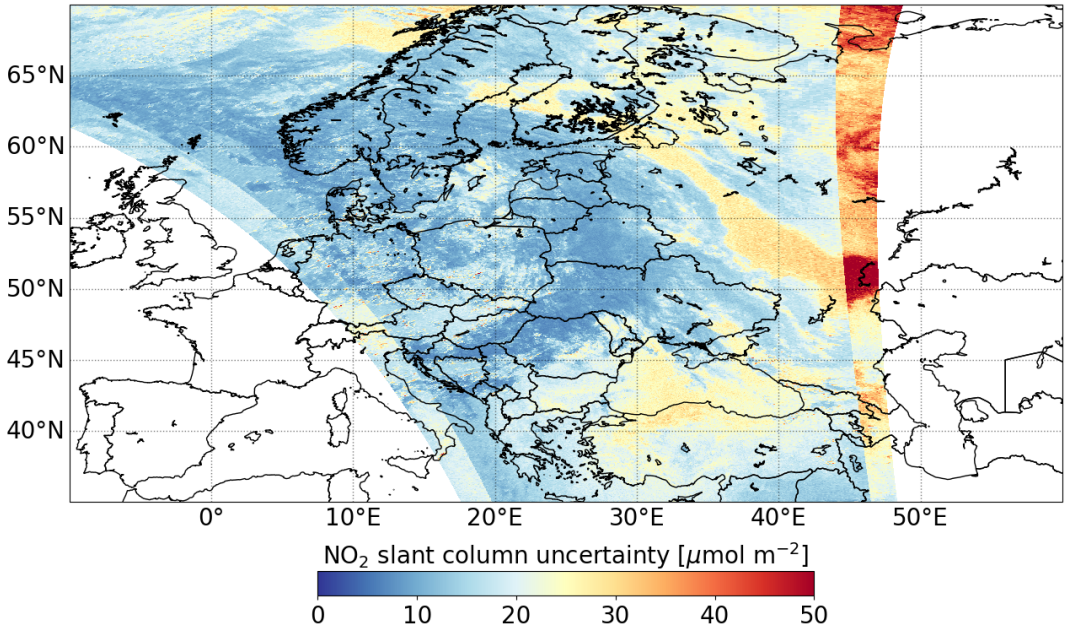


**Figure 4.10:** Slant column uncertainty from the adjusted $NO_2$ retrieval of TROPOMI orbit 26077.

When considering the regions with high obscuration fraction around 51° N and 42 ° E, a change from values above 40 $\mu$mol m$^{-2}$ to around and below 30 $\mu$mol m$^{-2}$ is detected. The decrease in uncertainty is of crucial importance as the threshold of 33 $\mu$mol m$^{-2}$ is now mostly met. As uncertainty values do not cross this threshold after the appliance of the adjustment to the retrieval, significantly fewer pixels are considered to be of bad quality.

The binning procedure as described by Van Geffen et al. (2020) can clearly be seen in both Figure 4.9 and Figure 4.10. In principle, each TROPOMI ground pixel is calculated with the use of two detector

pixels. This is done to keep the across-track ground pixel width more or less constant (Van Geffen et al., 2020). However, only one detector pixel is used in the processing for the first 22- and the last 20 ground pixel rows. As a consequence, using one instead of two detector measurements greatly influences the uncertainty which is seen in Figure 4.9 and Figure 4.10. Nevertheless, an overall improvement in the uncertainty of the slant column densities is evident for the TROPOMI orbit experiencing solar eclipse effects.

Furthermore, the root-mean-square (RMS) error is another way of judging whether the DOAS fit has improved. This is a good addition to the uncertainty analysis, as the RMS only focuses on the goodness of the fit and is not involved in the estimation of the absolute value. In addition, the calculated reflectance noise (see Equation 2.15) is not taken into account as a separate variable within the RMS calculation. This is beneficial as the calculated reflectance noise is also disturbed during a solar eclipse and would induce extra uncertainties in the analysis. Additionally, the root-mean-square error computes the mean of the number of wavelengths, which results in a statistic without a bias due to the two different lengths of wavelength windows. In the end, a certain amount of uncertainty of the SCD and VCD values will always stay, as the conditions of a solar eclipse are inherently different than what TROPOMI was designed for, namely conditions with enough sunlight. This is another reason to consider the RMS value of a pixel to evaluate the improvements. The computation of the RMS as described by Van Geffen et al. (2021) can be seen in Equation 4.8.

$$R_{\text{RMS}} = \sqrt{\frac{1}{n_\lambda} \sum_{i=1}^{n_\lambda} \left(R_{\text{meas}}(\lambda_i) - R_{\text{mod}}(\lambda_i)\right)^2} \tag{4.8}$$

A concise analysis of the improvement of the root-mean-square error can be found in Appendix C.

### 4.2.6. $NO_2$ VCD measurements

After the DOAS fitting process with the implementation of the new wavelength window, the useful output comprises slant column densities, as seen in Figure 4.3. Additionally, the $NO_2$ VCD concentrations are needed to be able to compare with the modelled values. As described in Subsection 2.2.2, the air mass factor is therefore needed for the conversion between SCD and VCD. The air mass factor, however, is expected to change as the changes in $NO_2$ concentration are different for the troposphere and stratosphere, due to the availability of convertible NO. This could cause a change in the profile shape of $NO_2$ which is used as an input for the air mass factor. Consequently, the air mass factor is expected to need adjusting with the use of the model results of the comparison between the non-eclipse and eclipse $NO_2$ profiles. As the explanation and proof for the change in the shape of the $NO_2$ profile will be presented in Subsection 4.4.3, further details will be provided there concerning the air mass factor.

## 4.3. Validation: Adjustment of the $NO_2$ retrieval

Considering the TROPOMI orbit 25850 on 9 October 2022, the vertical column densities retrieved through the original retrieval algorithm are shown in Figure 4.11a, followed by the vertical column densities retrieved through the adjusted retrieval algorithm, shown in Figure 4.11b. The measurements of TROPOMI orbit 25850 are used as a test case since there was no solar eclipse to influence the measurements. Subsequently, the difference in vertical column density between the original and the newly retrieved $NO_2$ concentrations is visualised in Figure 4.11c.

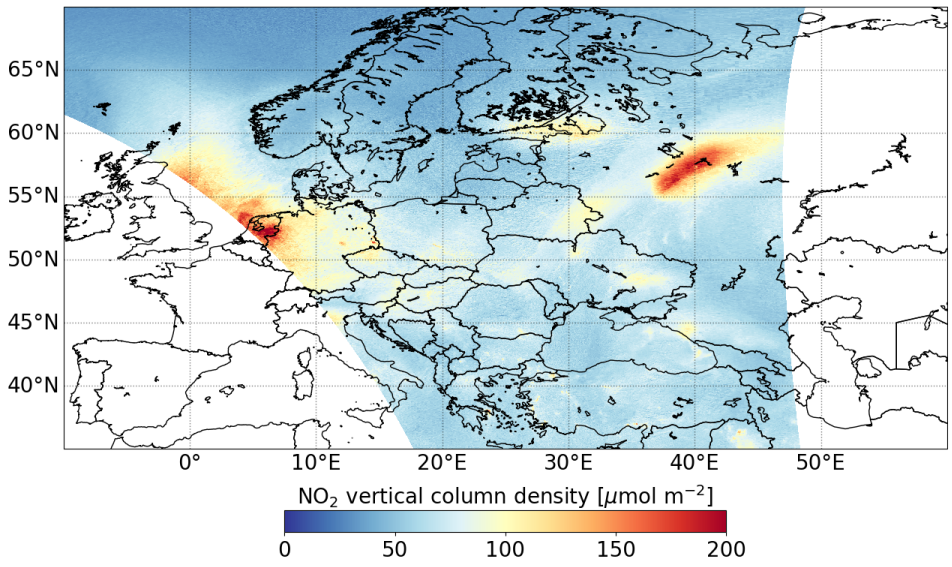


**(a)** Original $NO_2$ retrieval.

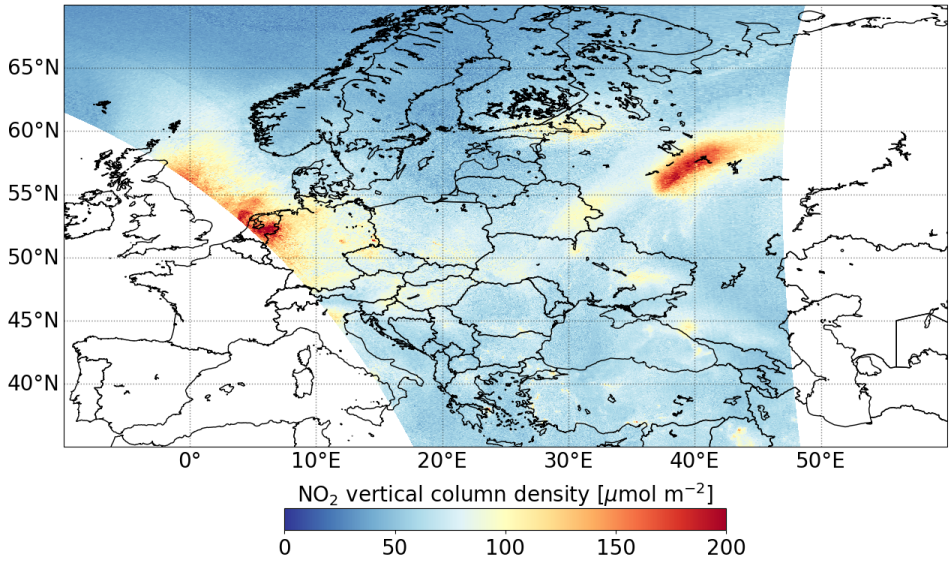


**(b)** Adjusted $NO_2$ retrieval.

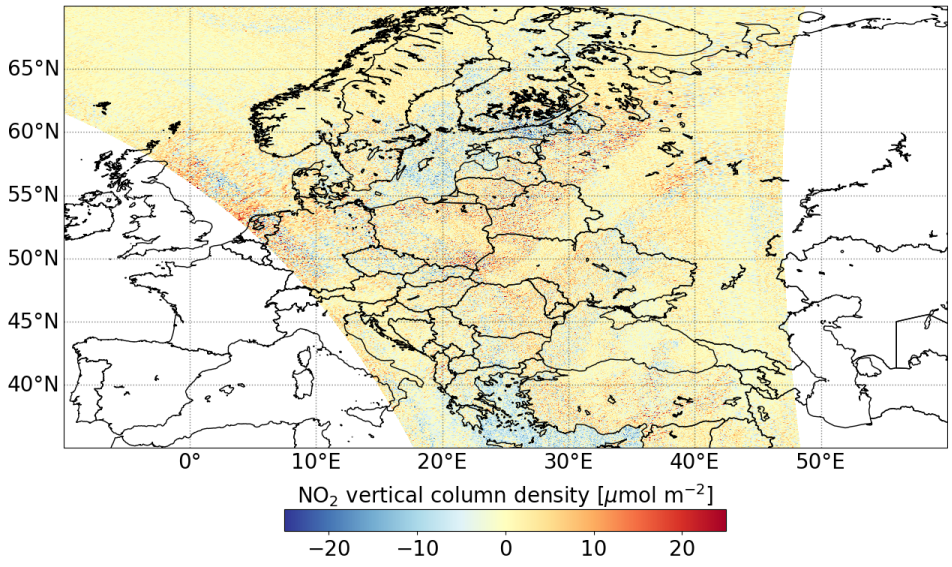


**(c)** Difference between the original and adjusted $NO_2$ retrievals. The difference is calculated by $VCD_{adjusted}$ - $VCD_{original}$.

**Figure 4.11:** Comparison of $NO_2$ vertical density column resulting from the original and adjusted $NO_2$ retrievals of TROPOMI orbit 25850.

From the difference as seen in Figure 4.11c, it can be ensured that the new retrievals for the solar eclipse cases can be trusted. The new retrieval of TROPOMI orbit 25850 shows similar concentrations as the original retrieval and the minor differences that occur fall within the associated uncertainty range of the specified TROPOMI pixels. Moreover, Figure 4.12 shows the correlation between the concentrations retrieved from the original and the new retrieval. The correlation creates another positive vision on the validation using the test case of this orbit as a good correlation is presented with a correlation coefficient of 0.975.

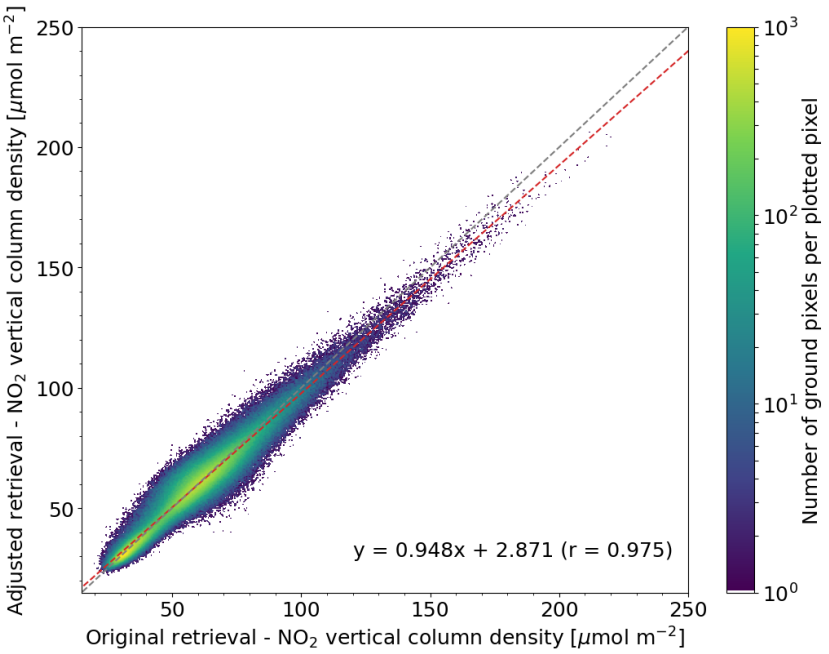


**Figure 4.12:** Correlation plot between the original and adjusted $NO_2$ retrievals of TROPOMI orbit 25850.

### Influence DOAS fitting parameters

Interestingly to note, are the areas above water bodies where clusters of negative differences (in blue) can be seen. The Baltic Sea at 57.5° N and 20° E and the Aegean Sea at 37.5° N and 25° E show these significant differences where the adjusted retrieval algorithm shows lower values than the original retrieval algorithm. This resulted in the land-water transition of the $NO_2$ concentrations to have decreased in comparison to the original retrieval, meaning a relatively lower $NO_2$ concentration is retrieved above water than above land. This can be related to other fitting parameters within the DOAS algorithm. The other fitting parameters could respond differently to the change in retrieval algorithm through the change of wavelength window. Since the DOAS algorithm is solving the best-fitting solution, this can influence the other parameters considered for the fit. Fortunately, these differences are of minor significance compared to the broader context. In addition, the presence of dissimilarities between the adjusted retrieval window and the original retrieval window does not inherently insinuate a negative attribute. As long as the retrieved concentrations are contained within the uncertainty intervals, the adjusted retrieval setup can be trusted.

### Increased uncertainty due to smaller wavelength window

The positive outcome of the validation test of a non-eclipse orbit in this Section ensures the reliability of the adjusted $NO_2$ retrieval. However, with the adjustment of the retrieval where a change of wavelength window is suggested, a minor downside is accompanied as well. With the adjustment, the length of the wavelength window has decreased from 60 nm to 29 nm, which in general terms means that the amount of information used in the retrieval, has decreased. As the vertical column densities measurements have shown, this poses not a problem in the accuracy of the $NO_2$ measurements, but the precision of the measurements does experience a setback. Namely, the slant column uncertainties show an increase between the measurements shown in Figure 4.11a and Figure 4.11b. The mean slant column uncertainty for the original retrieval in Figure 4.11a is 10.19 $\mu$mol m$^{-2}$, while the adjusted retrieval

in Figure 4.11b is computed with a mean slant column uncertainty of 14.08 $\mu$mol m$^{-2}$. Interestingly, this increase in uncertainty matches the principle behaviour of the so-called shot noise, which (when dominant of other noise sources) scales with the square root of the number of samples. Considering the number of wavelengths as the number of samples, we see an approximate decrease of factor 2 between the original wavelength window and the adjusted wavelength window. A multiplication of the noise with $\sqrt{2}$, indeed results in an increase from 10.19 $\mu$mol m$^{-2}$ to 14.08 $\mu$mol m$^{-2}$ of the slant column uncertainty. Although this does not present a major problem, it should be noted. Similarly, this is seen in the slant column uncertainties presented in Figure 4.9 and Figure 4.10. Visual inspection of the figures indicates that ground pixels not influenced by the solar eclipse, increase in slant column uncertainty at for example 68° N and 14° E. Nonetheless, here, an overall improvement of the slant column uncertainty is seen due to the disappearing solar eclipse biases.

## 4.4. Modelling expected $NO_2$ concentrations

In Subsection 2.2.3 it was already covered that a-priori $NO_2$ profiles simulated with the TM5 atmospheric chemistry model are used in the processing of the final TROPOMI $NO_2$ products. This same $NO_2$ profile, together with the NO profile can be used to do model simulations of $NO_2$ for non-eclipse and eclipse conditions. This will be described in Subsection 4.4.1 and Subsection 4.4.2. Finally, the adjustment of the air mass factor based on the $NO_2$ changes during a solar eclipse will be discussed in Subsection 4.4.3.

### 4.4.1. $NO_2$ and $NO_x$ profiles

The $NO_2$ and NO vertical profiles simulated with the TM5 atmospheric chemistry model will first need to be converted from volume mixing ratios to number densities, as the eclipse implementation will be performed using the latter. These conversions can be found in Appendix A. The separation of the atmosphere into multiple layers allows us to analyse the height profiles of the $NO_2$, both before and after the eclipse implementation. Subsequently, these layers can also be summed to create a total column value for the analysis.

### 4.4.2. Eclipse implementation

The eclipse implementation that will be applied is solely based on the photolysis rate of $NO_2$ being influenced by varying magnitudes of sunlight. The descriptions of Equation 2.1 and Equation 2.3 are used in this case, as they represent the full $NO_x$ partitioning during a solar eclipse. The rate of the $NO_2$ photolysis in Equation 2.1 is determined by the photodissociation rate constant $j_{NO_2}$ and the rate constant of Equation 2.3 is $k$. As also described by Adams et al. (2010), Equation 4.9 shows the resulting equilibrium:

$$\frac{[NO_2]}{[NO_x]} = \frac{1}{1 + j_{NO_2}/(k \cdot [O_3])} \tag{4.9}$$

During a solar eclipse, the boundary conditions behind the behaviour of the equilibrium differ for both the stratosphere and the troposphere. Therefore, this will be discussed separately from one another.

#### Stratosphere

In the research executed by Adams et al. (2010), the focus was pointed towards stratospheric measurements as NO and $NO_2$ concentrations between 10 and 52 km were used as inputs. All values below 10 km were deemed not to be of interest and set to the value of 10 km. Furthermore, the ozone profile was considered to be constant throughout the calculations as ozone does not show diurnal variation in the stratosphere (Adams et al., 2010). Additionally, Adams et al. (2010) also conclude that ozone measurements during the solar eclipse show variations within the natural behaviour of ozone and no response to the solar eclipse was seen. Since ozone in the stratosphere is also present in an abundant manner, it is stated that ozone thus doesn't interfere with the photochemical equilibrium in the stratosphere during a solar eclipse. Therefore the variable $r$ is introduced, where $r = j_{NO_2}/k[O_3]$ (Adams et al., 2010). The variable $r$ can be used assuming that ozone remains constant and consequently describes the ratio of the first-order rate constants.

$$\frac{[NO_2]}{[NO_x]} = \frac{1}{1 + j_{NO_2}/(k \cdot [O_3])} = \frac{1}{1 + r} \tag{4.10}$$

### Troposphere

Similarly, the role of photochemistry in the boundary layer during a solar eclipse was analyzed by Fabian et al. (2001) using ground-based observations and box-model simulations. Within the troposphere, the boundary layer is considered to be the dominant layer regarding $NO_2$ concentrations. Consequently, we assume that the statements derived for the boundary layer hold for the entire troposphere and vice versa. For the boundary layer, it holds that measured and modelled changes in $O_3$ showed a significantly lower magnitude of impact on the NO and $NO_2$ partitioning when compared to the impact $j_{NO_2}$ has on the NO and $NO_2$ partitioning (Fabian et al., 2001). The rate constant $k$ only varies with temperature on a scale that is not seen during a solar eclipse. For the effect of $j_{NO_2}$, however, a correlation was found between the modelled and measured values when compared to the $NO/NO_2$ ratio. The strong linear correlation as seen in Figure 4.13, confirms the relation between the photodissociation rate constant and the $NO_x$ partitioning. Consequently, to the first order, the equilibrium is linearly correlated with $j_{NO_2}$ (Warmiński and Bęś, 2009). For Equation 4.11 therefore $\frac{1}{k[O_3]}$ can be considered as a constant and $j_{NO_2}$ as the only variable influencing the changing ratio of $NO_2/NO_x$ on short-time scales.

$$\frac{[NO_2]}{[NO_x]} = \frac{1}{1 + j_{NO_2} \cdot \frac{1}{k \cdot [O_3]}} \tag{4.11}$$

Equation 4.10 and Equation 4.11 combined shows that $j_{NO_2}$ and $r$ are directly related. With the statement about the behaviour of the equilibrium in the troposphere, the solar eclipse implementation as described by Adams et al. (2010) can be used for both the stratosphere and the troposphere.

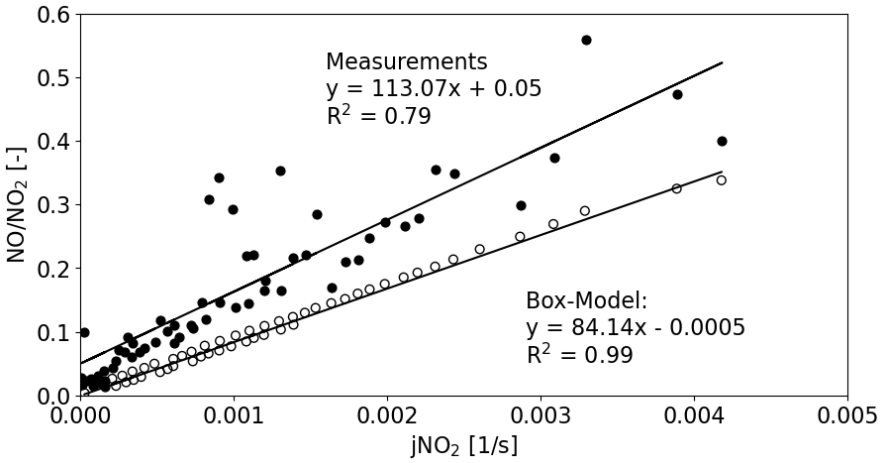


**Figure 4.13:** The $NO/NO_2$ ratio as function of $j_{NO_2}$. Measurements are shown as full circles and model values as open circles. The $NO/NO_2$ ratio is not the same as the $NO_2/NO_x$ ratio like used in Equation 4.11, but considering that $NO_x$ = NO + $NO_2$, the conclusion has a similar outcome (Fabian et al., 2001).

Evidently, the eclipse implementation on the original $NO_2$ profile can be performed by implementing the decreasing rate of photochemistry into the equilibrium equation. This can be done by scaling the rate of $NO_2$ photolysis through $r$ due to the relations shown in Equation 4.10 and Equation 4.11 where $r = j_{NO_2}/k[O_3]$ and $\frac{1}{k[O_3]}$ is found to be constant. Therefore, $j_{NO_2}$ linearly scales with the reduction in sunlight due to the solar eclipse and $r$ can be adjusted by the fraction of the solar disk that is not occulted, which is $(1 - f_o)$. With the computed obscuration fraction $f_o$, the resulting equation is shown in Equation 4.12.

$$[NO_2] = \frac{[NO_x]}{1 + r(1 - f_o)} \tag{4.12}$$

The parameter $r$ describes the original ratio of $NO_2/NO_x$. This ratio is important as it specifies the available NO to be transformed to $NO_2$ (Adams et al., 2010). The computation of $r$ is shown in Equation 4.13.

$$r = \frac{1}{[NO_2]/[NO_x]} - 1 \tag{4.13}$$

In addition, by using the value $r$ instead of trying to correctly calculate the rates $j_{NO_2}$ and $k$ during a solar eclipse, the full chemistry model used in the TM5 model is represented in the values of NO and $NO_2$, as all other chemical reactions regarding the $NO_2$ cycle are incorporated (Adams et al., 2010). Photolysis of $NO_2$ occurs around the wavelengths of 390 nm (Fabian et al., 2001), which is why the obscuration fraction for the application of the eclipse implementation will be performed for 390 nm.

At last, the ratio $\frac{[NO_2]}{[NO_x]}_{\text{eclipse}}$ can be computed as function of $\frac{[NO_2]}{[NO_x]}_{\text{no eclipse}}$ as seen in Equation 4.14. The obscuration fraction is responsible for an increase in the $NO_2/NO_x$ eclipse ratio, as an obscuration fraction between 0 and 1 will result in the denominator never being higher than a value of 1. Consequently, the $NO_2/NO_x$ non-eclipse ratio in the numerator is transformed to a higher $NO_2/NO_x$ eclipse ratio as a result. Following the eclipse implementation, the model estimated $NO_2$ during a solar eclipse can be analysed and compared to the eclipse-adjusted measurements from TROPOMI.

$$\frac{[NO_2]}{[NO_x]}_{\text{eclipse}} = \frac{\frac{[NO_2]}{[NO_x]}_{\text{no eclipse}}}{f_o \cdot \left(\frac{[NO_2]}{[NO_x]}_{\text{no eclipse}} - 1\right) + 1} \tag{4.14}$$

### 4.4.3. Air mass factor

As described in Subsection 2.2.2, the air mass factor is needed to convert slant column densities to vertical column densities. The three components of the air mass factor, namely the altitude-dependent AMF (i.e., the light paths), the column density profile and the temperature correction, are discussed individually on their contribution to the changing air mass factor during a solar eclipse. To begin with, the temperature correction is assumed to not be influenced by the solar eclipse as the temperature changes are insignificant. As was found by Anderson (1999) and Wu et al. (2011), surface temperatures do show a response to the solar eclipse, but the temperature profile of the atmosphere does not show a significant change. Fluctuations of 3° C were reported by Sun et al. (2022), who measured the atmospheric temperature during the solar eclipse on 21 June 2020 over Tibet. However, with respect to the magnitudes of the temperature profile through the atmosphere, which ranges from +20° C to -90° C, these fluctuations are expected not to significantly influence the shape of the temperature profile. Additionally, atmospheric turbulence creates another unreliable factor which influences the local circumstances related to the temperature profile. Consequently, the temperature correction is regarded to have an irrelevant effect on the air mass factor during a solar eclipse.

Secondly, the altitude-dependent AMF is assumed to remain similar to the non-eclipse value as the average light path is not affected. The research from Trees et al. (2021) shows that no corrections of the direct to diffuse radiation are needed in the partial shadow as they were able to compute good results without any correction on that part. Moreover, Ockenfuß et al. (2020) found that the contribution of diffuse radiation during a solar eclipse showed no relevant influence when compared to the direct radiation. The change in the radiative transfer model is assumed to be little considering the change in the median wavelength of the window, around which the model is computed, is from 440 nm to 452 nm. Additionally, within the new wavelength window ranging from 438 nm to 467 nm, the wavelength of 440 nm is still included, which makes the radiative transfer model still valid for use. This is also found in the non-eclipse test case of orbit 25850 retrieved on the 9th of October 2022, which was discussed in Section 4.3. This orbit matches the repeat cycle from the previously used TROPOMI orbit 26077 and is used to have more or less similar concentration and emission properties over the same region of interest. Figure 4.12 compares the retrieval of the different wavelength windows, which shows a good correlation. Therefore, the altitude-dependent AMF is assumed not to change when the window correction is applied.

However, the vertical $NO_2$ profile is expected to change during the solar eclipse. This is due to the differing availability of the reactants for the photochemical reactions to take place. The lower troposphere and the stratosphere differ in their $NO/NO_2$ ratios and therefore relative differences will occur in the conversion of NO to $NO_2$. Consequently, Equation 4.12 and Equation 4.13 show this relation through the variable $r$ (Adams et al., 2010). The relative contribution of the atmospheric layers to the total $NO_2$ column will then change and this will be seen in the $NO_2$ profile. The air mass factor uses the $NO_2$ profile as one of its inputs, as seen in Equation 2.18. By correcting the air mass factor through the

$NO_2$ profile, the retrieval of $NO_2$ can be further improved for the eclipse effects. Figure 4.14 shows and confirms the hypothesis of the difference in $NO_2$ increase between the troposphere, in the boundary layer, and the stratosphere.

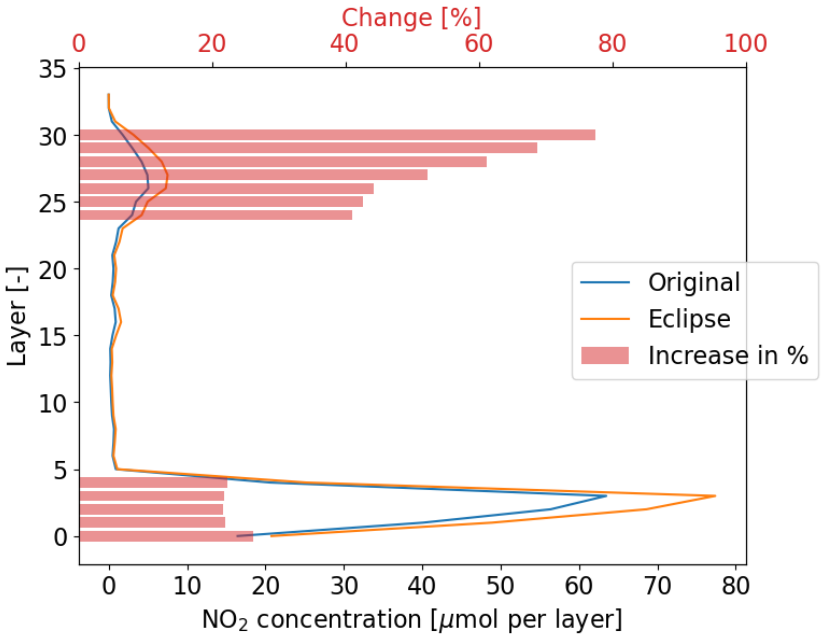


**Figure 4.14:** Vertical profile of $NO_2$ above highly polluted region, showing original $NO_2$ concentrations (in blue) and eclipse implemented $NO_2$ concentrations (in orange). Additionally, the increase in percentage (in red bars) is shown per atmospheric layer.

The air mass factor can be corrected by using the eclipse-corrected TM5 model calculations. The changed distribution of $NO_2$ through the different atmospheric layers indicates the changed $NO_2$ profile. With the help of the averaging kernels ($A_l$) provided in the TROPOMI Level-2 file, the changed $NO_2$ profile ($v_l$) can correct the air mass factor for the influence of the solar eclipse. The correction is applied using the equation as presented by Eskes et al. (2022) and results in the corrected air mass factor ($M_{\text{corr}}$) through Equation 4.15:

$$M_{\text{corr}} = M \sum_l A_l \, v_l / \sum_l v_l \tag{4.15}$$

The mean change in the air mass factor results in an approximate 1.26% increase for all ground pixels, where the air mass factors increase within a range of 0.01 and 0.18. Inherently, the correction of the air mass factor is therefore experienced the strongest over areas with high $NO_2$ concentrations, mostly originating from sources with high pollution near the surface. The air mass factors based on the uncorrected vertical $NO_2$ profiles therefore have values of 0.85-14.49 with a mean of 3.41. The air mass factors based on the corrected vertical $NO_2$ profiles present values of 0.86-14.67 with a mean of 3.45. For pixels containing the highest $NO_2$ concentrations, this meant that a maximum decrease in the vertical density column of 11.29 $\mu$mol $m^{-2}$ is seen. Considering all pixels within the shadow of the solar eclipse, a mean decrease in VCD of 0.84 $\mu$mol $m^{-2}$ is seen as a direct response to the improvement of the air mass factor.

# 5

# Results & Discussion

In the previous Chapter, the methods were explained how to remove the solar eclipse-related biases in the TROPOMI $NO_2$ measurements and how to take into account the solar eclipse effect in the atmospheric chemistry model TM5. In this Chapter, we show the results of the adjusted $NO_2$ TROPOMI measurements and the estimated $NO_2$ concentration during a solar eclipse from TM5. We present the results for two solar eclipse cases over Northern Europe: the solar eclipse of 10 June 2021 and of 25 October 2022.

## 5.1. Measurements from $NO_2$ retrieval

The methodology regarding the adjustment of the $NO_2$ retrieval, as visualised in Figure 4.3, has resulted in improved $NO_2$ concentrations from the measurements taken during the solar eclipses. The improved $NO_2$ concentrations are solely based on the adjustment performed in the processing chain of the TROPOMI measurements. This includes the radiance correction based on the obscuration fraction, the implementation of the new wavelength window and the adjustment made to the air mass factor.

### 5.1.1. Solar eclipse case of 10 June 2021

First, the plot of the obscuration fractions ($f_o$) is shown in Figure 5.1, to get an understanding of the geometry of the shadow of the solar eclipse that influences the $NO_2$ concentrations.

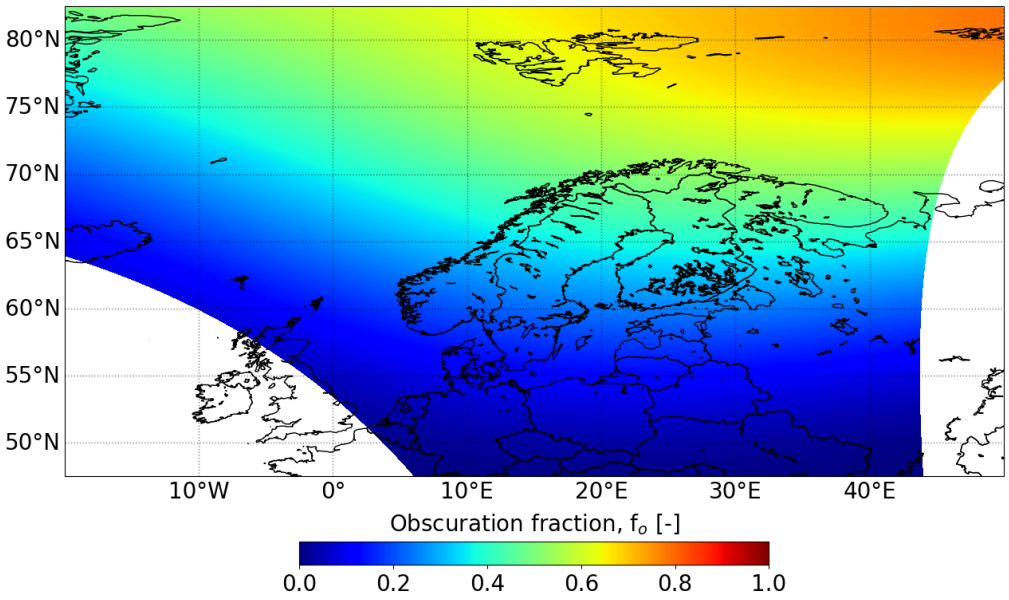


**Figure 5.1:** Obscuration fraction of the solar eclipse during the TROPOMI orbit 18955.

Figure 5.1 shows the calculated $f_o$ for all ground pixels in the region of interest of the solar eclipse captured by the TROPOMI orbit 18955 (see Equation 4.1). The obscuration fractions are shown as a snapshot of the experienced level of obscuration at the moment of measurement taken by TROPOMI. It lacks in this sense the complete dynamic influence of the solar eclipse. In the orbit, the antumbra was not captured. Nonetheless, here a maximum obscuration fraction, calculated at 440 nm, was found to be 0.820 at 83.60° N and 65.57° E. However, this is slightly outside of the visualised region as shown in Figure 5.1, which comes as a consequence of selecting the region of interest to be visualised in further analysis. Nonetheless, around 82.50° N and 50° E, the obscuration fractions of 0.8 are still encountered, which will be well enough for further analysis.

During this solar eclipse, TROPOMI was able to take measurements as their paths crossed above Northern Europe. The original vertical column densities are shown in Figure 5.2a, followed by the improved vertical column densities shown in Figure 5.2b. Consequently, the difference in vertical column density between the original and the newly retrieved $NO_2$ concentrations is visualised in Figure 5.2c. It must be noted that the following changes and differences seen in the $NO_2$ concentrations are related to the improvement of the retrieval algorithm and are not related to the actual change in $NO_2$ concentration in the atmosphere due to the solar eclipse. These will be elaborated on later in Section 5.2 and Section 5.3.

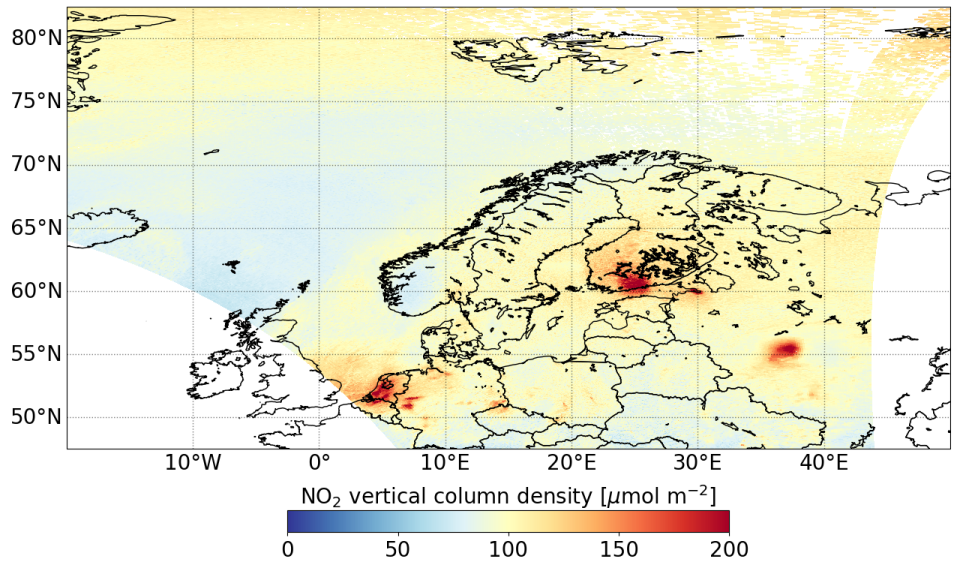


**(a)** Original $NO_2$ retrieval.

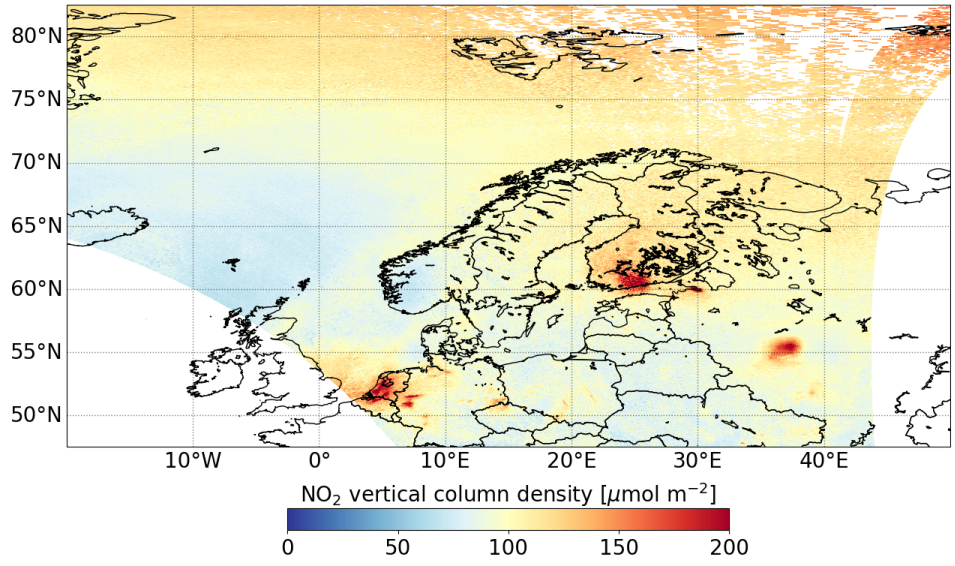


**(b)** Adjusted $NO_2$ retrieval.

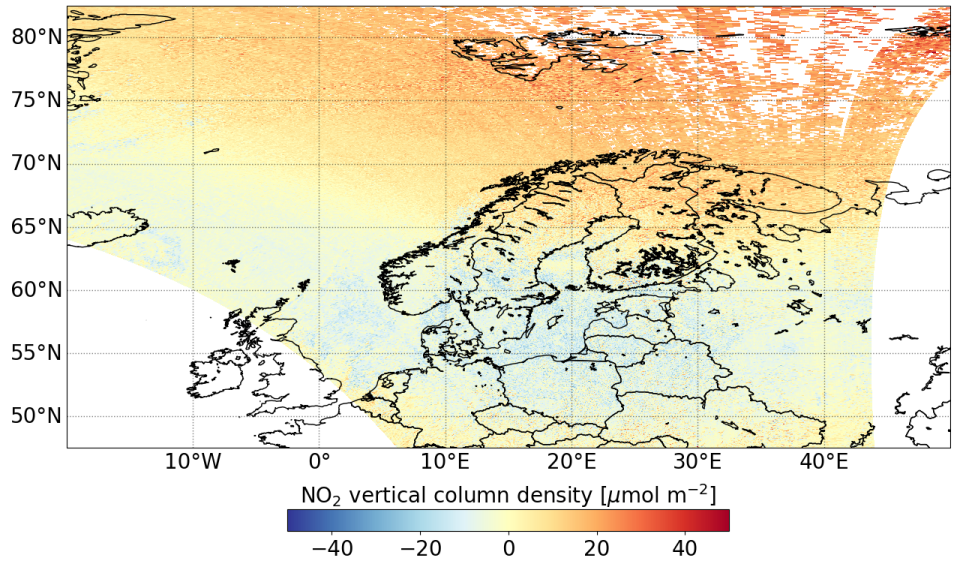


**(c)** Difference between the original and adjusted $NO_2$ retrievals. The difference is calculated by $VCD_{adjusted}$ - $VCD_{original}$.

**Figure 5.2:** Comparison of $NO_2$ vertical density column resulting from the original and adjusted $NO_2$ retrievals of TROPOMI orbit 18955.

Figure 5.2c shows the difference in $NO_2$ concentration between the original and adjusted $NO_2$ retrievals where to the north of 70° N a significant positive difference is encountered. This is in line with the increased obscuration fraction $f_o$ as we have seen in Figure 5.1. As discussed before in Chapter 3, the pixels in the north of this orbit suffer from the eclipse effects, accompanied by the difficulties related to the high solar zenith angle. Nonetheless, a gradual increase in differences is visible in the comparison when going from the south to the north. Furthermore, a region of blue values can be spotted between the latitudes of 50° N and 60° N. These blue values show a negative trend as these pixels received a lower $NO_2$ concentration in the adjusted retrieval than in the original retrieval. This region agrees well with where the obscuration fraction is $0 < f_o < 0.3$. When analyzing the wavelength spectra in Figure 4.5 for these obscuration fractions, the lower $NO_2$ concentrations here can be explained by the negative residuals shown. Interestingly, the already high concentration values in the original retrieval are exceeded by the concentrations of the adjusted retrieval. In any case, Figure 5.2b shows that the enhanced $NO_2$ concentration values during this eclipse are still observed after the retrieval algorithm adjustment, suggesting that the $NO_2$ concentration increase in the atmosphere is real and not an eclipse-induced bias.

When considering the validity of the adjusted measurements, the comparison to adjacent orbits is now possible as the retrieval is found to be reliable. The adjusted $NO_2$ measurements from the eclipse orbit are plotted with the $NO_2$ measurements from the prior and following orbits in Figure 5.3.

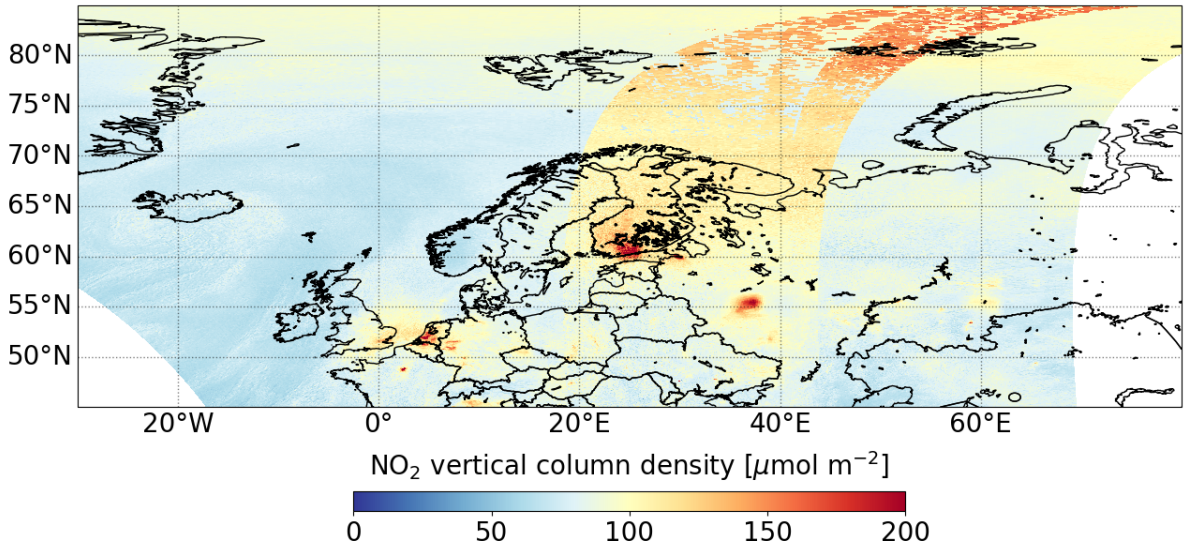


**Figure 5.3:** Map with $NO_2$ vertical column densities of 3 sequential orbits, including the orbit with solar eclipse in the middle.

Indeed, the apparent increase in $NO_2$ is clearly distinguished at the sharp boundaries with the adjacent orbits. As only small portions of the orbit are overlapping, the difference between non-eclipse and eclipse will be better analysed through the TM5 atmospheric chemistry model. The model results as will be presented in Section 5.2 will quantify the increase in $NO_2$ seen in Figure 5.3 and experienced during a solar eclipse.

### 5.1.2. Solar eclipse case of 25 October 2022

The obscuration fractions during the solar eclipse on 25 October 2022 will again first be shown in Figure 5.4, to get an understanding of the shadow cast on the Earth's surface by the moon.

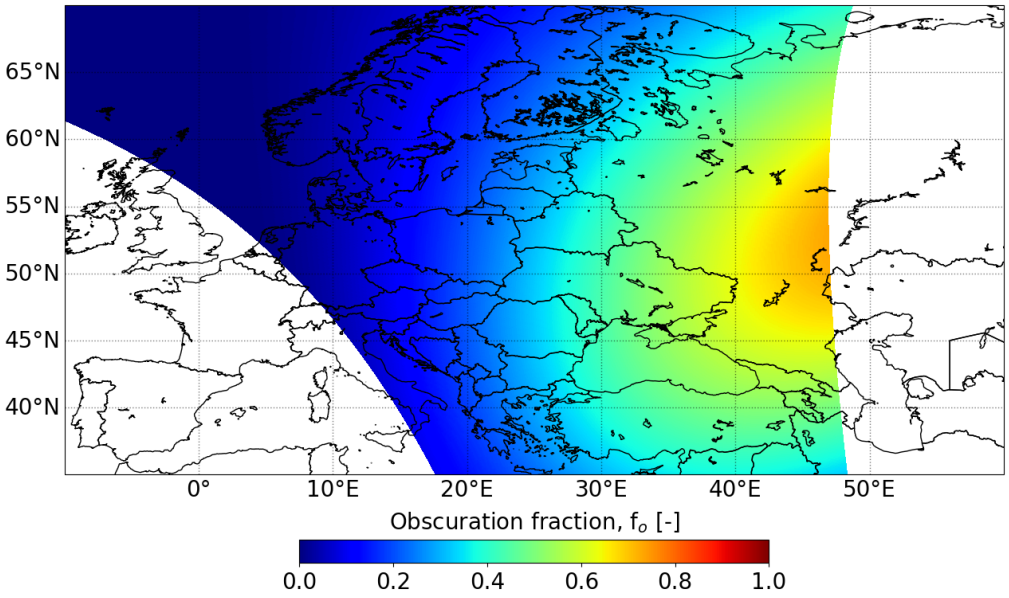


**Figure 5.4:** Obscuration fraction of the solar eclipse during the TROPOMI orbit 26077.

As can be concluded from the shown obscuration fractions of the solar eclipse, calculated at 440 nm and illustrated in Figure 5.4, the antumbra was not captured in the TROPOMI orbit 26077. It holds that the maximum obscuration fraction $f_o$ calculated for this orbit was 0.734 at 52.50° N and 46.89° E. Even though the antumbra of the solar eclipse was not captured by the orbit, a nice and clear circular geometry was captured. This creates the opportunity to analyse similar magnitudes of influence over different regions containing various $NO_2$ concentration properties.

#### Importance of Moon shadow type

It must be noted that the application of the research done here, is based on the antumbra parts of the shadow related to the solar eclipse. Here, direct sunlight reaches the surface which is dominant over the sunlight travelling horizontally through the atmosphere during a solar eclipse. For both cases, the maximum obscuration fractions observed were 0.8 and 0.734 and therefore the direct sunlight was dominant to horizontally travelling sunlight because only the penumbra had to be considered. When applying corrections and adjustments to the umbra part of a solar eclipse shadow, close attention has to be paid to the incorporation of horizontally travelling light, as that will be the only source of sunlight. Moreover, Equation 4.3 and Equation 4.4 as described in Subsection 4.2.1 will not perform as expected.

Considering the solar eclipse on 25 October 2022, orbit 26077 from TROPOMI coincided with the path of the solar eclipse to take valuable measurements. The original vertical column densities are shown in Figure 5.5a, followed by the improved vertical column densities shown in Figure 5.5b. Consequently, the difference in vertical column density between the original and the newly retrieved $NO_2$ concentrations is visualised in Figure 5.5c. It must be noted that the following changes in $NO_2$ concentrations are related to the improvement of the retrieval algorithm and are not related to the actual change in $NO_2$ concentration in the atmosphere due to the solar eclipse. These will be elaborated on later in Section 5.3.

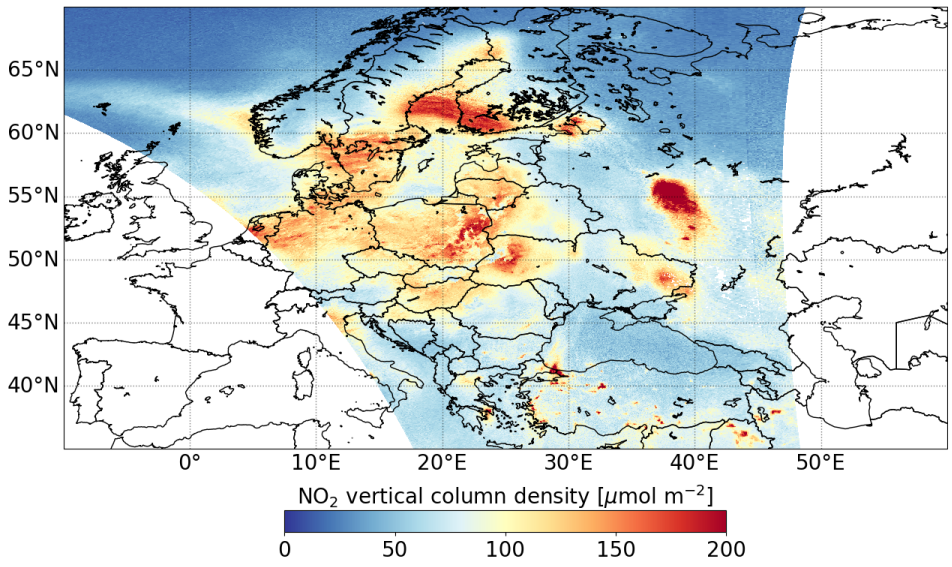


**(a)** Original $NO_2$ retrieval.

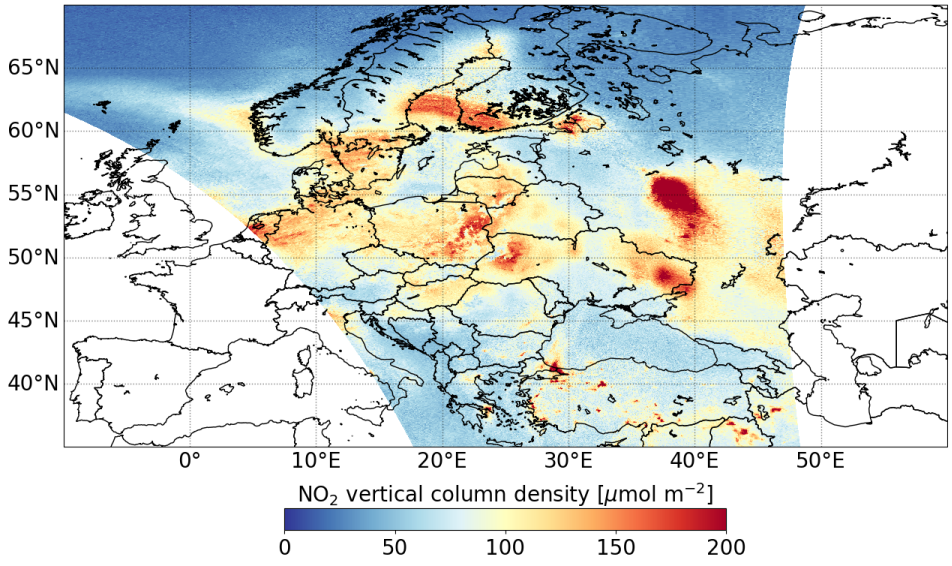


**(b)** Adjusted $NO_2$ retrieval.

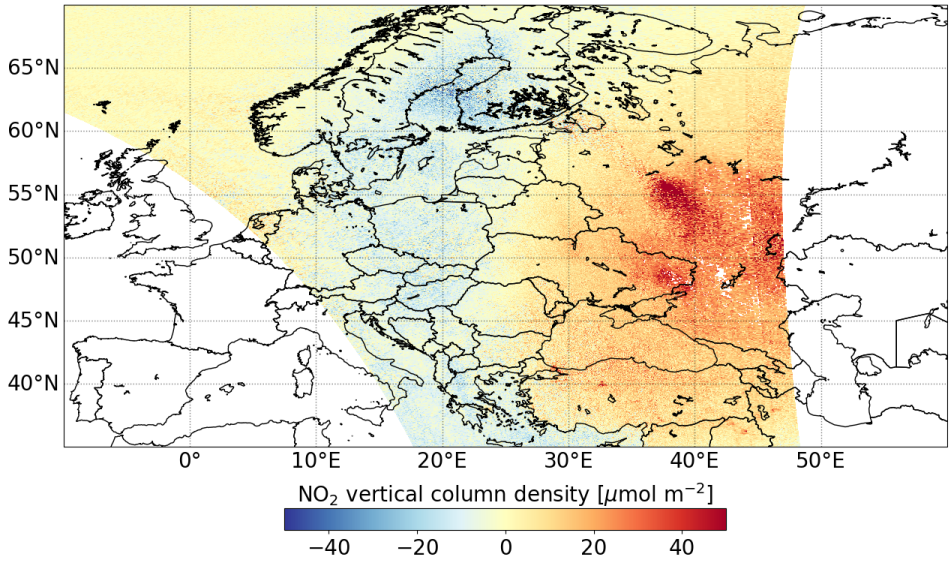


**(c)** Difference between the original and adjusted $NO_2$ retrievals. The difference is calculated by $VCD_{adjusted}$ - $VCD_{original}$.

**Figure 5.5:** Comparison of $NO_2$ vertical density column resulting from the original and adjusted $NO_2$ retrievals of TROPOMI orbit 26077.

Figure 5.5c shows the difference between the original and adjusted $NO_2$ vertical column densities. The red values at the east side of the orbit show positively orientated values towards 50 $\mu$mol m$^{-2}$, which describes the increase of $NO_2$ for the adjusted retrieval with respect to the original retrieval. Likewise, as in the TROPOMI orbit 18955, this orbit shows a region of negative differences for areas experiencing an obscuration fraction of $0 < f_o < 0.3$. A curve of blue values can be spotted starting and curving around 20° E longitude, moving from east of 20° E to west and back to east 20° E with increasing latitude. Consequently, it can be stated that the shape of the changes shown in Figure 5.5c coincides closely with the shape of the eclipse shadow as described by the obscuration fraction in Figure 5.4. Evident from the figures in Figure 5.5 is again the strong confirmation of the increase $NO_2$ with the adjusted retrieval. Therefore, the high $NO_2$ concentrations can be discarded as a measurement artefact and be related to the actual chemistry in the atmosphere, as a result of the solar eclipse.

After the correct retrieval of the orbit influenced by the solar eclipse, the comparison to adjacent orbits can be done as all measurements are of similar quality. The adjusted $NO_2$ measurements from the eclipse orbit are plotted with the $NO_2$ measurements from the prior and following orbits in Figure 5.6.

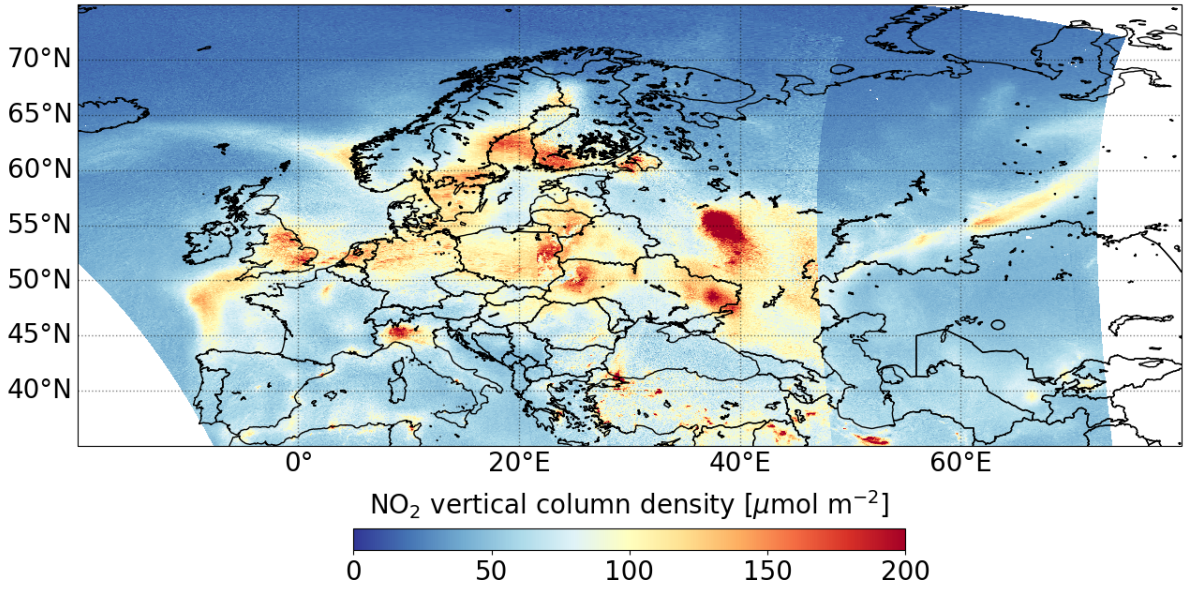


**Figure 5.6:** Map with $NO_2$ vertical column densities of 3 sequential orbits, including the orbit with the solar eclipse in the middle.

In Figure 5.6, a sharp boundary is seen between the right and middle TROPOMI orbits. This boundary is indicative of a change in atmospheric composition as normal orbit-to-orbit variations are not expected to be this significant. Interestingly, the transition to the following orbit on the left appears not to show a significant boundary between the measurements. This could be related to the low influence of the solar eclipse, as the observed obscuration fractions were low. Another explanation could be that the atmosphere has already recovered from the effects of the solar eclipse, as the resulting shadow was moving from the west to east. Nevertheless, the considerable increase seen at the transition between orbits will be analysed in Section 5.3, where the TM5 model will provide the necessary eclipse model values for the orbit.

### Change of $NO_2$ measurements

The change in $NO_2$ concentrations of both orbit 18955 and 26077 is in line with the expectation based on the calculated obscuration fractions experienced during the solar eclipses. It is interesting to see that the high, and unreliable, $NO_2$ concentrations from the original retrievals are overtaken by even higher $NO_2$ concentrations in the improved retrievals. Here, improvements in the slant column density results were dominant over the improvements seen from the air mass factor adjustment in terms of the resulting vertical column density. The slant column density improvements showed a significant correlation with the intensity of the eclipse shadow, whereas the influence of the adjusted air mass factor was only apparent over highly polluted regions. This part of the analysis, however, is not to be thought

of as proof for the magnitude of the increase of $NO_2$ during a solar eclipse due to photochemistry. The specific increase as the effect of photochemistry will be provided in Section 5.3. Here, in this section, we showed the improvements made by the adjusted retrieval algorithm of $NO_2$ as the sunlight's properties, under the influence of the solar eclipse, were disrupting the original retrieval process of the $NO_2$ vertical column densities.

## 5.2. $NO_2$ modelling vs. measurements: Solar eclipse 10 June 2021

The adjusted measurement results have indicated that an increase of $NO_2$ is the result of the influence of a solar eclipse and are again shown in Figure 5.7a. With comparison to model values, we can quantify the extent of the increase. Through the use of the atmospheric chemistry model TM5 and the originally predicted $NO_2$ values, the expected values without the influence of the solar eclipse can be computed. Since the TM5 model itself does not include any influence of possible solar eclipses, the values shown in Figure 5.7b can be seen as the expectation in $NO_2$ concentrations when no solar eclipse would have occurred during the TROPOMI orbit 18955 on 10 June 2021. Additionally, the eclipse implementation as described in Subsection 4.4.2 is applied to the $NO_2$ values, alongside the associated NO values, to be able to model the expected $NO_2$ concentrations during a solar eclipse. The resulting eclipse modelled $NO_2$ values of the pixels of TROPOMI orbit 18955 are shown in Figure 5.7c.

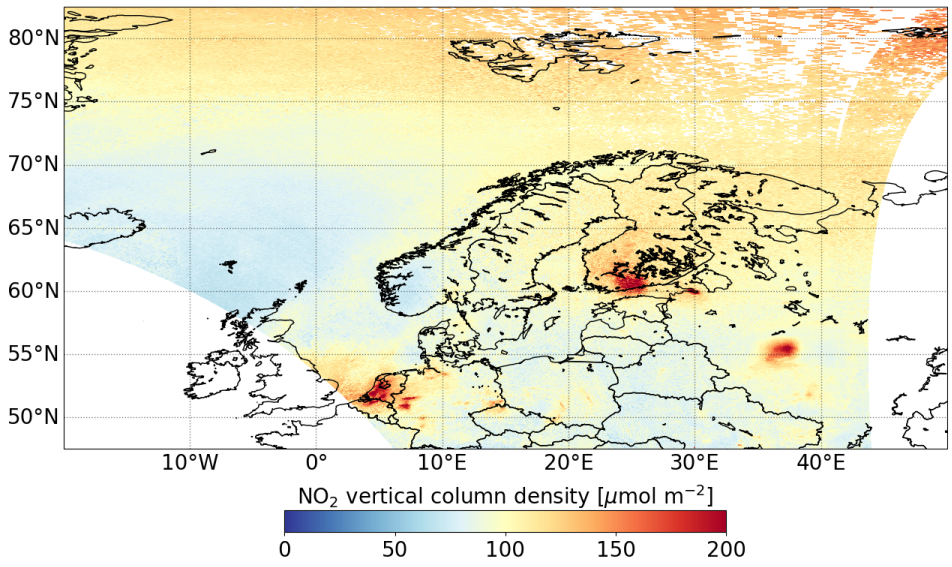


**(a)** Adjusted $NO_2$ concentration measurements.

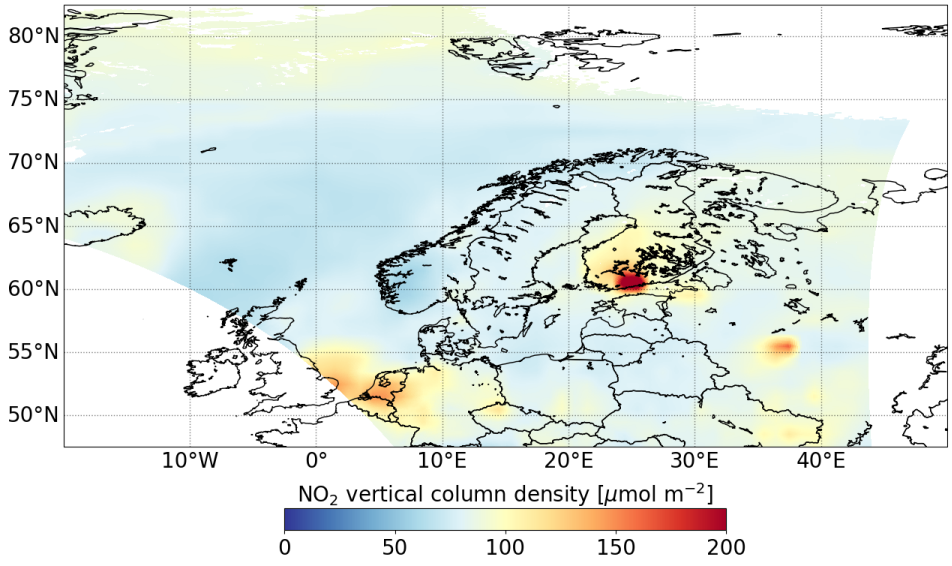


**(b)** Expected non-eclipse $NO_2$ concentrations by TM5.

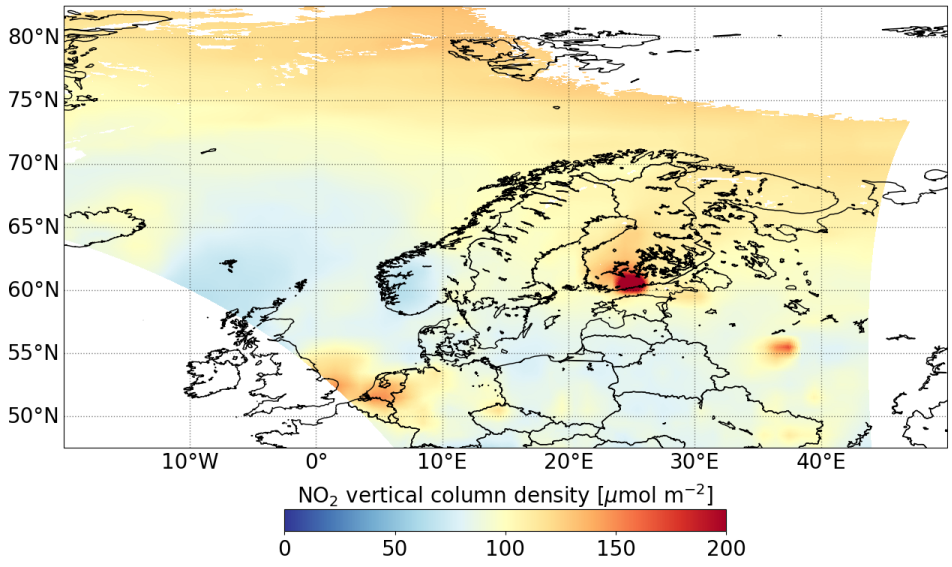


**(c)** Expected eclipse $NO_2$ concentrations by TM5.

**Figure 5.7:** Comparison of measurements and model $NO_2$ concentrations of TROPOMI orbit 18955.

Overall, no major remarkable observations are discovered in Figure 5.7b. It stands out that the $NO_2$ concentrations above rural areas like The Netherlands, Helsinki and Moscow are considerably higher than their neighbouring areas, but this is expected as emissions are higher above highly populated areas. Nonetheless, the uncertainty ranges of the vertical column densities from the original retrieval do show similar high values in these areas and compared to the measurements in Figure 5.7a, the modelled values above The Netherlands and Moscow are still lower. The expected $NO_2$ concentrations in Figure 5.7c, calculated with the use of the TM5 model, introduce a general trend of increasing $NO_2$ values in the northern parts of the orbit. This is the result of the incorporation of the obscuration fraction into the eclipse implementation. From the comparison between the figures in Figure 5.7, visually a good agreement can be seen between the measurements in Figure 5.7a and the eclipse implemented model values in Figure 5.7c. In the north of the orbit, a curve pattern is presented in both figures where the $NO_2$ concentrations are increasing. The $NO_2$ concentrations for the non-eclipse expectation in Figure 5.7b merely show uniformly distributed values. The differences will be even more pronounced in the following figures and analysis.

The comparison between the non-eclipse expected $NO_2$ and the concentrations retrieved from the measurements gives a first indication of the behaviour of $NO_2$ under the solar eclipse conditions. Subsequently, the difference between the modelled expected eclipse $NO_2$ concentration and the $NO_2$ measurements are computed. This will visualise the agreement between the model values and the measurements and can indicate the assumed photochemistry in the atmosphere. The difference between the measurements and both the non-eclipse and eclipse model values are shown in Figure 5.8, in addition the their absolute $NO_2$ concentrations.

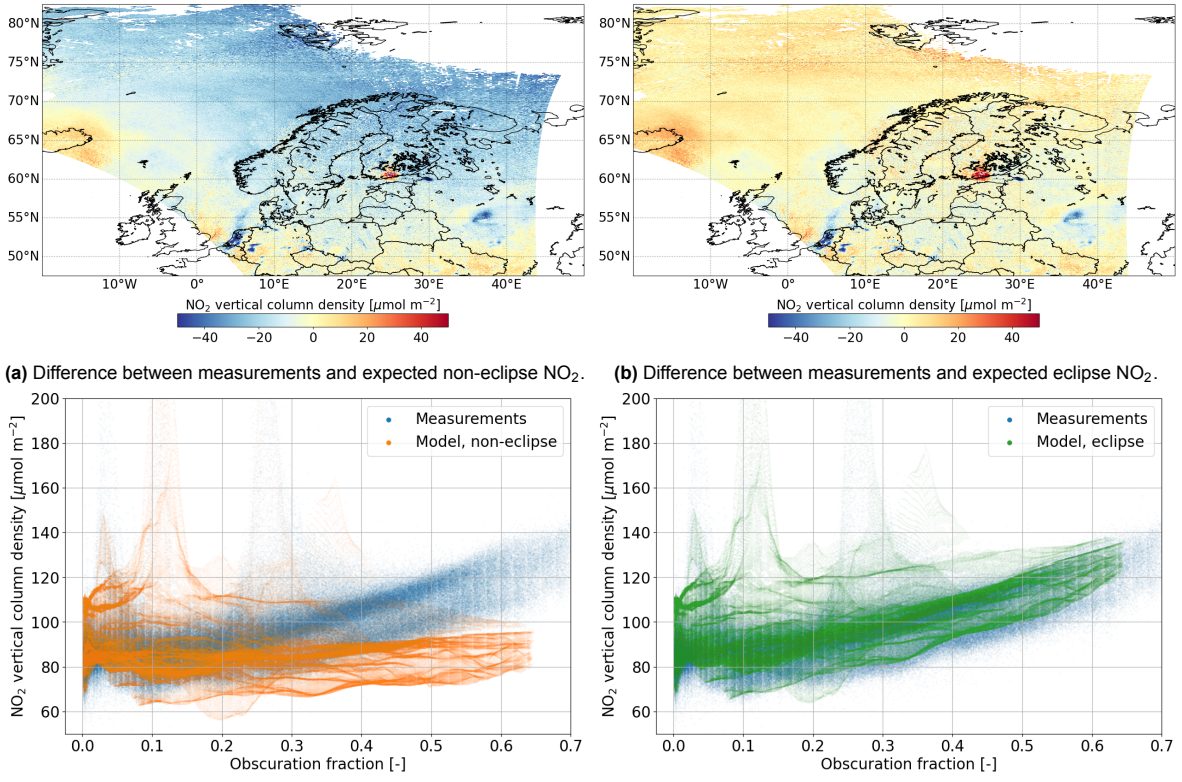


**(a)** Difference between measurements and expected non-eclipse $NO_2$.

**(b)** Difference between measurements and expected eclipse $NO_2$.

**(c)** Absolute $NO_2$ concentrations of the measurements and expected non-eclipse versus obscuration fraction.

**(d)** Absolute $NO_2$ concentrations of the measurements and expected eclipse versus obscuration fraction.

**Figure 5.8:** Differences (in **(a)** and **(b)**) between the $NO_2$ concentrations (in **(c)** and **(d)**) of the measurements and TM5 model values for both non-eclipse and eclipse expectations of TROPOMI orbit 18955. The differences in **(a)** and **(b)** are calculated by $VCD_{model}$ - $VCD_{measurements}$. Unfortunately, in all four plots the $NO_2$ data from the TM5 model is missing for obscuration fractions higher than 0.63, which was caused by an irreversible loss of TM5 pixels during the regridding of the data in combination with the bad quality flag.

The differences as seen in Figure 5.8a show a general trend where the differences become more

negative towards the north of Europe. This is adversely in line with the increase in obscuration fraction calculated for the solar eclipse, as shown in Figure 5.1, which increases towards the north. Similar is evident from the concentrations plotted in Figure 5.8c, where the non-eclipse model values deviate increasingly from the measurements with increasing obscuration fraction. Figure 5.8b and Figure 5.8d on the other hand show a general agreement between the measurements and model values where no specific patterns are recognised, apart from the increase of $NO_2$ with obscuration fraction. Interestingly, $NO_2$ concentrations over Helsinki at 60° N and 25° E seem to be significantly over-estimated in the TM5 model calculations for both the non-eclipse and eclipse model values shown in Figure 5.8. This considerable difference does not fall within the expectation that the model values would be substantially overestimated. Moreover, the high sensitivity to surface emissions in these areas can make it difficult to model and predict the specific emissions that will take place within the TM5 model. Indications for this can be seen in Figure 5.8c and Figure 5.8d, where the model concentrations show steeply increasing peaks which are not directly seen in the measurements. Consequently, we could say that these differences in small areas of the orbit are not related to the solar eclipse effects.

### Dissimilarity of atmospheric sensitivity

An alternative explanation for the discrepancies seen is related to the results from box-model simulations of the atmospheric boundary layer during a solar eclipse done by Wu et al. (2011). The results show that the effects on $NO_2$ above highly polluted areas are significantly higher than for unpolluted areas. In addition, Wu et al. (2011) showed that for highly polluted areas the progression and regression of the $NO_2$ response to the solar eclipse was not symmetrical. To return to 'before eclipse' conditions it took longer than the time needed to build up to the conditions at the maximum of the solar eclipse. In our research, the eclipse implementation was applied based on the availability of sunlight and therefore the resulting $NO_2$ concentrations are computed as a direct response to the amount of light present. Consequently, our results do not incorporate a possible delay of the recovery of the $NO_2$ equilibrium. This can partly explain the differences seen above The Netherlands and Moscow where the adjusted eclipse measurements show higher values than the modelled values. This indicates that for areas with high pollution, different factors can come into play when considering the sensitivity of the atmosphere.

Overall, the measurements show higher values of $NO_2$ concentrations for pixels with higher obscuration fractions than the non-eclipse model values, while the eclipse model values show a close agreement with the measurements. To quantitatively analyse the effect of the eclipse implementation, the differences as presented in Figure 5.8 are plotted versus the obscuration fraction in Figure 5.9.

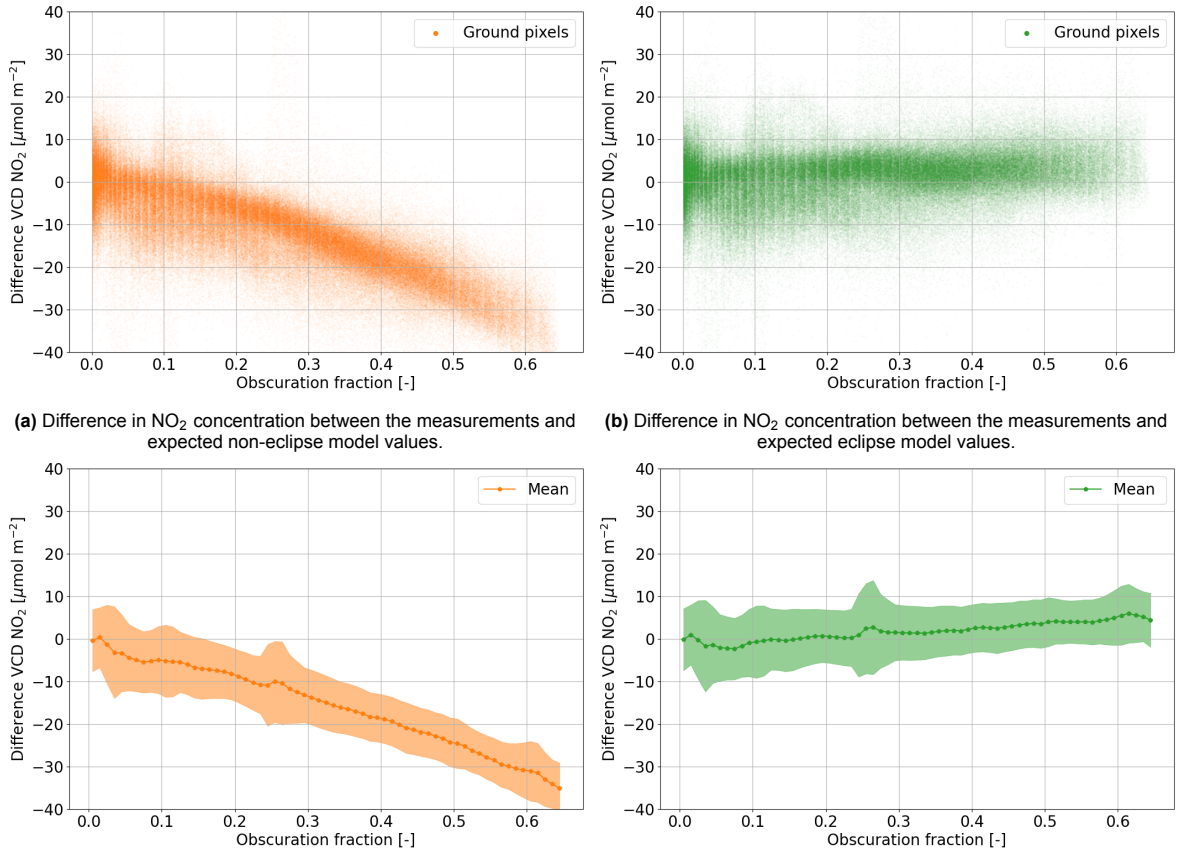


**(a)** Difference in $NO_2$ concentration between the measurements and expected non-eclipse model values.

**(b)** Difference in $NO_2$ concentration between the measurements and expected eclipse model values.

**(c)** Mean of the differences as presented above.

**(d)** Mean of the differences as presented above.

**Figure 5.9:** Absolute differences in $NO_2$ concentrations between measurements and TM5 model values versus obscuration fraction for both non-eclipse (**a**) and eclipse (**b**) expectations of TROPOMI orbit 18955. The differences are calculated by $VCD_{model}$ - $VCD_{measurements}$. The mean of the differences (in **(c)** and **(d)**) are calculated based on bins of obscuration fractions of size 0.01.

In Figure 5.9a we can see that with increasing obscuration fraction, differences between the measured and modelled data sets are growing significantly. We see mean differences up to 30 $\mu$mol $m^{-2}$ for pixels with an obscuration fraction of 0.6. Non-eclipse, reference vertical column uncertainties are exceeded as they on average range between 5 and 15 $\mu$mol $m^{-2}$, including both polluted and unpolluted areas. In comparison to Figure 5.9c, Figure 5.9d shows an evident improvement of the differences between the measurements and the modelled values. The improvement shows that the modelled $NO_2$ concentrations are now more accurately representative of the $NO_2$ concentration during a solar eclipse.

In-depth analysis showed that the discrepancies as discussed and seen in Figure 5.8b for the specific areas again are encountered in the data in Figure 5.9d. This is for example seen in the confidence regions where between obscuration fractions 0.0 and 0.1 a little peak is seen which exceeds the -10 $\mu$mol $m^{-2}$ and corresponds to the negative differences seen above The Netherlands in Figure 5.8b. The positive peak of the confidence interval exceeding the +10 $\mu$mol $m^{-2}$ between obscuration fractions 0.2 and 0.3 is related to the positively orientated differences above Helsinki, as seen in Figure 5.8b.

The results from Figure 5.9 illustrate that the solar eclipse has a significant influence on the $NO_2$ concentrations. The agreement between the measurements and the model values resulting from the eclipse implementation shows that the $NO_2$ concentrations in the atmosphere increase as a response to the decreasing amount of incoming sunlight. Lastly, the non-eclipse model values will help us to quantify the increase of $NO_2$ during a solar eclipse as the difference between it and the measurements accurately display the increase of $NO_2$ caused by the solar eclipse.

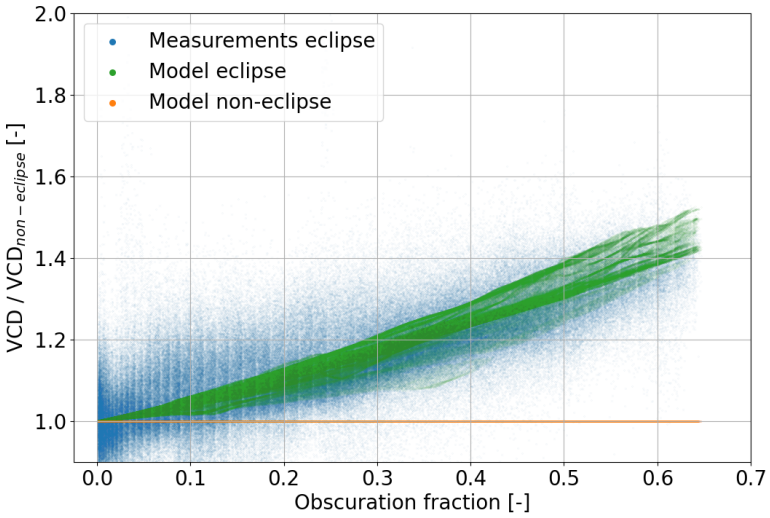


**Figure 5.10:** The increase in $NO_2$ as a ratio of modelled non-eclipse $NO_2$ values versus obscuration fraction is plotted. The ratio is computed using the non-eclipse expected model values as the reference. Both measurements (in blue) and eclipse model concentrations (in green) of TROPOMI orbit 18955 are shown.

In Figure 5.10, the ratios of eclipse vertical column densities with respect to the non-eclipse vertical column density of the TM5 model are shown. VCD of both the adjusted eclipse measurements and the modelled eclipse concentrations are compared to the non-eclipse values here. With the use of the ratio, all non-eclipse effects are filtered out and consequently, the increasing ratio as seen in Figure 5.10 represents the effects of the solar eclipse. In comparison to the ratio of the non-eclipse model, which is constant along the range of obscuration fractions, both the measurements and eclipse model concentrations increase with a similar ratio as the obscuration fraction increases. To specifically quantify this increase per obscuration fraction, Figure 5.11 shows the mean ratio and trend line of the datasets.

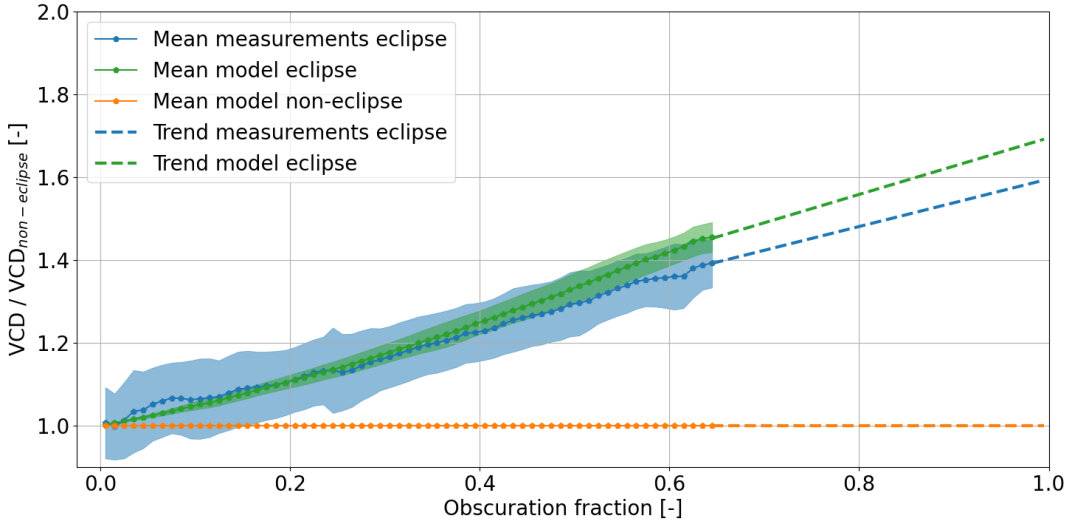


**Figure 5.11:** The increase in $NO_2$ as a mean ratio of modelled non-eclipse $NO_2$ values versus obscuration fraction is plotted. The ratios shown are the measurements (in blue) and the eclipse model concentrations (in green) of TROPOMI orbit 18955, with their corresponding trendlines. The mean of the ratios are calculated based on bins of obscuration fractions of size 0.01.

In general, there exists a eminent agreement in the mean ratios observed, revealing a marked increase in $NO_2$ levels when compared against model-derived ratios that exclude anticipated eclipse effects. Both sets of ratios exhibit a linear trend, demonstrating a close alignment evident for example at an obscuration fraction of 0.6, where the computed ratio for both measured and modelled concentrations approximates to 1.4. The trendlines shown in Figure 5.11 project the linear trend observed in the initial

phase where concentrations were measurable during the periods of experienced obscuration. Extrapolation of these trendlines suggests a potential ratio of 1.6$\pm$0.07 for measurements and approximately 1.7$\pm$0.04 for modelled data. These findings demonstrate strong agreement with prior observations from Adams et al. (2010) through measurement and modelling. This investigation signifies the ability to detect the enlargement of $NO_2$ attributable to a solar eclipse across expansive spatial regions using space-based measurements. In summary, the measurements conclusively illustrate an increase in atmospheric $NO_2$ levels during a solar eclipse, while the modelled eclipse-projected concentrations establish a connection to the short-term sensitivity of $NO_2$ to changing solar irradiance.

## 5.3. $NO_2$ modelling vs. measurements: Solar eclipse 25 October 2022

Here, a similar approach and figures will be shown as in Section 5.2. This solar eclipse case will serve as extra proof for the case treated there. Therefore a concise analysis will be given concerning the similarities in analysis results. Nonetheless, substantial additions will be elaborated in-depth as this solar eclipse case is not less significant. First, the figures in Figure 5.12 will consist of the adjusted measurements from TROPOMI, the non-eclipse- and eclipse TM5 model values from the TROPOMI orbit 26077 on 25 October 2022.

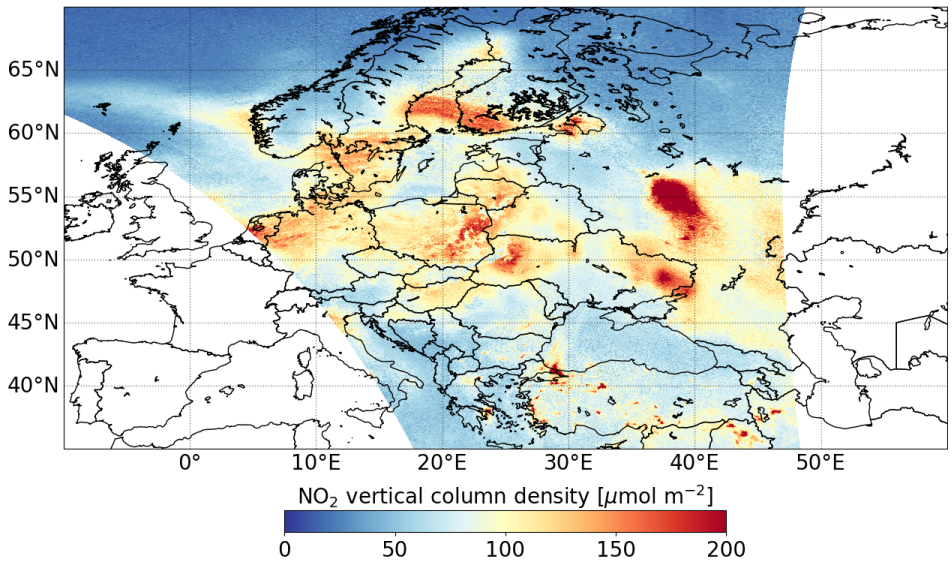


**(a)** Adjusted $NO_2$ concentration measurements.

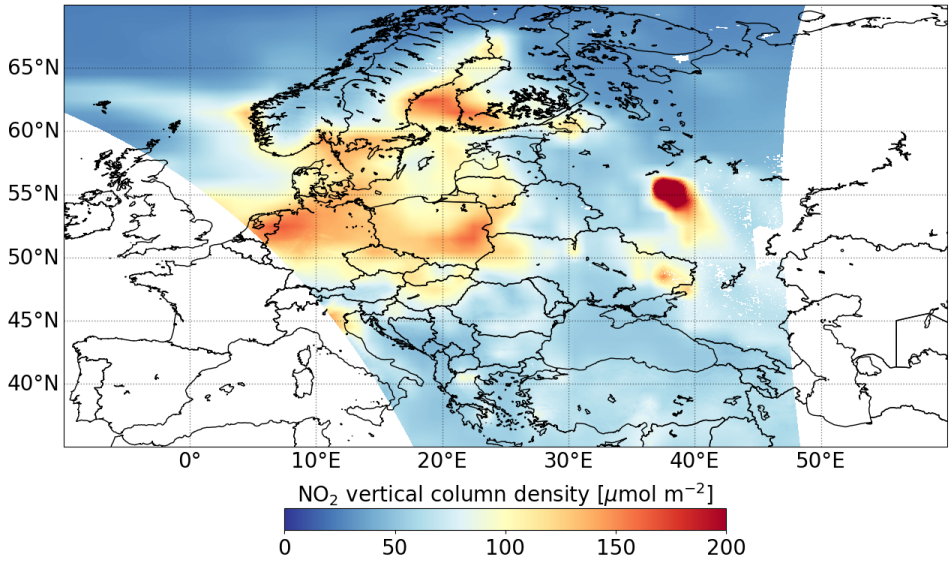


**(b)** Expected non-eclipse $NO_2$ concentrations by TM5.

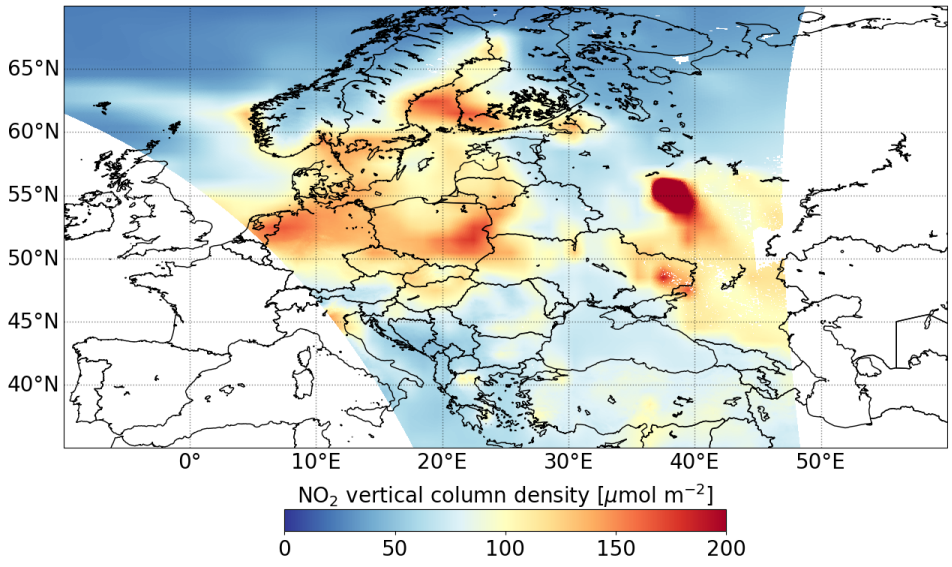


**(c)** Expected eclipse $NO_2$ concentrations by TM5.

**Figure 5.12:** Comparison of measurements and model $NO_2$ concentrations of TROPOMI orbit 26077.

In comparison to the solar eclipse covered in Section 5.2, here higher concentrations of $NO_2$ are seen in spatially larger areas. Moscow here still shows up as a big individual source of $NO_2$, while above Western Europe, Sweden and Finland more widespread areas of emission are present in Figure 5.12c. This is similarly concluded from the $NO_2$ concentrations originating from the adjusted retrieval algorithm in Figure 5.12a. The transition from non-eclipse $NO_2$ concentrations in Figure 5.12b to the eclipse $NO_2$ concentrations in Figure 5.12c is mainly represented by an increase in $NO_2$ east of 30° E. From Figure 5.4 this increase can be related to the obscuration fraction being higher than 0.3 and specifically increasing around the 50° latitude. In Figure 5.12b no striking solar eclipse effects are visualised, but increases in $NO_2$ seen over Western Europe and east of Moscow and Ukraine are the result of predicted surface emissions. From the visual comparison, it can be said that the expected eclipse $NO_2$ concentrations in Figure 5.12c match the measurements in Figure 5.12a better than the non-eclipse values do from Figure 5.12b. The computed differences between the two modelled datasets and the measurements are presented in Figure 5.13, where the agreement between measurements and model simulations will become evident.

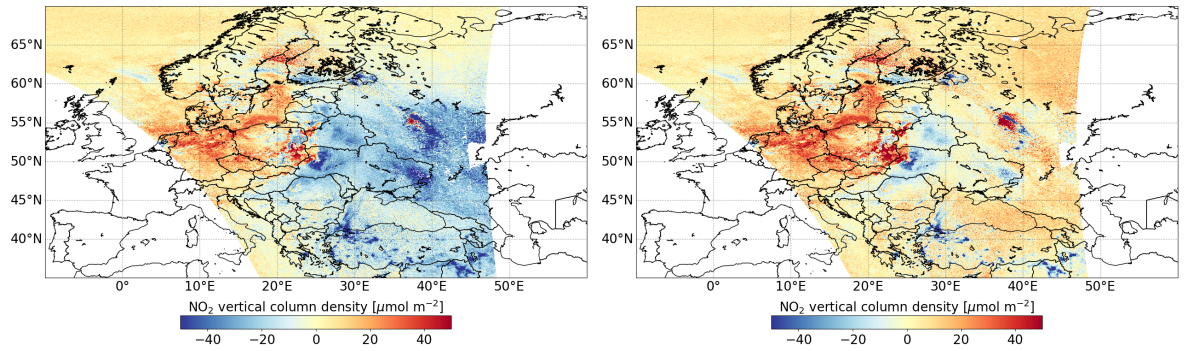


**(a)** Difference between measurements and expected non-eclipse $NO_2$.

**(b)** Difference between measurements and expected eclipse $NO_2$.

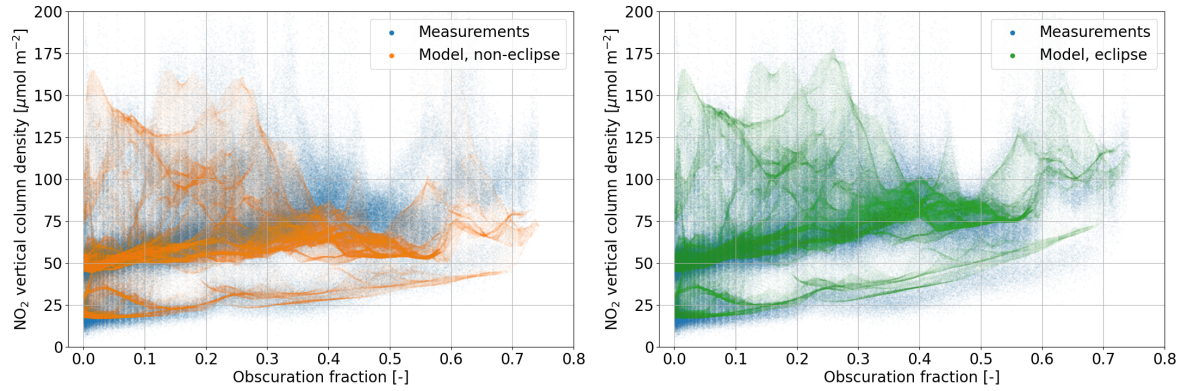


**(c)** Absolute $NO_2$ concentrations of the measurements and expected non-eclipse versus obscuration fraction.

**(d)** Absolute $NO_2$ concentrations of the measurements and expected eclipse versus obscuration fraction.

**Figure 5.13:** Differences (in **(a)** and **(b)**) between the $NO_2$ concentrations (in **(c)** and **(d)**) of the measurements and TM5 model values for both non-eclipse and eclipse expectations of TROPOMI orbit 26077. The differences in **(a)** and **(b)** are calculated by $VCD_{model}$ - $VCD_{measurements}$.

Figure 5.13a shows the major differences which are present between the measurements and the expected non-eclipse $NO_2$ concentrations. The blue region east of 25° E indicates that the model values are underestimated compared to the measurements. This region corresponds to where the solar eclipse has its most influence in terms of (partial) shadow. In comparison to the modelled expected eclipse $NO_2$ concentrations, the differences in Figure 5.13b show an improvement as the majority of the negative differences have disappeared and are closer to zero. For pixels with an obscuration fraction above 0.3, the expected eclipse model values proof to be accurate when compared to the measurements. Pixels with an obscuration fraction lower than 0.3, unfortunately, suffer from high emission effects, as seen in Figure 5.13c and Figure 5.13d. Various concentrated and high signatures of $NO_2$ concentrations are present. Similarly, Figure 5.13a and Figure 5.13b, show big differences above Western Europe. Neither of the datasets computed through the TM5 chemistry model were able to

accurately model the $NO_2$ concentrations as measured by TROPOMI.

### Difficulty of regional emissions

Several concepts can be addressed to explain the overestimation of $NO_2$ in the TM5 model above Western Europe. The areas where the overestimation of $NO_2$ occurs are Germany, Poland, Sweden and in particular Helsinki. After the eclipse implementation is applied, these areas still show significant differences. First, visual inspection of the figures in Figure 5.12 indicates that the measurements can contain sharp boundaries in terms of concentration between ground pixels, while the modelled concentrations show a more gradual transition between low and high concentrations. As addressed in Subsection 2.2.3, the TM5 model values are computed on a grid of one by one degree, while it was evident from Subsection 2.2.1 that the TROPOMI ground pixels are 5.5 km by 3.5 km. In principle, this is a considerable mismatch between the two datasets but the TM5 model values are regridded to match the spatial resolution of the TROPOMI measurements, which is done through weighted linear interpolation based on the nearest four neighbours TM5 pixels (Van Geffen et al., 2021). The weighted interpolation could be the cause of introducing too high $NO_2$ values above areas where low concentrations would be expected. The sharp boundary between land and water is for example well visualised in terms of $NO_2$ concentration measurements above the Baltic Sea at 57.5° N and 20° E in Figure 5.12a, while the modelled values in Figure 5.12c show $NO_2$ creeping to the atmosphere above the water as a result from the surrounding high emission sources. Consequently, large differences are seen in the same area in Figure 5.13a and Figure 5.13b.

Secondly, an overestimation of $NO_2$ could be related to the wrong emissions prediction. Unlike, for example, the input of estimated meteorological data, the actual emission of $NO_2$ by its anthropogenic sources may contain significant errors. Therefore, the possibility arises that emissions estimations were too high in the original TM5 model profiles, which propagate through in both the non-eclipse and eclipse model expectations of the $NO_2$ concentrations.

A quantitative analysis is shown in Figure 5.14 where the differences in $NO_2$ concentration versus the obscuration fraction are plotted.

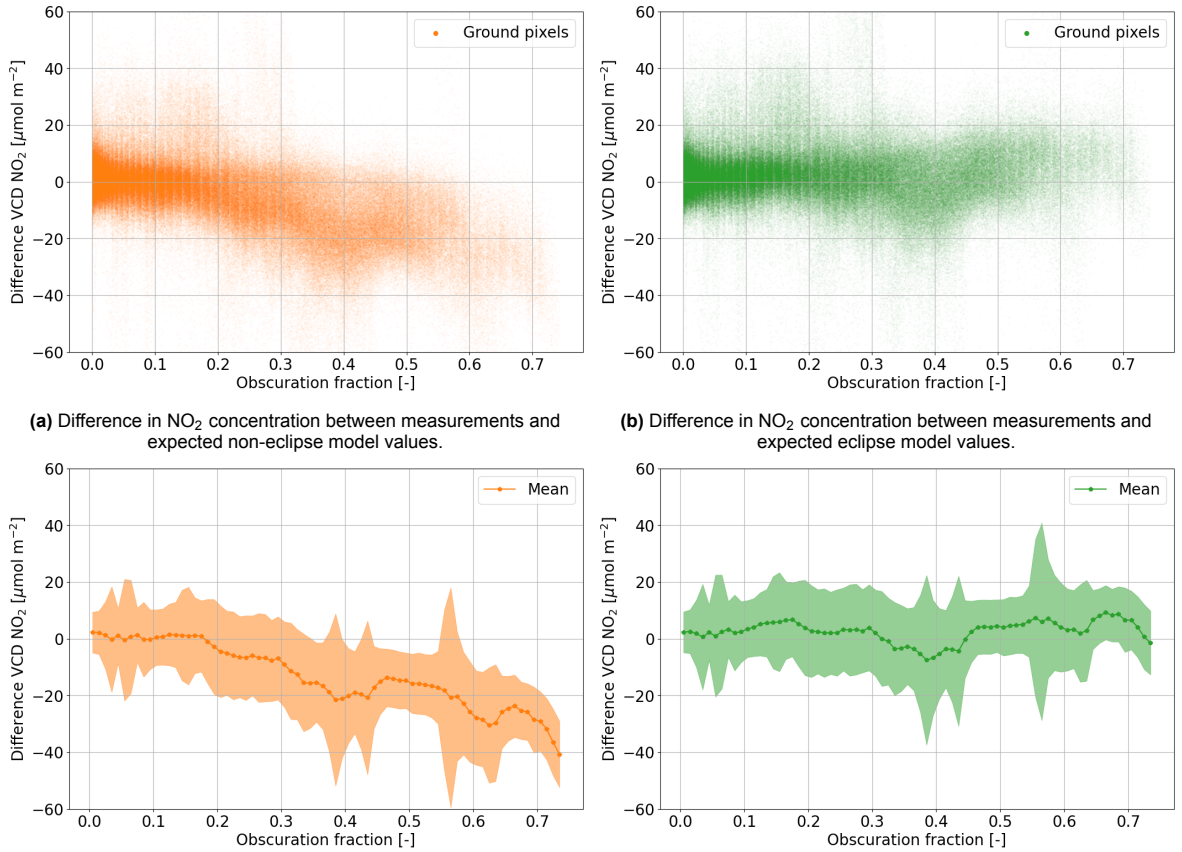


**(a)** Difference in $NO_2$ concentration between measurements and expected non-eclipse model values.

**(b)** Difference in $NO_2$ concentration between measurements and expected eclipse model values.

**(c)** Mean of the differences as presented above.

**(d)** Mean of the differences as presented above.

**Figure 5.14:** Absolute differences in $NO_2$ concentrations between measurements and TM5 model values versus obscuration fraction for both non-eclipse (**a**) and eclipse (**b**) expectations of TROPOMI orbit 26077. The differences are calculated by $VCD_{model}$ - $VCD_{measurements}$. The mean of the differences (in **(c)** and **(d)**) are calculated based on bins of obscuration fractions of size 0.01.

Directly apparent from the figures in Figure 5.14 is the increased uncertainty range of the mean values for specific obscuration fractions showing up as peaks. The in-depth analysis concluded that the several peaks in the uncertainty range highlight the specific areas of high $NO_2$ emissions. With the higher emissions, a clear solar eclipse effect is impeded by the variable concentrations of $NO_2$ in the atmosphere. In Figure 5.14c this is encountered for the pixels experiencing an obscuration fraction up to 0.2, where the mean difference is calculated to be zero. Nonetheless, a clear overall difference can still seen between the measurements and the model values for the non-eclipse expectation for high obscuration fractions, while the expected eclipse $NO_2$ values show a good agreement for all obscuration fractions. This proves that the eclipse implementation as used is a good representation of the influence of the solar eclipse on the $NO_2$ concentrations in the atmosphere. Therefore, the negative differences as presented in Figure 5.13c can be interpreted as the increase of $NO_2$ during a solar eclipse as well. The general trend of the mean is described by an increase of $NO_2$ as the obscuration fraction increases, which translates to an increase of $NO_2$ as the incoming sunlight decreases.

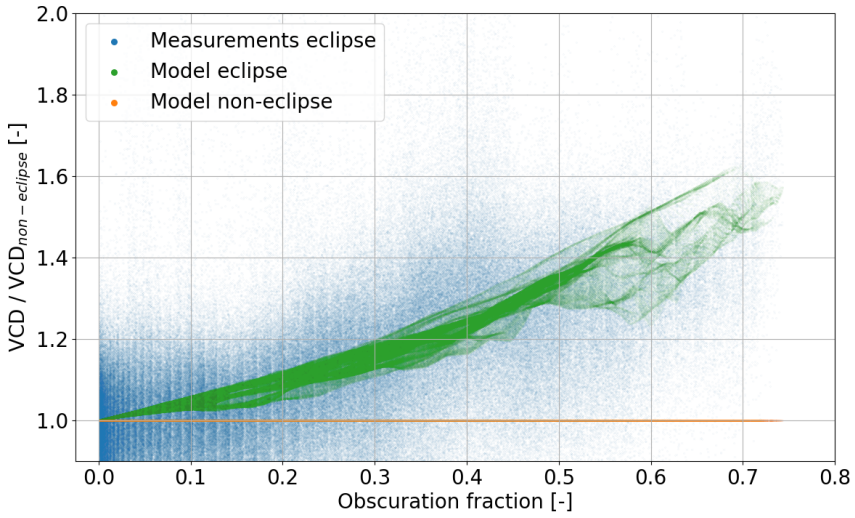


**Figure 5.15:** The increase in $NO_2$ as a ratio of modelled non-eclipse $NO_2$ values versus obscuration fraction is plotted. The ratio is computed using the non-eclipse expected model values as the reference. Both measurements (in blue) and eclipse model concentrations (in green) of TROPOMI orbit 26077 are shown.

Figure 5.15 shows a more coherent agreement between the measurements and the eclipse model concentrations in terms of $NO_2$ increase than the results presented in Figure 5.13c and Figure 5.14c. The various high peaks are now eliminated as the measurements are divided by the non-eclipse expected values, subsequently only showing solar eclipse effects. A broadly dispersed set of ground pixels is still presented but in comparison to the non-eclipse model ratio, the measurements do indicate the increase of $NO_2$ as ratios higher than 1.0 are shown. Moreover, the measurements ratios do share a similar upward trend compared to the modelled ratios, despite the higher uncertainty concerning the spread for different obscuration fractions. The mean ratio of both the measurements and the modelled concentrations including their linear trendlines are shown in Figure 5.16:

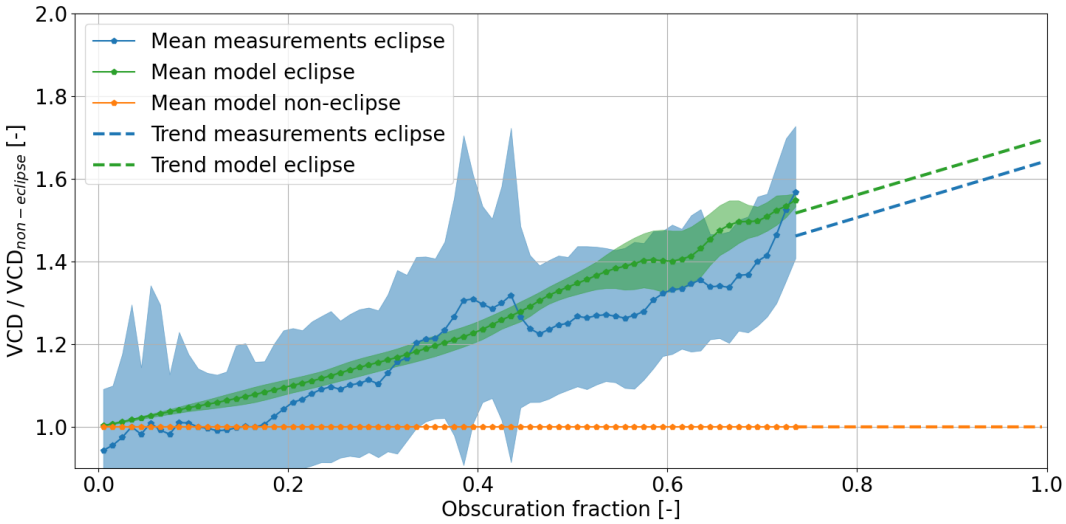


**Figure 5.16:** The increase in $NO_2$ as a mean ratio of modelled non-eclipse $NO_2$ values versus obscuration fraction is plotted. The ratios shown are the measurements (in blue) and the eclipse model concentrations (in green) of TROPOMI orbit 26077, with their corresponding trendlines. The mean of the ratios are calculated based on bins of obscuration fractions of size 0.01.

Notably in the analysis presented in Figure 5.16 is a distinctive discrepancy in the levels of uncertainty between the mean measurement ratio and the computed mean derived from modelled eclipse concentrations. This divergence is reflected in their respective confidence intervals, where the measurement-derived mean ratio exhibits a higher uncertainty compared to the model-based computation, characterised by its narrower confidence regions, thereby indicating a higher level of precision. However,

despite this apparent difference in uncertainty, a compelling agreement is seen between the computed means of the ratios from both measurement and modelled concentrations. The extrapolated trendlines show potential ratios of $1.65 \pm 0.13$ for the measurements and $1.7 \pm 0.04$ for the modelled data for an obscuration fraction of 1. It's noteworthy that while the ratio derived from modelled eclipse concentrations follows an almost linear increase, the measurement-based ratio displays deviations from the anticipated linear trend as the obscuration fraction increases. This divergence, however, does not negate the underlying similarity in the linear trends observed in both ratios, primarily in terms of their magnitude, wherein the primary discrepancy lies in the initial means of the ratios. Importantly, both ratios, in contrast to the constant ratio of the non-eclipse model, demonstrate a substantial increase, suggesting a clear relation between the influence of a solar eclipse and the increase of $NO_2$ concentrations within the atmosphere. These findings strengthen the premise of a robust relationship between solar eclipse events and increased $NO_2$ concentrations, showcasing the capacity of space-based measurements conducted by instruments such as TROPOMI. These results have shown that large-scale measurements are able to effectively capture and delineate the anticipated rise in $NO_2$ concentrations, as predicted by the model's sensitivity to $NO_2$ dynamics within the atmosphere in response to the sunlight-intercepting occurrence of a solar eclipse.

# 6

# Conclusion

This research aimed to evaluate the sensitivity of $NO_2$ in the Earth's atmosphere as a response to the influence of a solar eclipse. To do this, TROPOMI $NO_2$ measurements were used during the solar eclipses on 10 June 2021 and 25 October 2022.

The original measurements during these solar eclipses showed disturbed values, indicating the suspicion of an incorrect retrieval. The pixels inside the shadow of the solar eclipse showed slant column uncertainties exceeding 50 $\mu$mol $m^{-2}$. From the TROPOMI algorithm, these pixels showed errors related to outliers within the wavelength spectra computed with DOAS. The wavelength spectra of the residuals indeed showed influences from the solar eclipses, through the decrease and increase of the contribution of the Balmer lines for different obscuration fractions. A method was designed to correct the $NO_2$ measurements for the biases induced by the solar eclipse. The computed obscuration fractions were applied in the radiance correction and subsequently shifting the wavelength window within the DOAS retrieval made the influence of the Balmer lines disappear. We verified the new method using a test orbit during a day without a solar eclipse. After applying the new $NO_2$ retrieval method, a qualitative inspection of the results still concluded elevated $NO_2$ concentrations in the solar eclipse region. This suggested that the increased $NO_2$ measured by TROPOMI during the solar eclipse was real and not artificially introduced by the algorithm. It shows that, after the adjustment, the TROPOMI algorithm is still able to correctly measure $NO_2$ concentrations with unfavourable light conditions.

To understand the actual increase of $NO_2$ in the atmosphere, we modelled the expected $NO_2$ increase during a solar eclipse by adjusting the $NO_2$ columns of the TM5 atmospheric chemistry model on the TROPOMI grid. Since the TM5 model is not aware of the solar eclipse event, the originally modelled prediction presents the non-eclipse values for the orbits of interest. The comparison between the adjusted $NO_2$ measurements and the modelled non-eclipse values for the solar eclipse on 10 June 2021 showed a negative linear trend where differences of 30 $\mu$mol $m^{-2}$ for an obscuration fraction of 0.6 occurred. This shows both datasets' disagreement and the underestimation of the model values. Therefore, with the eclipse implementation, through the use of equilibrium equations, the predicted eclipse values were computed. An improvement of the model values is evident as the differences are now minimised to 5 $\mu$mol $m^{-2}$ at an obscuration fraction of 0.6.

With the agreement of the adjusted $NO_2$ measurements and the eclipse implemented model values, the behaviour of $NO_2$ in Earth's atmosphere is defined through their comparison. It was demonstrated that the linear photodissociation proved to be accurate for short-term changes in the $NO_2$ concentrations. The linear behaviour was confirmed by the increases seen for both solar eclipse cases on 10 June 2021 and 25 October 2022. Both cases showed linear trends in the increasing ratios of vertical column density of both the measurements and the model. These ratios were found to be $1.6 \pm 0.12$ and $1.7 \pm 0.07$, respectively, compared to the non-eclipse values for ground pixels experiencing obscuration fractions up to 1. The ratios computed using this extensive dataset of $NO_2$ concentrations influenced by a solar eclipse strengthens the relation between the reduction of sunlight and the increase of $NO_2$.

In conclusion, we have shown the first space-based observational evidence and quantification of large-scale $NO_2$ concentration increases during solar eclipses. Moreover, the adjusted retrieval is now able to correctly obtain $NO_2$ concentrations in the atmosphere during solar eclipses. The increase in $NO_2$ concentrations during a solar eclipse as measured from space by TROPOMI is apparent over a substantial area and has proven to be a result of the decreased amount of sunlight. Those corrected measurements can be used to test and further improve atmospheric chemistry models to compensate for variations of solar radiation other than the diurnal cycle.

# 7

# Recommendations & Outlook

## 7.1. Recommendations

### 7.1.1. Pseudo absorber Balmer lines correction

Instead of changing the wavelength window to deal with the influence of the Balmer lines, another approach could have been chosen to adjust the $NO_2$ retrieval. Within the DOAS fitting algorithm, the possibility exists to include Pseudo absorbers. These absorbers can represent a signal which otherwise disturbs the fitting algorithm as it has difficulties trying to relate it to the other fitting parameters. The advantage of this approach would be that the original wavelength window can still be used, from which more information is gathered as this is a bigger window. Additional computations, however, have to be made to model the effect of the Balmer lines during a solar eclipse. As this effect is highly variable with the constantly changing observed obscuration fraction this could be a complicated task. However, the benefit of having to model the effect of the Balmer lines is the resulting understanding of the behaviour of these Balmer lines and the underlying physics.

Care has to be taken for additional constraints within the original wavelength window during a solar eclipse. The Ring effect for example needs to be corrected as well, as its effect is embedded into the spectral structures of the Balmer lines. The computation of the Ring effect, however, is based on the reference reflectance spectrum of the Sun. To correctly adjust the Ring effect, the reference spectrum of the Sun during a solar eclipse would be of help. At the moment, this is not present and is also not possible as the irradiance measured by TROPOMI is not influenced by the interaction with the Moon.

### 7.1.2. Full chemistry model including solar eclipse

A more direct approach to specifically only study the sensitivity of $NO_2$ to the short-term variations of sunlight in the atmosphere would be to incorporate a solar eclipse feature into the complete TM5 atmospheric chemistry model. Within the model, a certain amount of sunlight could be set to change during a certain period to take place in the middle of the day. The measurements retrieved through the research as described in this thesis can be used to form the basis of the full chemistry model and can subsequently be used as validation for its results. As the measurements accurately present the resulting concentration of $NO_2$ in the atmosphere, the model will then be able to present the specific changes as a response to the influence of the solar eclipse. The benefit of using a full chemistry model is that other components that are coupled to the $NO_2$ concentrations and gasses that have similar photochemical dependencies are now also taken into the equation. That way, a more complete analysis of the photochemical behaviour of $NO_2$, and other gasses, could be made, under the assumption that the model can compute a representative simulation of the dynamics concerning a solar eclipse and the response of the atmospheric composition.

In principle, this research has shown that indeed the measurements can be used as a validation to model values. The simplified model in this research, accomplished through the incorporated assumptions made by Adams et al. (2010), has shown the short-term dependency of $NO_2$ to sunlight. Though, over big cities with high pollution of $NO_2$, this simplified model could not yet perform accurately, but a

more complete model analysis could improve this in addition to the long-term expectancy concerning the photochemical equilibrium of $NO_2$.

### 7.1.3. Temporal resolution

The foundation of measuring the atmosphere with TROPOMI is based on the fact that it can scan the entire Earth within one day. This means that daily measurements are provided across the entire surface of the Earth, but atmospheric dynamics that act on shorter timescales are not able to be mapped and analysed. A satellite that would be able to measure at a higher temporal resolution would be valuable to create a better understanding of the dynamics of $NO_2$ during a solar eclipse. Wu et al. (2011) also found with the use of chemical box model simulations that the increase during the progression of the solar eclipse and the decrease after the eclipse maximum were not symmetrical. With the use of geostationary satellites that can measure $NO_2$ from space with a higher temporal resolution, a better time series of measurements could be gathered. The time series of $NO_2$ measurements during a solar eclipse can consequently be used to more precisely analyse $NO_2$'s behaviour and sensitivity to sunlight. Geostationary satellites like GEMS (Kim et al., 2020), TEMPO (Zoogman et al., 2017) and MTG (Holmlund et al., 2021) can form the basis for this analysis in the future for the continents of Asia, North America and Europe, respectively.

### 7.1.4. Ozone during a solar eclipse

Alongside the several studies, of e.g. Adams et al. (2010) and Gil et al. (2000), regarding the change of $NO_2$ in the atmosphere during a solar eclipse, the influence on the ozone ($O_3$) concentration was also studied. It is believed that the photochemical dependency of $O_3$ is also influenced during a solar eclipse, as the photolysis reaction of $O_3 + h\upsilon \Rightarrow O + O_2$ happens in the UV wavelength region of 290-330 nm. Contrary to the conclusions drawn from the research into $NO_2$ and its response to a solar eclipse, none of the studies could, with similar confidence, confirm the response of $O_3$ using ground-based measurements. Applying a similar method as used in this research, using a large-scale dataset of spaceborne $O_3$ measurements during a solar eclipse, could help to clarify the hypothesis around the effect of a reduction in incoming sunlight to $O_3$. Despite the short-term influences by the solar eclipse, the extensive amount of data over a large area can highlight spatial signatures not earlier detected during research into changing $O_3$ concentrations in the atmosphere during a solar eclipse. The extent of the fitting window has to be studied specifically related to the $O_3$ absorption spectrum and has to be adjusted for possible high-spectral-resolution features caused by the solar eclipse.

### 7.1.5. Analysis of other variables affecting the $NO_2$ concentrations influenced by the solar eclipse

An advantage of spaceborne measurements is the ability to analyse dependencies on a large scale, i.e., at multiple locations simultaneously. With the adjustment of the $NO_2$ retrieval to correctly present the $NO_2$ concentration for every pixel, as a result, there is now an existing dataset of large-scale $NO_2$ concentrations influenced by a solar eclipse. This dataset can be used for further analysis of various variables and their effect on the $NO_2$ concentration while these variables are also affected by the solar eclipse. Typical variables such as cloud fraction, latitude, anthropogenic inputs and surface height could be chosen for a more in-depth analysis to find possible relations between them and the reduction in light with a corresponding response to the $NO_2$ concentration. This would improve the understanding of how a reduction in incoming sunlight would influence the $NO_2$ concentrations in a variety of different scenarios globally.

## 7.2. Outlook

### 7.2.1. Relevance for geoengineering

This research has shown that the equilibrium between $NO_2$ and NO in the atmosphere is sensitive to a fast reduction in sunlight. In comparison to orbits before and after the solar eclipse orbit, a high increase of $NO_2$ was measured and experienced in the shadow of the Moon. In this partial shadow of the Moon, starting from obscuration fractions equal to zero, the increase of $NO_2$ concentration can be observed for the smallest obscuration fractions along a clear positive trend. Solar geoengineering concepts will most likely also work with small obscuration fractions, which can possibly change over time. These

concepts present themselves as sunshades in space and stratospheric aerosol injection to manage the incoming solar radiation (Lenton and Vaughan, 2009). The small obscuration fractions as observed in our research could similarly be seen during the appliance of the solar geoengineering concepts. The atmospheric response of sunlight-engineering approaches must therefore be model-simulated accordingly to investigate their influence. It was found that atmospheric response of this nature, caused by events which influence the amount of solar radiation received on Earth, may not yet be well simulated in some existing atmospheric chemistry- and climate models (Driscoll et al., 2012; Charlton-Perez et al., 2013). Only considering the disturbance of the $NO_2$-NO equilibrium (through the increase of $NO_2$) for now, means that in both the troposphere and the stratosphere a $NO_2$ increase leads to negative effects. Not only do $NO_2$ and NO itself cause health problems due to their air-polluting properties (World Health Organization, 2003), but as a consequence of the $NO_2$ increase, also ozone ($O_3$) increases in the troposphere where it is the origin of the well-known smog in big cities (Sillman, 2003). For the stratosphere, the $NO_2$ increase has a contrary effect on $O_3$ as it acts as a catalyser for the destruction of ozone (see Subsection 2.1.3). However, for the stratosphere, this is not beneficial as the ozone present in the stratosphere protects us from UV radiation. Both these effects in the troposphere and stratosphere therefore do not show positive influences but do already occur at low obscuration fractions.

Due to the relatively short duration of the solar eclipses, no long-lasting effects of $NO_x$ were experienced in terms of, for example, bad air quality, as its short-term response to the recovery to normal sunlight conditions consequently meant a recovery of the $NO_2$ and NO balance as well. Where a solar eclipse is a dynamic event which will only last for a couple of hours per year, climate engineering approaches involving solar radiation management lead to situations where a portion of the sunlight is blocked for long-term periods. The long-term nature of these approaches brings a new dimension to the proposed complex engineering solutions, concerning the changing climate within the Earth-Atmosphere environment. As addressed before, ozone for example is known to be affected by the change in $NO_2$ concentration. Still, due to the short-term processes during a solar eclipse, the resulting influence on the $O_3$ concentration is difficult to study. Additionally, the photolysis of $O_3$ (Matsumi and Kawasaki, 2003) would also be a point of interest when long-term periods of obscuration are caused by sunlight-intercepting geoengineering approaches. The long-term effects therefore need to be treated carefully with great attention. Solar geoengineering may settle a new $NO_2$-NO equilibrium, which should be a point of attention when predicting the consequences of solar geoengineering. An all-encompassing understanding of the atmosphere, its composition and the effects of initiating changes to them should be achieved before we invest in changes to the interaction between the Earth and atmosphere that cause long-term effects.

### 7.2.2. Relevance for cloud shadows

A more common phenomenon creating a shadow in the atmosphere and onto the Earth's surface is a cloud. Applying the principle from this research similarly in a theoretical manner to the cloud shadows, one could argue that the reduction in sunlight underneath a cloud will result in an increase of $NO_2$ as well. However, the different kinds of shadows need to be considered here. The partial shadow on the Earth's surface created by the Moon during a solar eclipse differs significantly from the shadow caused by clouds. During a solar eclipse, 50% of the incoming sunlight could be blocked by the Moon, but this is not similar to a cloud letting through only 50% of the sunlight. In the shadow of a cloud, we are dealing with a shadow that would be equivalent to an umbra shadow when dealing with solar eclipses. The umbra usually takes in less than 1% of space of the entire lunar shadow, which we did not analyse in this research. Here, the shadow does not receive any direct sunlight as the Sun's disk is completely covered by the Moon. In the scenario of a cloud, this is similar, but in addition, the cloud does disperse a portion of the light that is received at the top downwards to the Earth's surface. Therefore, a relation between the obscuration (in terms of the reduction of direct sunlight) induced by a cloud and the obscuration experienced during a solar eclipse is incomparable.

Still, this research has shown that we can measure the concentration of atmospheric constituents while experiencing reduced light conditions. Extending the knowledge gained from this research could help to enhance our understanding of atmospheric composition changes in the shadows of clouds. The challenge associated with this concept is the major difference concerning the principle of light paths. In fact, a shadow underneath a cloud can be seen as a total obscuration, but still receiving light through

the cloud means the way the light behaves is completely different. This has a major effect on our computation from slant column densities to vertical column densities as the air mass factor diverges from what we are used to during the solar eclipse scenario. The challenging part of this problem is that the computation of the air mass factor needs to be very specific to be able to accurately determine any changing $NO_2$ concentrations in the shadow of a cloud. To achieve this accurate computation of the air mass factor, highly detailed information about the considered clouds would be necessary to ensure a reliable retrieval of the $NO_2$ concentrations due to the small-scale variability of clouds. So far, this information does not seem to be available to be applied to such satellite-based approaches.

Another factor which needs to be considered is the appliance of the actinic flux. The actinic flux describes the distribution of solar irradiance in all directions and consequently does not necessarily depend on direct sunlight but is also considered when dealing with diffuse light. It has been found that the application of the actinic flux is of importance when photodissociation is governed by the presence of clouds. Madronich (1987) found that photodissociation rates inside clouds can exceed the rates found for clear-sky values. This is contrary to the theoretical principle of having lower photodissociation rates due to reduced sunlight as we have seen for the solar eclipse scenarios. The coupling between these two concepts can provide us with interesting knowledge on the behaviour of $NO_2$ in the shadow of clouds.

Overall, the research into the $NO_2$ concentrations in the shadow of clouds would be very interesting to conduct. Its results would contribute to the understanding of Earth-atmosphere interaction influenced by solar geoengineering effects. However, challenging aspects related to the complex computation of the air mass factor including small-scale variability of clouds will need to be tackled, not to mention the possibility of changing cloud properties induced by the reduction of incoming sunlight. The impact of cloud shadows on the $NO_2$ concentrations in the atmosphere is in that respect significantly more complicated in terms of atmospheric properties and geometry compared to the impact of solar eclipses on the $NO_2$ concentrations in the atmosphere.

# Bibliography


Adams, C., McLinden, C. A., Strong, K., and Umlenski, V. (2010). Ozone and $NO_2$ variations measured during the 1 August 2008 solar eclipse above Eureka, Canada with a UV-visible spectrometer. *Journal of Geophysical Research: Atmospheres*, 115(D19):D19310.

Anderson, J. (1999). Meteorological changes during a solar eclipse. *Weather*, 54(7):207–215.

Bernhard, G. and Petkov, B. (2019). Measurements of spectral irradiance during the solar eclipse of 21 August 2017: reassessment of the effect of solar limb darkening and of changes in total ozone. *Atmospheric Chemistry and Physics*, 19(7):4703–4719.

Chance, K. and Kurucz, R. L. (2010). An improved high-resolution solar reference spectrum for earth's atmosphere measurements in the ultraviolet, visible, and near infrared. *Journal of quantitative spectroscopy and radiative transfer*, 111(9):1289–1295.

Chance, K. V. and Spurr, R. J. (1997). Ring effect studies: Rayleigh scattering, including molecular parameters for rotational Raman scattering, and the Fraunhofer spectrum. *Applied optics*, 36(21):5224–5230.

Charlton-Perez, A. J., Baldwin, M. P., Birner, T., Black, R. X., Butler, A. H., Calvo, N., Davis, N. A., Gerber, E. P., Gillett, N., Hardiman, S., et al. (2013). On the lack of stratospheric dynamical variability in low-top versions of the CMIP5 models. *Journal of Geophysical Research: Atmospheres*, 118(6):2494–2505.

Chimot, J., Vlemmix, T., Veefkind, J. P., De Haan, J. F., and Levelt, P. F. (2016). Impact of aerosols on the OMI tropospheric $NO_2$ retrievals over industrialized regions: how accurate is the aerosol correction of cloud-free scenes via a simple cloud model? *Atmospheric Measurement Techniques*, 9(2):359–382.

Chitta, L. P., Smitha, H. N., and Solanki, S. K. (2020). *Solar Photosphere, Oxford Research Encyclopedia of Physics*. Oxford University Press Oxford.

Crutzen, P. J. (1979). The role of NO and NO2 in the chemistry of the troposphere and stratosphere. *Annual review of earth and planetary sciences*, 7(1):443–472.

Dessler, A. (2000). *Chemistry and Physics of Stratospheric Ozone*. ISSN. Elsevier Science.

Driscoll, S., Bozzo, A., Gray, L. J., Robock, A., and Stenchikov, G. (2012). Coupled Model Intercomparison Project 5 (CMIP5) simulations of climate following volcanic eruptions. *Journal of Geophysical Research: Atmospheres*, 117(D17).

Emde, C. and Mayer, B. (2007). Simulation of solar radiation during a total eclipse: a challenge for radiative transfer. *Atmospheric Chemistry and Physics*, 7(9):2259–2270.

Eskes, H. J., van Geffen, J. H. G. M., Boersma, K. F., Eichmann, K.-U., Apituley, A., Pedergnana, M., Sneep, M., Veefkind, J. P., and Loyola, D. (2022). *S5P/TROPOMI Level-2 Product User Manual Nitrogen Dioxide*. ESA, http://www.tropomi.eu/data-products/nitrogen-dioxide/, Report S5P-KNMI-L2-0021-MA, version 4.1.0 edition. (last access: 14 September 2023).

Espenak, F. (2016). *21st Century Canon of Solar Eclipses*.

Espenak, F. and Meeus, J. (2006). *Five millennium canon of solar eclipses:-1999 to+ 3000 (2000 BCE to 3000 CE)*. National Aeronautics and Space Flight Administration.

Fabian, P., Rappengluck, B., Stohl, A., Werner, H., Winterhalter, M., Schlager, H., Stock, P., Berresheim, H., Kaminski, U., Koepke, P., Reuder, J., and Birmili, W. (2001). Boundary layer photochemistry during a total solar eclipse. *Meteorologische Zeitschrift*, 10(3):187–192.

Gil, M., Puentedura, O., Yela, M., and Cuevas, E. (2000). Behavior of $NO_2$ and $O_3$ columns during the eclipse of February 26, 1998, as measured by visible spectroscopy. *Journal of Geophysical Research: Atmospheres*, 105(D3):3583–3593.

Holmlund, K., Grandell, J., Schmetz, J., Stuhlmann, R., Bojkov, B., Munro, R., Lekouara, M., Coppens, D., Viticchie, B., August, T., Theodore, B., Watts, P., Dobber, M., Fowler, G., Bojinski, S., Schmid, A., Salonen, K., Tjemkes, S., Aminou, D., and Blythe, P. (2021). Meteosat Third Generation (MTG): Continuation and innovation of observations from geostationary orbit. *Bulletin of the American Meteorological Society*, pages 1–71.

Huijnen, V., Williams, J., van Weele, M., van Noije, T., Krol, M., Dentener, F., Segers, A., Houweling, S., Peters, W., de Laat, J., Boersma, F., Bergamaschi, P., van Velthoven, P., Le Sager, P., Eskes, H., Alkemade, F., Scheele, R., Nédélec, P., and Pätz, H.-W. (2010). The global chemistry transport model TM5: description and evaluation of the tropospheric chemistry version 3.0. *Geoscientific Model Development*, 3(2):445–473.

Jacob, D. J. (1999). *Introduction to Atmospheric Chemistry*. Princeton University Press.

Kim, J., Jeong, U., Ahn, M.-H., Kim, J. H., Park, R. J., Lee, H., Song, C. H., Choi, Y.-S., Lee, K.-H., Yoo, J.-M., Jeong, M.-J., Park, S. K., Lee, K.-M., Song, C.-K., Kim, S.-W., Kim, Y. J., Kim, S.-W., Kim, M., Go, S., Liu, X., Chance, K., Miller, C. C., Al-Saadi, J., Veihelmann, B., Bhartia, P. K., Torres, O., Abad, G. G., Haffner, D. P., Ko, D. H., Lee, S. H., Woo, J.-H., Chong, H., Park, S. S., Nicks, D., Choi, W. J., Moon, K.-J., Cho, A., Yoon, J., kyun Kim, S., Hong, H., Lee, K., Lee, H., Lee, S., Choi, M., Veefkind, P., Levelt, P. F., Edwards, D. P., Kang, M., Eo, M., Bak, J., Baek, K., Kwon, H.-A., Yang, J., Park, J., Han, K. M., Kim, B.-R., Shin, H.-W., Choi, H., Lee, E., Chong, J., Cha, Y., Koo, J.-H., Irie, H., Hayashida, S., Kasai, Y., Kanaya, Y., Liu, C., Lin, J., Crawford, J. H., Carmichael, G. R., Newchurch, M. J., Lefer, B. L., Herman, J. R., Swap, R. J., Lau, A. K. H., Kurosu, T. P., Jaross, G., Ahlers, B., Dobber, M., McElroy, C. T., and Choi, Y. (2020). New era of air quality monitoring from space: Geostationary Environment Monitoring Spectrometer (GEMS). *Bulletin of the American Meteorological Society*, 101(1):E1–E22.

Koepke, P., Reuder, J., and Schween, J. (2001). Spectral variation of the solar radiation during an eclipse. *Meteorologische Zeitschrift*, 10(3):179–186.

Kramida, A. E. (2010). A critical compilation of experimental data on spectral lines and energy levels of hydrogen, deuterium, and tritium. *Atomic Data and Nuclear Data Tables*, 96(6):586–644.

Krol, M., Houweling, S., Bregman, B., Van den Broek, M., Segers, A., Van Velthoven, P., Peters, W., Dentener, F., and Bergamaschi, P. (2005). The two-way nested global chemistry-transport zoom model TM5: algorithm and applications. *Atmospheric Chemistry and Physics*, 5(2):417–432.

Lenton, T. M. and Vaughan, N. E. (2009). The radiative forcing potential of different climate geoengineering options. *Atmospheric Chemistry and Physics*, 9(15):5539–5561.

Liou, K. N. (2002). *An Introduction to Atmospheric Radiation*, volume 84. Elsevier.

Lorente, A., Folkert Boersma, K., Yu, H., Dörner, S., Hilboll, A., Richter, A., Liu, M., Lamsal, L. N., Barkley, M., De Smedt, I., Van Roozendael, M., Wang, Y., Wagner, T., Beirle, S., Lin, J.-T., Krotkov, N., Stammes, P., Wang, P., Eskes, H. J., and Krol, M. (2017). Structural uncertainty in air mass factor calculation for $NO_2$ and HCHO satellite retrievals. *Atmospheric Measurement Techniques*, 10(3):759–782.

Madronich, S. (1987). Photodissociation in the atmosphere: 1. actinic flux and the effects of ground reflections and clouds. *Journal of Geophysical Research: Atmospheres*, 92(D8):9740–9752.

Matsumi, Y. and Kawasaki, M. (2003). Photolysis of atmospheric ozone in the ultraviolet region. *Chemical reviews*, 103(12):4767–4782.

Meeus, J. (1989). Elements of solar eclipses, 1951-2200. *Willman-Bell Inc., Virginia*.

Moon, B., Jeong, D.-G., Oh, S., and Sohn, J. (2017). Variation in solar limb darkening coefficient estimated from solar images taken by soho and sdo. *Journal of Astronomy and Space Sciences*, 34(2):99–103.

Ockenfuß, P., Emde, C., Mayer, B., and Bernhard, G. (2020). Accurate 3-D radiative transfer simulation of spectral solar irradiance during the total solar eclipse of 21 August 2017. *Atmospheric Chemistry and Physics*, 20(4):1961–1976.

Phillips, K. J. H. (1995). *Guide to the Sun*. Cambridge University Press.

Pierce, A. K. and Slaughter, C. D. (1977). Solar limb darkening. I-At wavelengths of 3033-7297. *Solar Physics*, 51:25–41.

Platt, U. and Stutz, J. (2008). *Differential absorption spectroscopy*. Springer.

Rodgers, C. D. (2000). *Inverse methods for atmospheric sounding: theory and practice*, volume 2. World scientific.

Seidelmann, P. K. (1992). *Explanatory Supplement to the Astronomical Almanac*. University Science Books, California, U. S. Naval Observatory, Washington, D.C.

Shindell, D. T., Faluvegi, G., Koch, D. M., Schmidt, G. A., Unger, N., and Bauer, S. E. (2009). Improved attribution of climate forcing to emissions. *Science*, 326(5953):716–718.

Sillman, S. (2003). Tropospheric ozone and photochemical smog. *Treatise on geochemistry*, 9:612.

Sillman, S., Logan, J. A., and Wofsy, S. C. (1990). The sensitivity of ozone to nitrogen oxides and hydrocarbons in regional ozone episodes. *Journal of Geophysical Research: Atmospheres*, 95(D2):1837–1851.

Sun, Y.-Y., Chen, C.-H., Yu, T., Wang, J., Qiu, L., Qi, Y., and Lin, K. (2022). Temperature response to the June 2020 solar eclipse observed by FORMOSAT-7/COSMIC2 in the Tibet sector. *Terrestrial, Atmospheric and Oceanic Sciences*, 33(1):2.

Sunyer, J., Spix, C., Quénel, P., de León, A. P., Pönka, A., Barumandzadeh, T., Touloumi, G., Bacharova, L., Wojtyniak, B., Vonk, J., Bisanti, L., Schwartz, J., and Katsouyanni, K. (1997). Urban air pollution and emergency admissions for asthma in four European cities: the APHEA Project. *Thorax*, 52(9):760–765.

Trees, V., Wang, P., and Stammes, P. (2021). Restoring the top-of-atmosphere reflectance during solar eclipses: a proof of concept with the UV absorbing aerosol index measured by TROPOMI. *Atmospheric Chemistry and Physics*, 21(11):8593–8614.

Van Geffen, J., Boersma, K. F., Eskes, H., Sneep, M., Ter Linden, M., Zara, M., and Veefkind, J. P. (2020). S5P TROPOMI NO 2 slant column retrieval: Method, stability, uncertainties and comparisons with OMI. *Atmospheric Measurement Techniques*, 13(3):1315–1335.

Van Geffen, J., Eskes, H. J., Boersma, K. F., and Veefkind, J. P. (2021). *TROPOMI ATBD of the total and tropospheric $NO_2$ data products*. KNMI, De Bilt, The Netherlands, Report S5P-KNMI-L2-0005-RP, version 2.2.0 edition. (last access: 7 September 2023).

Vandaele, A. C., Hermans, C., Simon, P. C., Carleer, M., Colin, R., Fally, S., Merienne, M.-F., Jenouvrier, A., and Coquart, B. (1998). Measurements of the $NO_2$ absorption cross-section from 42 000 $cm^{-1}$ to 10 000 $cm^{-1}$ (238-1000 nm) at 220 K and 294 K. *Journal of Quantitative Spectroscopy and Radiative Transfer*, 59(3-5):171–184.

Veefkind, J. P., Aben, I., McMullan, K., Förster, H., de Vries, J., Otter, G., Claas, J., Eskes, H. J., de Haan, J. F., Kleipool, Q., van Weele, M., Hasekamp, O., Hoogeveen, R., Landgraf, J., Snel, R., Tol, P., Ingmann, P., Voors, R., Kruizinga, B., Vink, R., Visser, H., and Levelt, P. F. (2012). TROPOMI on the ESA Sentinel-5 Precursor: A GMES mission for global observations of the atmospheric composition for climate, air quality and ozone layer applications. *Remote Sensing of Environment*, 120:70–83.

Warmiński, K. and Bęś, A. (2009). Diurnal and seasonal variations in the $NO_2$ photolysis rate constant, NO titration rate constant and the $NO_2$/NO ratio in ambient air in the City of Olsztyn. *Ecological Chemistry and Engineering.*, 16(8):1029–1037.

Wood, R. W. (1922). XLIX. Atomic hydrogen and the balmer series spectrum. *The London, Edinburgh, and Dublin Philosophical Magazine and Journal of Science*, 44(261):538–546.

World Health Organization (2003). *Health aspects of air pollution with particulate matter, ozone and nitrogen dioxide: report on a WHO working group, Bonn, Germany 13-15 January 2003*. Copenhagen: WHO Regional Office for Europe.

Wu, J.-B., Wang, Z. F., Zhang, W., Dong, H. B., Pan, X. L., Li, J., Lin, C.-Y., and Xie, P. H. (2011). The effects of a solar eclipse on photo-oxidants in different areas of China. *Atmospheric Chemistry and Physics*, 11(15):8075–8085.

Wypych, G. (2015). *Handbook of UV Degradation and Stabilization*. ChemTec Publishing, 2nd edition.

Zoogman, P., Liu, X., Suleiman, R. M., Pennington, W. F., Flittner, D. E., Al-Saadi, J. A., Hilton, B. B., Nicks, D. K., Newchurch, M. J., Carr, J. L., Janz, S. J., Andraschko, M. R., Arola, A., Baker, B. D., Canova, B. P., Chan Miller, C., Cohen, R. C., Davis, J. E., Dussault, M. E., Edwards, D. P., Fishman, J., Ghulam, A., González Abad, G., Grutter, M., Herman, J. R., Houck, J., Jacob, D. J., Joiner, J., Kerridge, B. J., Kim, J., Krotkov, N. A., Lamsal, L., Li, C., Lindfors, A., Martin, R. V., McElroy, C. T., McLinden, C., Natraj, V., Neil, D. O., Nowlan, C. R., O'Sullivan, E. J., Palmer, P. I., Pierce, R. B., Pippin, M. R., Saiz-Lopez, A., Spurr, R. J. D., Szykman, J. J., Torres, O., Veefkind, J. P., Veihelmann, B., Wang, H., Wang, J., and Chance, K. (2017). Tropospheric emissions: Monitoring of pollution (TEMPO). *Journal of Quantitative Spectroscopy and Radiative Transfer*, 186:17–39.

# A

# Appendix A: Conversions of $NO_2$ and NO profiles

$\rho$, air density [kg $m^{-3}$]
$P$, absolute pressure [Pa]
$R_{air}$, specific gas constant of dry air = 287.05 [J $kg^{-1}$ $K^{-1}$]
$T$, absolute temperature [K]

$$\rho = \frac{P}{R_{air} * T} \tag{A.1}$$

$[NO_2]_{no\ eclipse}$, number density of $NO_2$ per atmospheric layer [$cm^{-3}$], before eclipse implementation
$NO_{2,VMR}$, volume mixing ratio of $NO_2$ per atmospheric layer [mol $mol^{-1}$]
$N_a$, Number of Avogrado = $6.02214076 * 10^{23}$ [-]
$M_{air}$, molar mass of dry air = 0.0289652 [kg $mol^{-1}$]

$$[NO_2]_{no\ eclipse} = NO_{2,VMR} * \frac{N_a * \rho}{M_{air}} * 10^{-6} \tag{A.2}$$

Eclipse implementation is applied. $[NO_2]_{no\ eclipse}$ is converted to $[NO_2]_{eclipse}$ (see Equation 4.14).

$[NO_2]_{eclipse}$, number density of $NO_2$ per atmospheric layer [$cm^{-3}$], after eclipse implementation

$$NO_{2,VMR} = \frac{[NO_2]_{eclipse} * M_{air}}{N_a * \rho} * \frac{1}{10^{-6}} \tag{A.3}$$

$NO_{2,partial}$, mols per $m^2$ of $NO_2$ per atmospheric layer [mol $m^{-2}$]
$P_{diff}$, pressure difference per atmospheric layer [Pa]
$g$, gravitational constant Earth = 9.80665 [kg $s^{-2}$]

$$NO_{2,partial} = \frac{NO_{2,VMR} * P_{diff}}{g * R_{air}} \tag{A.4}$$

$NO_{2,total}$, $\mu$mol of $NO_2$ for total column [$\mu$mol $m^{-2}$]

$$NO_{2,total} = \sum NO_{2,partial} * 10^6 \tag{A.5}$$

# B

# Appendix B: Effect of the DOAS algorithm on the modelled reflectance during a solar eclipse

## B.1. Influence of Balmer lines on modelled reflectance

With the analysis of the residuals of the DOAS fit process, as has been covered in Subsection 4.2.3, the goodness of the fit has been analysed using the wavelength spectra of cloud-free pixels. The increasing residual values positively correlated to the observed obscuration fraction. In this part, we focus on the countereffect of the rising, positively orientated, residuals which are the negatively orientated residual peaks following the peaks at the wavelengths of the Balmer lines. For higher obscuration fractions they become more distinct, as shown in the following figure:

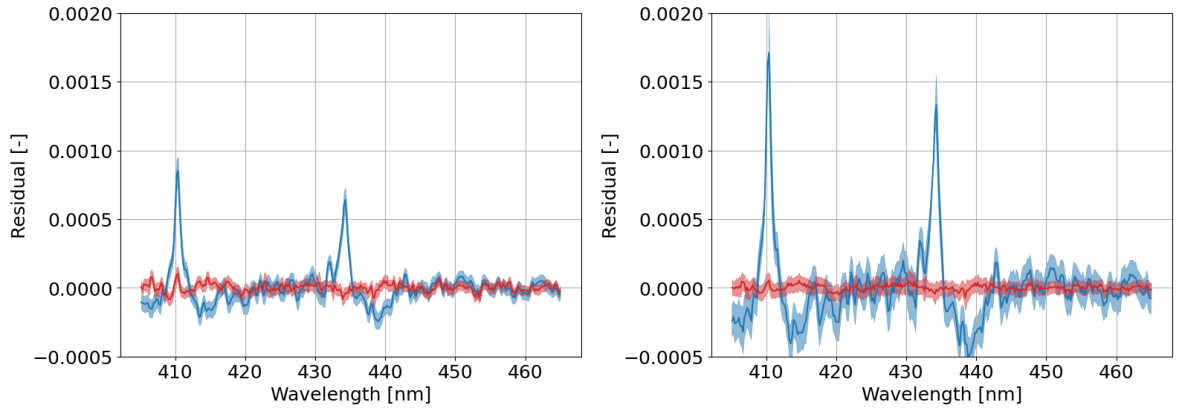


**(a)** For cloud-free pixels with $0.6 < f_o < 0.65$.

**(b)** For cloud-free pixels with $0.7 < f_o < 0.75$

**Figure B.1:** Eclipse wavelength spectrum (in blue) and reference wavelength spectrum (in red) for pixels with specified obscuration fractions.

For both Figure B.1a and Figure B.1b it can be seen that around the Balmer lines at the specified wavelengths of 410 nm and 434 nm, the residual shows large increases. Accompanied by these large positive increases are smaller negatively orientated decreases, which still differ significantly from the reference wavelength spectrum. Interestingly, the significant negative residuals do not present themselves around wavelengths that are known to influence the spectrum in this particular way. The shape of the spectrum suggests that the decreases may be a response to the large increases that preceded them. Since the DOAS fitting process uses polynomials to model the measured reflectance, this can be a possible explanation considering the wave movement of a polynomial. This can be best anal-

ysed by plotting the measured and modelled reflectances, to be able to distinguish the origin of this phenomenon.

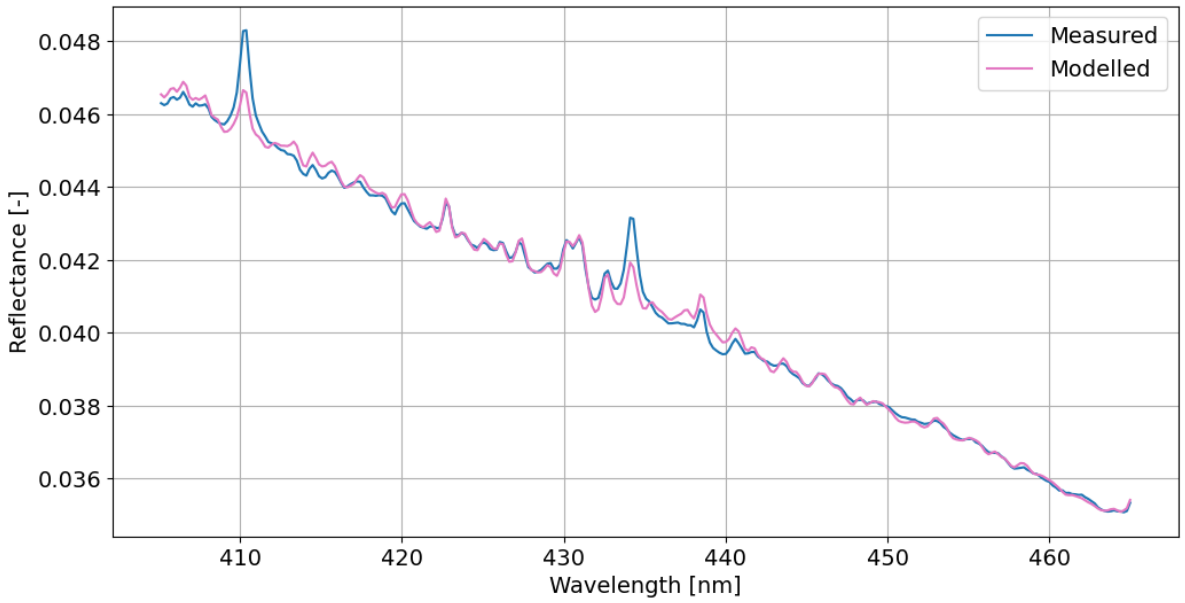


**Figure B.2:** Measured and modelled reflectance of cloud-free pixels with $0.7 < f_o < 0.75$.

Comparison of the measured and modelled reflectance supports the hypotheses made concerning the negative residuals as shown in Figure B.1. The results in Figure B.2 show that the measured reflectance only shows the large positive increases and no clear negative deviations from the overall trend are visible. The results in Figure B.2 show that the modelled reflectance is the cause of the negative residuals as it shows an overestimation in the modelled reflectance following the modelled peak at the Balmer lines. This relates to the wave moment of a polynomial of the modelled reflectance as the relatively large increase in reflectance around the Balmer lines slowly dampens out. In summary, the negative residual response as shown in Figure B.1 can be related to the DOAS fitting process and are not related to the reflectance response of the solar eclipse. Moreover, these results provide important and interesting insight into the coupling of the fitting process and the external influence of the solar eclipse.

# C

# Appendix C: Analysis of the root-mean-square error

Here, the analysis of the root-mean-square (RMS) error is shown. One solar eclipse case, on 25 October 2022, and a non-eclipse test case, on 9 October 2022, are considered. Evidently, the analysis shows an improvement of the RMS error.

## C.1. Solar eclipse case: 25 October 2022

As presented in Subsection 5.1.2, the solar eclipse induces an obscuration of the sunlight which presents the shadow of the eclipse in the east of this specific orbit. In Figure C.1, the uncorrected radiance file in combination with the spike removal turned off was used in the DOAS retrieval algorithm for $NO_2$. This was done to obtain a representation of the physics at hand during a solar eclipse, without any filtering or correcting done related to bad quality.

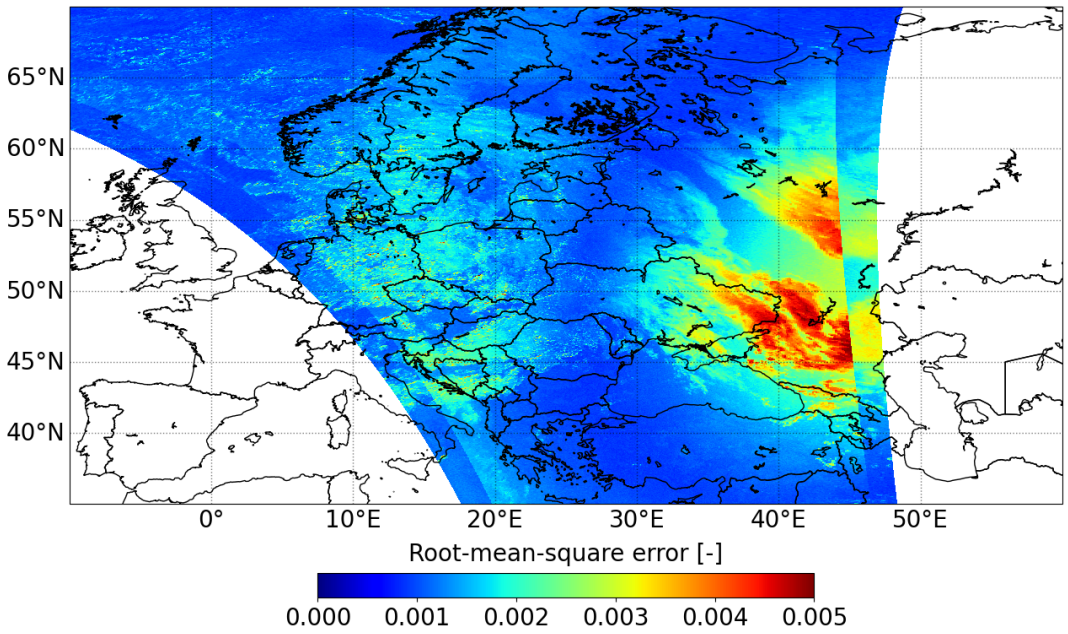


**Figure C.1:** Root-mean-square error as originally retrieved by the DOAS algorithm using the original (uncorrected) radiance as input, on 25 October 2022 during TROPOMI orbit 26077. The spike removal was turned off for this retrieval.

Figure C.1 shows an area of elevated RMS error values in the shadow of the eclipse. This is inline with the presented slant column density and retrieved errors within the TROPOMI algorithm as discussed

in Section 3.2. Figure C.2 shows the root-mean-square error values after the performed radiance correction (see Subsection 4.2.1).

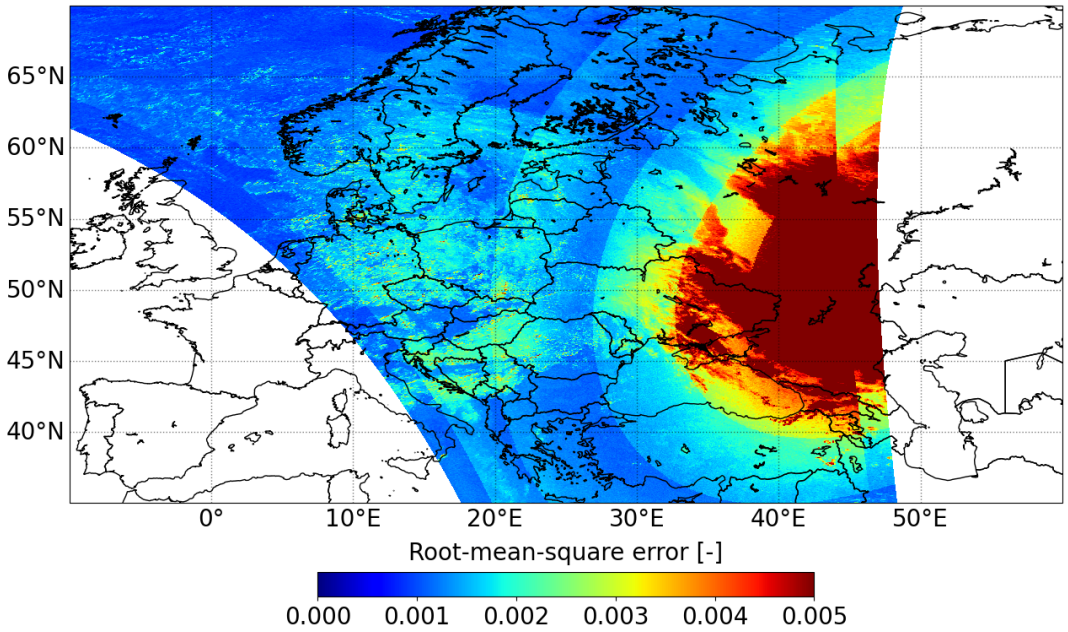


**Figure C.2:** Root-mean-square error as retrieved by the original $NO_2$ retrieval after the appliance of the radiance correction, on 25 October 2022 during TROPOMI orbit 26077. The spike removal was turned off for this retrieval. Note that the circular bands visible are not related to solar eclipse effects, but are caused by a bug in the code.

From Figure C.2, a clear increase of the RMS error can be concluded as the magnitude of the radiance is corrected for the influence of the solar eclipse to acquire respectable reflectance values. Again, here the spike removal was turned off and still the original $NO_2$ retrieval is used. The radiance correction induced significantly higher RMS errors due to the fact that the DOAS algorithm has difficulties to compute a modelled reflectance that matches the measured reflectance. The importance of correcting for the radiance is here shown, as it supports the unreliability of the algorithm during a solar eclipse.

It must be noted that the circular bands visible in Figure C.2 are not related to any solar eclipse-induced effects. These are related to a bug in the code, which occurs during the radiance correction. It is caused by the noise correction, based on the obscuration fraction, as described in Subsection 4.2.1 through Equation 4.5, Equation 4.6 and Equation 4.7. Here, conversions back and forth from dB are needed, including rounding to an integer. The rounding to an integer is the reason for the sharp transitions seen in the RMS error values. The circular bands are related to the influence of the obscuration fraction during the solar eclipse.

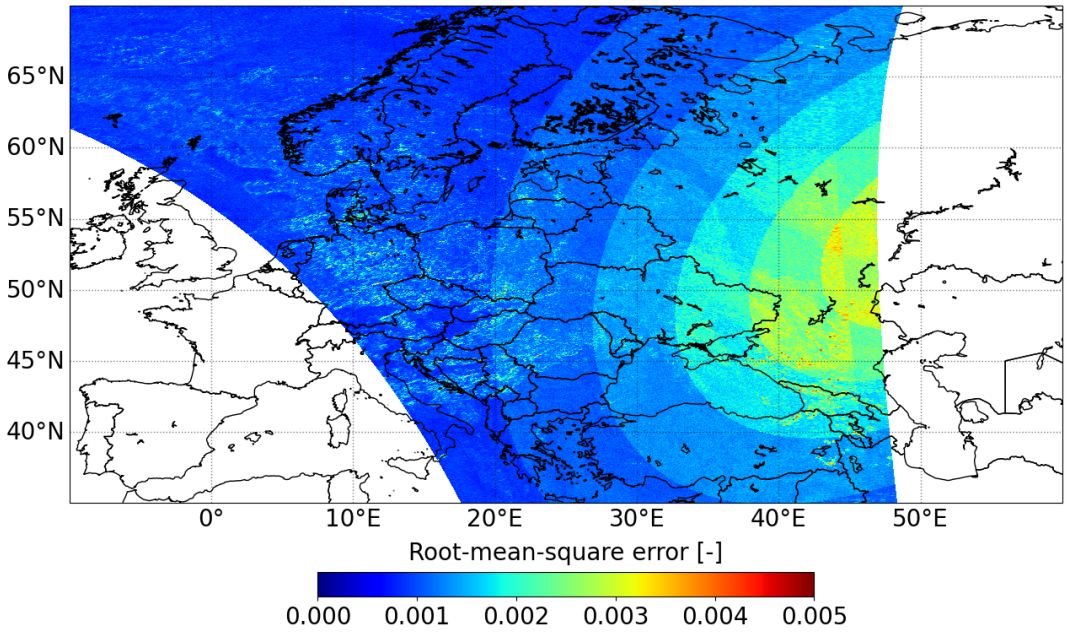


**Figure C.3:** Root-mean-square error as retrieved by the adjusted $NO_2$ retrieval, on 25 October 2022 during TROPOMI orbit 26077. The spike removal was turned off for this retrieval. Note that the circular bands visible are not related to solar eclipse effects, but are caused by a bug in the code.

Despite the disturbance of the circular bands, a clear improvement of the root-mean-square error is seen in Figure C.3 from the adjusted retrieval in comparison to the RMS values from the original retrieval as shown in both Figure C.1 and Figure C.2. This supports the conclusion earlier made, that the adjustment of the $NO_2$ improves the reliability of the measurements taken during a solar eclipse by TROPOMI.

## C.2. Test case: 9 October 2022

As validation for the use of the new wavelength window in the $NO_2$ retrieval, the comparison is made between the root-mean-square error values of both the original window and the adjusted window for a non-eclipse orbit.

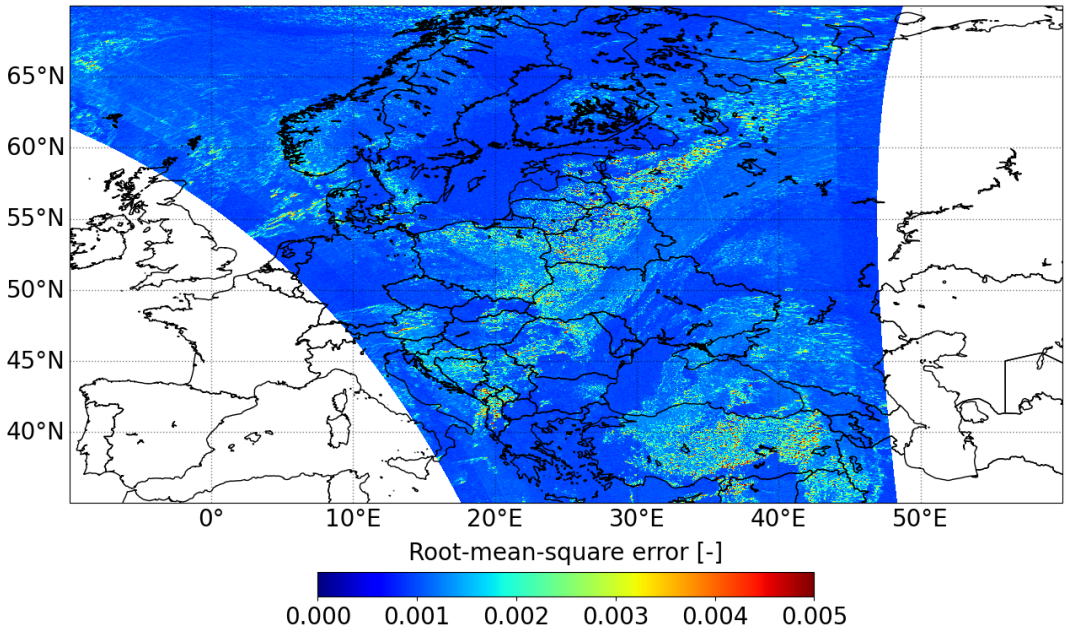


**Figure C.4:** Root-mean-square error as retrieved by the original $NO_2$ retrieval, on 9 October 2022 during TROPOMI orbit 25850.

The circular bands as previously seen in the figures presented in Section C.1 are not seen in the analysis of the test case inFigure C.5, as no radiance correction was needed here to correct for any solar eclipse effects.

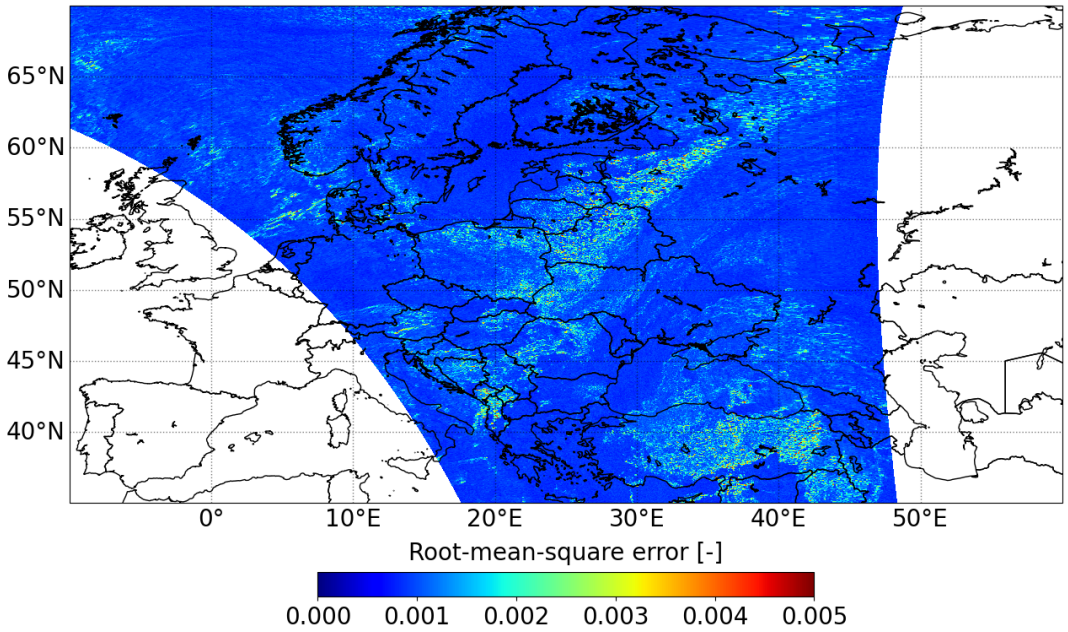


**Figure C.5:** Root-mean-square error as retrieved by the adjusted $NO_2$ retrieval, on 9 October 2022 during TROPOMI orbit 25850.

No significant changes in RMS error values are seen between the change in wavelength window from Figure C.4 and Figure C.5. This supports the conclusion drawn in the earlier validation using the test case in Section 4.3, that the adjusted $NO_2$ retrieval can be trusted.